

HTOSR-TR. C16-  
0048

## FINAL REPORT

Approved for public release,  
distribution unlimited

# DETERMINATION OF STRUCTURE TEMPERATURE AND CONCENTRATION IN THE NEAR INJECTOR REGION OF IMPINGING JETS USING HOLOGRAPHIC TECHNIQUES

AFOSR Grant No. F49620-92-J-0343

Principal Investigator  
Prof. Dimos Poulikakos

Department of Mechanical Engineering  
University of Illinois at Chicago  
842 W. Taylor St.  
Chicago, IL 60607-7022

19960220 022

DTIC QUALITY INSPECTED 1

Form Approved  
OMB No. 0704-0188

1. AGENCY USE ONLY (Leave blank)	2. REPORT DATE January 25, 1996	3. REPORT TYPE AND DATES COVERED FINAL 6/1/92 - 5/31/95
----------------------------------	------------------------------------	--

**G-F49620-92-J-0343**

PI: Dimos Poulikakos

8. PERFORMING ORGANIZATION  
REPORT NUMBER

: 10. SPONSORING / MONITORING  
: AGENCY REPORT NUMBER

## 11. SUPPLEMENTARY NOTES

Approved for public release; distribution is unlimited.

12b. DISTRIBUTION CODE

The purpose of this research was to investigate the dense region of a spray generated by two high speed impinging jets, using a novel holographic technique developed and tested under the present grant. The dense spray region was shown to contain a large population of non-spherical liquid elements. This region cannot be studied with more conventional optical methods. The structure of the liquid elements near the jet impact point was indicative of the mechanisms of the disintegration process. The overall spray pattern clearly revealed the wave nature of the breakup process, which was more distinct with high viscosity liquids. Smaller and faster droplets were generated with larger impingement angle, higher jet velocity, and smaller orifice diameter. Surface tension plays an important role in the droplet size without any noticeable effect on the spray pattern, whereas viscosity affects the structure without any significant effect on the droplet size. In the parametric domain investigated, the average droplet velocities were linearly proportional to the liquid jet velocity despite the large variation in the liquid properties. The droplet velocities were not affected markedly by the liquid properties. The theoretical predictions for the mean droplet size provided a reasonable order-of-magnitude estimate. The superiority of the universal root-normal distribution to the Rosin-Rammler distribution was proved in the great majority of high jet velocity cases tested. The presence of a high temperature environment significantly altered the spray pattern. An important finding was that while evaporation effects reduce the size of large liquid elements and droplets, they are also responsible for the complete disappearance of small droplets. This partially offsets the impact of a high temperature environment on the average droplet size in the spray.

Holography, Impinging high-speed jets, structure, break-up, velocity, atomization, dense region

64

16. PRICE CODE

unclassified

unclassified

unclassified

UL

## CONTENTS

<b>Summary</b>	<b>Page</b>
	2
<b>Nomenclature</b>	3
<b>1. Introduction and Background</b>	5
<b>2. Experiments</b>	12
2.1 <i>Impinging Jet Apparatus</i>	12
2.2 <i>Optical System for Holographic Recording</i>	13
2.3 <i>Hologram Reconstruction and Image Processing</i>	14
<b>3. Results and Discussion</b>	16
3.1 <i>Low and Moderate Jet Velocities</i>	16
3.2 <i>High Jet Velocities</i>	19
3.2a Test Conditions and Physical Properties of Liquids	19
3.2b Overall Spray Pattern	20
3.2c Droplet Size Measurements	23
3.2d Theoretical Prediction for Droplet Sizes	25
3.2e Droplet Size Distribution	27
3.2f Droplet Velocity Measurements	28
3.3 <i>Experiments in an Elevated Temperature Environment</i>	30
<b>References</b>	32
<b>Tables</b>	35
<b>Figures</b>	37
<b>List of Professional Personnel and Publications</b>	64
<b>Appendix A</b>	
<b>Appendix B</b>	

# **DETERMINATION OF STRUCTURE, TEMPERATURE AND CONCENTRATION IN THE NEAR INJECTOR REGION OF IMPINGING JETS USING HOLOGRAPHIC TECHNIQUES**

AFOSR Grant No. F49620-92-J-0343

Principal Investigator : Prof. Dimos Poulikakos

Department of Mechanical Engineering  
University of Illinois at Chicago  
842 W. Taylor St.  
Chicago, IL 60607-7022

## **SUMMARY**

The purpose of this research was to investigate the dense region of a spray generated by two high speed impinging jets, using a novel holographic technique developed and tested under the present grant. The dense spray region was shown to contain a large population of non-spherical liquid elements. This region cannot be studied with more conventional optical methods. The structure of the liquid elements near the jet impact point was indicative of the mechanisms of the disintegration process. The effect of several parameters such as the impingement angle, the liquid jet velocity, the orifice diameter, and the liquid properties on the atomization process was investigated. In addition, experiments in a high temperature chamber were performed. The overall spray pattern clearly revealed the wave nature of the breakup process, which was more distinct with high viscosity liquids. Smaller and faster droplets were generated with larger impingement angle, higher jet velocity, and smaller orifice diameter. Surface tension plays an important role in the droplet size without any noticeable effect on the spray pattern, whereas viscosity affects the structure without any significant effect on the droplet size. In the parametric domain investigated, the average droplet velocities were linearly proportional to the liquid jet velocity despite the large variation in the liquid properties. The droplet velocities were not affected markedly by the liquid properties. The theoretical predictions for the mean droplet size provided a reasonable order-of-magnitude estimate. The superiority of the universal root-normal distribution to the Rosin-Rammler distribution was proved in the great majority of high jet velocity cases tested. For low jet impingement velocities, existing theoretical predictions on the size and shape of the liquid sheet as well as on the size distribution of the droplets around the sheet boundary were also tested against the experimental measurements. For most part, the predicted shape agreed rather well with the experimental observations qualitatively as well as quantitatively. As the impingement velocity increased, the agreement on the maximum sheet thickness deteriorated. The experiments clearly indicated that the non-spherical liquid elements exhibit large size variations in the neighborhood of the same location. This behavior is not predicted by the theories which are based on the premise that the droplets at each angular position are monodispersed. The presence of a high temperature environment significantly altered the spray pattern. An important finding was that while evaporation effects reduce the size of large liquid elements and droplets, they are also responsible for the complete disappearance of small droplets. This partially offsets the impact of a high temperature environment on the average droplet size in the spray.

## NOMENCLATURE

$C$	constant
$D$	diameter
$d_D$	droplet diameter
$d_L$	ligament diameter
$D_j$	orifice diameter
$D_{MMD}$	mass median diameter
$D_{10}$	length-mean diameter
$D_{30}$	volume-mean diameter
$D_{32}$	Sauter-mean diameter
$e$	ratio of longest significant wavelength to liquid jet diameter
$h$	liquid sheet thickness
$h_e$	liquid sheet edge thickness
$h_i$	initial thickness of liquid sheet
$K$	parameter
$q$	Rosin-Rammler drop size distribution parameter
$Q$	liquid volume fraction containing drops of diameter smaller than $d_D$
$r$	radial distance from the impinging point
$r_e$	radial distance of liquid sheet edge
$R$	liquid jet radius
$Re_j$	Reynolds number of liquid jet
$s$	direction of motion of a plane liquid sheet
$U$	velocity of liquid sheet
$V$	velocity
$V_a$	velocity of air
$V_j$	velocity of liquid jet
$V_m$	magnitude of velocity vector of droplet

$V_x$	horizontal velocity component of droplet
$V_y$	vertical velocity component of droplet
$We_j$	Weber number of liquid jet
$x$	horizontal coordinate from impinging point
$X$	characteristic diameter in Rosin-Rammler distribution
$y$	vertical coordinate from impinging point

### Greek Symbols

$\beta$	constant
$\theta$	half of the impingement angle
$\lambda_{\min}$	minimum wavelength for wave growth
$\mu$	viscosity of liquid
$\rho$	density of air
$\rho_l$	density of liquid
$\sigma$	surface tension of liquid
$\phi$	azimuthal angle measured counterclockwise from the y axis
$\psi$	angle between the tangent to the rim of the cardioid sheet and the radius vector

## 1. INTRODUCTION AND BACKGROUND

Impinging-jet injectors are commonly used in liquid propellant rocket engines [1,2]. The liquid propellants (fuel and oxidizer) are injected through a number of separate small holes in such a manner that they impinge upon each other. Combustion instabilities in rocket engines are characterized by sustained pressure oscillations. The origin of the instabilities appears to be related to the atomization and mixing processes of the propellants. Photographs of the spray formed by two impinging jets show the periodic nature of the atomization process [3, 4]. Groups of droplets resulting from the break-up of liquid ligaments give the impression of waves originating from the impingement point. The mechanisms that initiate and sustain these phenomena have not been disclosed satisfactorily.

As shown schematically in Fig. 1, two impinging jets at low liquid jet velocities (Fig. 1a) produce an expanding sheet in a plane perpendicular to the plane containing the two liquid jets. As the jet velocity becomes high enough for the complete atomization of the liquid (Fig. 1b), a small fan-shaped liquid sheet is formed around the impingement point. This liquid sheet disintegrates into unstable arc-shaped liquid ligaments that contract themselves by surface tension and finally break into droplets. The spray characteristics depend on the liquid jet velocity  $V_j$ , the orifice diameter  $D_j$ , the impingement angle  $2\theta$ , the conditions of the surroundings, and the physical properties of the liquid. Although the present study focused on high jet velocities relevant to those encountered in rocket engines, work was also performed at low jet velocities to investigate certain fundamental aspects of the break up process and to test existing theories on droplet sizes.

With reference to low speed impingement, several investigations have been conducted over the years with the aim to understand the mechanism of disintegration of a liquid sheet and to predict its thickness that plays a key role in the resulting droplet sizes. The mechanism of disintegration of a semi-infinite plane liquid sheet where the liquid has

finite viscosity and the thickness of the sheet decreases with distance from the orifice was explored by Dombrowski and Johns [5]. They attributed the disintegration process to the rapidly growing surface waves resulting from interaction with the surrounding gaseous medium. Disintegration occurs when the wave amplitude reaches a critical value and ligaments of the sheet are torn off. These ligaments rapidly contract into unstable ligaments under the action of surface tension and droplets are produced by the break up of these unstable ligaments. Dombrowski and Johns [5] proposed the following diameter for such ligaments

$$d_L = 0.9614 \left[ \frac{K^2 \sigma^2}{\rho \rho_L U^4} \right]^{\frac{1}{6}} \left[ 1 + 2.6 \mu \sqrt[3]{\frac{K \rho^4 U^7}{72 \rho_L^2 \sigma^5}} \right]^{\frac{1}{5}} \quad (1)$$

where  $\sigma$  is the liquid surface tension,  $\mu$  is the liquid viscosity,  $\rho$  is the density of the surrounding medium,  $\rho_L$  is the density of the liquid, and  $U$  is the velocity of the liquid sheet moving in the  $z$  direction. The constant  $K$  is defined in the expression for the thickness of the liquid sheet  $h$ ,

$$h = \frac{K}{s} \quad (2)$$

The (assumed uniform) diameter of the droplets disintegrating from above ligaments is [5]

$$d_D = \left( \frac{3\pi}{\sqrt{2}} \right)^{\frac{1}{3}} d_L \left( 1 + \frac{3\mu}{(\rho_L \sigma d_L)^{\frac{1}{2}}} \right)^{\frac{1}{6}} \quad (3)$$

The variation of the thickness of a liquid sheet created by two impinging jets with radial distance,  $r$ , and angular position,  $\phi$  has been proposed by Hasson and Peck [6].

$$\frac{h r}{R^2} = \frac{\sin^3 \theta}{(1 - \cos \phi \cos \theta)^2} \quad (4)$$

Here,  $R$  is the radius of liquid jet. The basic idea of their analysis is that a cross-section through the jet in a plane parallel to the sheet is an ellipse and mass and momentum is conserved between an angular element in an ellipse and a corresponding element in the liquid sheet. Note that the expressions for the liquid sheet thickness (Eqs. 2 and 4) have not been verified experimentally.

Couto and Bastos-Netto [7] combined Dombrowski and John's analysis [5] and Hasson and Peck's expression [6] for the thickness distribution of the liquid sheet to predict the droplet size distribution. The constant  $K$  required in Eqs. (1, 2) is obtained from

$$K = h r = \frac{R^2 \sin^3 \theta}{(1 - \cos \phi \cos \theta)^2} \quad (5)$$

Note that the coordinate  $s$  in Eq. (2) is replaced by  $r$  in Eq.(5) in order to be consistent with the notation of the direction of motion of the liquid in the sheet in Fig. 1.

Clark and Dombrowski [8] obtained an expression for the size of droplets formed from the rim of a fan spray sheet. They used a perturbation analysis based upon total energy conservation for inviscid flow. Their correlation, including a constant obtained from experimental data, reads

$$d_D = 2.41 \times 10^6 \left( \frac{\sigma}{\rho_L} \right)^{\frac{1}{9}} \left( \frac{K^2}{U} \right)^{\frac{2}{9}} \quad (6)$$

This expression for the droplet size is more applicable to the droplets generated by two impinging jets because it considers droplets shedding tangentially from the edge of an oval liquid sheet whereas Dombrowski and Johns [5] considered droplets generated at the leading edge of a semi-infinite liquid sheet.

Ibrahim and Przekwas [9] obtained theoretical expressions for the thickness and the shape of the liquid sheet. They adopted the expression for the initial sheet thickness obtained by Naber and Reitz [10] in their study of engine spray/wall impingement. This expression reads

$$h_i = \left[ \frac{\beta R \sin \theta}{e^\beta - 1} \right] e^{\beta \left(1 - \frac{\phi}{\pi}\right)} \quad (7)$$

where  $\beta$  is determined from mass and momentum conservation. The thickness at any position,  $r$ , is expressed as

$$h = \frac{R / \sin \theta}{r} h_i \quad (8)$$

To predict the shape of the liquid sheet, they used Taylor's expression [11] for the thickness at the edge of the sheet. Taylor showed that the form of cardioid waves which can remain at rest to form the boundary of the liquid sheet is described by

$$h_e = \frac{2 \sigma}{\rho_L U^2 \sin^2 \psi} \quad (9)$$

where  $\psi$  is the angle between the wave front and the radius vector. They developed an expression for  $\psi$  satisfying all boundary conditions

$$\psi = \left( \frac{\pi}{2} \right) e^{\ln \left( \frac{2\theta}{\pi} \right) \left( 1 - \frac{\phi}{\pi} \right)} \quad (10)$$

The shape of the liquid sheet can be predicted by calculating the radial distance  $r_e$  between the edge of the sheet and the point of impact from Eq. (8) utilizing Eqs. (7, 9, 10)

$$r_e = \frac{R}{\sin \theta} \frac{h_i}{h_e} \quad (11)$$

Experimental verification of the theoretical predictions discussed above was scarce. The work presented in this report aimed at this deficiency. The experimental results for the sheet size and shape as well as for the droplet size were used to test many of the aforementioned theoretical predictions. In addition, a natural progression requires understanding of the low speed impingement process before embarking to the study of the more complex high speed impingement process.

With reference to high speed jets, studies on the spray characteristics of impinging-jet injectors started in the 1950s and 1960s aiming at revealing the atomization mechanisms and predicting the size distribution of droplets. Foster and Heidmann [12] investigated the effects of orifice diameter, jet velocity, impingement angle, pre-impingement length, and liquid properties (viscosity, surface tension) on the structure of the spray. They measured the jet velocity, droplet velocity, mass distribution, liquid sheet break-up characteristics, and maximum drop size. The droplet velocity varied from 99% to 72% of the jet velocity for a change in circumferential position from the spray axis to  $\phi = 80^\circ$ . In a subsequent paper, Heidmann and Foster [13] studied the effect of the impingement angle on the drop size distribution and the spray pattern. The most pronounced effect of a decrease in the impingement angle on the spray pattern was the increase in mass concentration along the spray axis.

Dombrowski and Hooper [14] studied the mechanism of the disintegration of liquid sheets formed by two impinging laminar and turbulent jets. They contributed the

mechanism to the formation of unstable waves of aerodynamic or hydrodynamic origin. Huang [15] investigated the breakup mechanism of axisymmetric liquid sheets formed by the impingement of two co-axial water jets. He reported three breakup regimes depending on the Weber number of the liquid jet ( $We_j = \rho_l D_j V_j^2 / \sigma$ , where  $\rho_l$  and  $\sigma$  are the density and surface tension of the liquid). The first breakup regime,  $100 < We_j < 500$ , was characterized by stable liquid sheets, and the increase of the breakup radius with an increase of the jet velocity. In the second breakup regime,  $We_j > 2000$ , large amplitude anti-symmetric waves grow radially. Transition regimes were observed between above two regimes,  $500 < We_j < 2000$ .

Recent research conducted by Anderson et al. [16] focused on the characteristics of the spray created by two turbulent impinging jets. The mean drop diameters decreased with an increase in the jet velocity and impingement angle. The mean drop velocities were almost equal to the jet velocity regardless of the impingement angle and measured position. These measurements were compared with predictions from an analytical model based on linear stability theory. The predicted drop size could show the previously observed trend but failed to produce quantitative agreement. They suggested that the conceptual fluid dynamic processes at the impingement point, which was initially introduced by Dombrowski and Hooper [14], should be investigated to understand the driving mechanism of the spray formation satisfactorily.

Ryan et al. [17] extended Anderson et al.'s work [16] to investigate the effects of the jet conditions (laminar versus turbulent), orifice diameter, impingement angle, and jet velocity on the atomization of impinging liquid jets. The experimental results contrasting the laminar and turbulent jet conditions demonstrated that the jet conditions had a significant effect on the atomization process. In their theoretical work, they modeled the disintegration of sheets formed by two impinging liquid jets using two existing theories; a stationary antisymmetric wave-based theory for the low Weber numbers [18], and a linear stability-based theory for the high Weber numbers [16]. Vassallo et al. [19] investigated the spray

characteristics of two and four impinging-jet injectors using the PDPA. In the two-jet injector studies, they observed the decrease of mean drop size, the increase of mean velocity, and the increase of the number density with an increase of the jet velocity. For the four-jet injector, they found the critical jet velocity below which the mean drop size and velocity increase.

Despite the important role of impinging-jet injectors in rocket engines, the relevant fluid dynamics mechanisms are still not well understood, partially because the structure near the impinging point has not been clearly revealed. Considerable advances in the development of laser instruments (LDV and PDPA) for the spray diagnostic systems make it possible to obtain reliable data for droplet sizes and velocities in the dilute spray region. However, they have inherent limitations for measurements in the dense spray region where liquid elements are rather large and non-spherical. In addition to that, no information of the structure around the impingement point can be obtained by using these instruments.

This report contains the main results of an experimental investigation, based on two-reference beam double-pulse holography, for visualization of the spray structure as well as measurements on the size and velocity of the liquid droplets. The new double-pulse holographic technique uses two reference beams instead of one and relies on the change of the polarization direction of the laser light between pulses for the velocity measurements. The experiments involved two nonevaporating impinging jets injected into still air at atmospheric pressure. The effect of several factors on the spray characteristics was examined using water, ethanol, and three glycerol solutions as test liquids. Theoretical predictions on the mean droplet size were also attempted and tested against the experimental results. The frequently used droplet size distributions were compared with the experimental results to validate their application to experimental data. Experiments in an environment with elevated temperature involving evaporation were also performed.

## 2. EXPERIMENTS

### 2.1 *Impinging Jet Apparatus*

The experimental apparatus for two impinging jets is shown schematically in Fig. 2. High pressure  $N_2$  gas from a  $N_2$  gas cylinder is used for pressurizing a liquid reservoir. The liquid flow from the flowmeter passes through an on-off valve and it is divided into two identical branches for the two individual impinging liquid jets. Precision-bore glass tubes are used as impinging jet injectors. These tubes feature highly accurate inner diameters despite their small size and are practically free from surface roughness problems. The inner diameters of the tubes in this study are 1.016 and 1.534 mm. The length of the tubes is 15.24 cm. A 5.08 cm long, 0.635 cm O.D. copper tube bonded at one end of each glass tube is connected to the liquid supplying plastic tube. The entry to the glass tube was smoothly contoured to maintain laminar flow conditions at the injector exit. The laminar flow condition up to the Reynolds number about 10,000 was indicated by visual observations such as no ruffling of liquid jet boundaries and clear glassy appearance of the jets.

The injector is placed through a hole in a square aluminum block mounted on a rotation stage by four threaded rods. Each injector can slide freely and be fixed by three set-screws to adjust the pre-impingement length defined as the length from the liquid jet exit to the impacting point of the obliquely colliding liquid jets. A very accurate adjustment method is required to assure that the two liquid jets exist on the same plane. Otherwise, the liquid sheet produced by two impinging liquid jets is not perpendicular to the plane containing the liquid jets. Four very finely threaded rods used for mounting the aluminum block to the rotation stage can adjust the liquid jet plane so that a "perfect" liquid sheet (at low speeds) is created normal to the liquid jet plane. The impingement angle can be adjusted accurately by a rotation stage. The falling liquid is collected into a cylindrical liquid tank.

## 2.2 Optical System for Hologram Recording

A novel technique was used for the recording of the holograms used for the velocity measurements. This technique allows for the separate reconstruction of the spray image obtained by different pulses of the light source, an advantage that greatly facilitates the image processing of the holograms, particularly in the dense spray region. Figure 3 (a) shows the schematic layout of the holographic recording system. The light source is a ruby laser which can generate a 694 *nm* wavelength, vertically polarized, 1 *J* output energy, either single or double pulse laser beam. The pulse interval was 50  $\mu$ s (after a trial and error process). The short pulse duration (30 *ns*) assures the freezing of all moving liquid elements or droplets and the clarity of the resulting images. For the alignment of all optical components before firing the ruby laser, a He-Ne alignment laser which is mounted on the ruby laser box is used.

A Pockels Cell is used to change the polarization direction of the first pulse. To drive the Pockels Cell, a high voltage pulse generator is utilized. The input signal to this device comes from a synchronization socket in the ruby laser control box. To change the polarization direction of the first pulse only, the Pockels Cell should be activated just before the first pulse throughout the duration of the first pulse. To this end, the high voltage pulse generator provides an adjustable input/output delay and pulse width, from 0.2 *ms* to 1.2 *ms* and from 40 *ns* to 1.2 *ms*, respectively. The output pulse amplitude ranges from 2.0 *KV* to 7.5 *KV*.

A beamsplitter is used to divide the incoming laser beam into an object beam and a reference beam. The object beam is expanded and collimated by a Galilean-type beam expander. The diameter of the object beam is increased up to 10.0 *cm* to cover entirely the spray region of interest. This plane wave passes through the spray region and finally is intercepted at the 10.16 *cm*  $\times$  12.7 *cm* holographic glass plate.

The reference beam passes through a cube type polarization beamsplitter. This beamsplitter reflects the vertical components of polarization in the incident light while permitting the horizontal components to pass undeviated. Therefore, the reference beam of the first pulse, whose polarization direction is changed horizontally by the Pockels Cell, passes through the beamsplitter without any change of direction. The reference beam of the second pulse is reflected at the diagonal plane in the beamsplitter. In this manner, two reference beams which have different incident angles interfere with the object wave. This produces two separate holograms each corresponding to a laser pulse. Each reference wave is diverged by a plano-concave lens to cover the entire holographic plate. Neutral density filters are used to control the reference-to-object-beam ratio as well as the total irradiance at the holographic plate to improve the quality of the holograms. The entire setup is placed on a vibration-isolation optical table.

To find the magnification factor and locate the droplet position, one more hologram of the grid object was taken just after fabricating a spray hologram without any changes in the optical system. The grid with numbered horizontal and vertical lines at 5.0 mm intervals was drawn by a computer, copied onto a transparent paper and attached to a transparent glass plate.

### ***2.3 Hologram Reconstruction and Image Processing System***

The holograms were reconstructed using a 10 mW He-Ne laser as shown in Fig. 3 (b). The reference wave is expanded up to 20 mm diameter by a beam expander and converted to a spherical diverging wave by a plano-concave lens the same as at recording. The reconstructed virtual image of the spray is magnified by a Questar telescope macro lens system (a long distance microscope). A camera which is attached to the end of this system can record the magnified microscopic images of the liquid droplets. Six different locations were identified and studied for both pulses, i.e., three locations in the horizontal direction with  $\Delta x = \pm 2.5 \text{ cm}$  from the spray axis, at two locations ( $\Delta y = 2.5 \text{ cm}$ ) on the spray

axis. The sampling area at each location was approximately  $(\Delta x, \Delta y) = (1.0 \times 1.5 \text{ cm})$ . At one location, the droplet images and the grid were photographed. The droplet images can be magnified seven times in the final photographic print  $(7.5 \text{ cm} \times 11.0 \text{ cm})$ .

The images of droplets and grids printed on the photographic papers were captured by a CCD camera and inputted into a personal computer for the image analysis. Image Analyst provided by Automatrix Inc. was used as the image processing software. The magnification factor between the length of the image on the monitor and the actual length of the image was calculated by measuring the length of one grid the real distance of which is  $5.0 \text{ mm}$ . The value of the conversion factor in this study ranges from  $24.3$  to  $27.9 \mu\text{m}$  per one pixel of the monitor. The diameters of droplets were obtained by measuring the total area of droplets and calculating the equivalent diameter of a circle corresponding to the total area.

To measure the horizontal and vertical velocities of droplets, the absolute coordinates of the centroid of the droplets from the origin of the grid for both pulses were measured. Next, the difference in the coordinates of the centroid in each direction between two pulses was divided by the pulse separation time. To verify the accuracy of the diameter measurements, the holograms of a  $4.763 \text{ mm}$  precision steel ball and a  $306.6 \mu\text{m}$  steel wire were fabricated. The diameters of the steel ball and the wire were measured in the same way as described for the measurements of the liquid droplet diameters. The relative error in the diameter measurements was within 5%. The approximate error involved in the velocity measurements of droplets was estimated in the following manner. Assuming that a maximum of 4 pixels of error (this value is arbitrary but reasonable for the maximum value based on experience) can be involved in the distance measurements, the corresponding distance of error is  $111.6 \mu\text{m}$  using the maximum conversion ratio ( $27.9 \mu\text{m}/\text{pixel}$ ). The velocity of error for this distance is  $2.2 \text{ m/s}$  with  $50 \mu\text{s}$  pulse separation time. This value is within 20% of measured velocities of droplets for  $V_j = 12.0 \text{ m/s}$ .

The total number of droplets measured for each test condition ranged between 500 and 1000. This is relatively small sample size compared to the recommended value (5500) [20]. However, this is inevitable because the measurements were made from the instantaneous spray images (for 30 ns) rather than collecting a large amount of data over a time period (for example, a couple of seconds as customarily done with other laser instruments). Processing of the data is very tedious because the data analysis procedure for the droplet size and velocity measurements is not currently automated. Future efforts in this direction will hopefully yield an automated system analogous to particle image velocimetry.

### 3. RESULTS AND DISCUSSION

#### 3.1 *Low and Moderate Jet Velocities*

The shapes of the liquid sheet (obtained with strobe photography) at three different impingement angles are compared with the theoretically predicted shapes in Figs. 4 to 6. The dotted shapes (corresponding to the outline of the photographed liquid sheet) match rather well with the theoretical predictions of Ibrahim and Przekwas [9] for all impingement angles examined. The only noticeable difference appears at  $\phi = 180^\circ$ . A "V" shape is observed in the theoretical prediction above the impingement point (denoted with a dark circle) as the impingement angle increases (Figs. 5 and 6). No such of shape was visually observed in the experiments (note that the physical presence of the glass tubes prohibited the photographic recording of the liquid sheet in the neighborhood of  $\phi = 180^\circ$ ). As expected, the maximum width of the liquid sheet increases with increasing the impingement angle. However, the maximum length of the liquid sheet is considerably less sensitive to the value of the impingement angle in the range from  $2\theta = 90^\circ$  to  $2\theta = 120^\circ$ . The streaklines due to the movement of droplets indicate that the droplets are shedding from the edge of the liquid sheet in the tangential direction along the edge instead of moving in the

radial direction. This fact is also verified by the measurement of droplet velocities, which will be described later.

The quantitative comparison of the maximum width and the maximum length of the liquid sheet between experimental measurements and theoretical predictions is shown in Fig. 7. The theoretically predicted values of the maximum width [9] in Fig. 7 (a) at low jet impingement velocities match very well with the measured values. However, the theory overestimates the maximum width of the liquid sheet as the jet velocity is increased up to  $V_j = 2.5$  m/s. The disagreement becomes greater at higher velocities, around  $V_j = 3.0$  m/s, especially for  $2\theta = 90^\circ$ . The experiments agree with the predicted trend that the dependence of the maximum width of the sheet on the jet impingement velocity is stronger for high impingement angles. The predicted maximum length of the liquid sheet agrees reasonably with the measured values even though the theory underestimates at low jet velocities and overestimates at high jet velocities of the experiments (Fig. 7 (b)). The theory predicts practically no difference in the maximum length between  $2\theta = 90^\circ$  and  $2\theta = 120^\circ$ . The experiments support this trend which implies that after a certain impingement angle the shape of the liquid sheet keeps widening while its length remains practically constant.

Figure 8 shows typical photographs of microscopic views of a hologram illustrating the droplet formation process. Figure 8 (a) is a view of a portion of the side of the sheet while Fig.8 (b) is nearly under the bottom (tip) of the sheet ( $\phi = 0^\circ$ ). Two facts are clear: First, there is a great variation in droplet size and second the majority of the droplets features non-spherical shapes in particular in the region underneath the sheet (Fig.8 (b)). Using the Image Analyst software an average roundness factor from all the droplets measured was defined. The value of this factor was 0.81 (a value equal to unity corresponds to a perfect sphere). Further breakup of the non-spherical droplets downstream is unlikely.

The droplet size measurements are compared in Fig. 9 to the theoretical predictions of Dombrowski and Johns [5] (with the expression for  $K$  from Hasson and Peck [6])

Ibrahim and Przekwas [9], as well as Clark and Dombrowski [8]. Note that all the droplets observed were sized and are included in Fig. 9. For all impingement angles (Figs. 9a to 9c), no droplets were observed in the upper region of the liquid sheet ( $\phi > \pm 90^\circ$ ) due to the shedding mechanism of droplets in the tangential direction as explained in the discussion relevant to Figs. 4 to 6. On the other hand, the theories in [5] and [9] predicted the existence of droplets all around the liquid sheet because they relied on the assumption that droplets are disintegrating at all locations around the edge of the liquid sheet moving in the radial direction. Utilizing two different expressions for the thickness of the liquid sheet (Hasson and Peck's [6] and Ibrahim and Przekwas' [9]) did not markedly affect in the predicted droplet size distribution using Dombrowski and Johns' analysis [5]. Clark and Dombrowski's correlation [8] predicted droplet sizes larger than those in [5] and [9]. This is because Clark and Dombrowski's analysis [8] focused on droplets disintegrating from the rim of an oval liquid sheet, which are usually coarser than those disintegrating from the leading edge of a semi-infinite liquid sheet [5].

In general, the predicted size distribution falls within the range of the measured values. However, the theories fail to account for the wide distribution of droplet sizes ranging from  $500 \mu\text{m}$  up to  $3000 \mu\text{m}$ . This discrepancy comes from the assumption of Dombrowski and Johns [5] that only one size of droplets is created from the unstable liquid ligaments. This assumption was adopted by all subsequent studies of the process [6-9]. It is recommended that future modeling efforts describe the disintegration of unstable liquid ligaments in a manner that allows for the generation of multiple size of droplets. Note that, we do not report average droplet diameters. However, the coexistence of small and large droplets at the same angular position is obvious in the holograms. Existing theories do not allow for this fact. We believe that improvement is needed in this respect. The coexistence of small and large droplets around small values of  $\phi$  (tip of the liquid sheet) can be physically explained by the likelihood of the presence and partial disintegration of large liquid ligaments in this region. On the other hand, droplets existing at side regions of the

liquid sheet (away from the tip) are perhaps more likely to be torn off directly from the edge of the sheet so that their diameters are comparable to the sheet thickness .

Cumulative droplet size distributions are compared with the Rosin-Rammler distribution function [20] in Fig. 10. The Rosin-Rammler distribution function is expressed in the form

$$1 - Q = \exp \left( -\frac{d_p}{X} \right)^q \quad (12)$$

where  $Q$  is the fraction of the total volume contained in drops of diameter less than  $d_p$ ,  $q$  is a size distribution parameter, and  $X$  is a characteristic diameter such that 63.2% of the total liquid volume is in drops of smaller diameter. The Rosin-Rammler distribution generally fits well with the measurements for all three cases (Fig. 10). The higher value of  $q$  for  $2\theta = 90^\circ$  and  $2\theta = 120^\circ$  indicates that the range of drop sizes is smaller compared to  $2\theta = 60^\circ$ .

Figures 11a and 11b show the horizontal and vertical velocity components of the droplets for two characteristic impingement angles. The horizontal velocities clearly show that droplet shedding occurs tangentially along the edge and not radially. This fact, combined with the cardioid shape of the sheet (Figs. 4-6) are responsible for the presence of negative horizontal velocities in the right half of the sheet in the vicinity of  $\phi = 0^\circ$  and positive horizontal velocities in the left half of the sheet in the same vicinity. The vertical velocity components of the droplets show good symmetry with respect to  $\phi = 0^\circ$  with the maximum occurring at  $\phi = 0^\circ$ . The droplets in the vicinity of  $\phi = 0^\circ$  move straight downward.

### 3.2 High Jet Velocities

#### 3.2a Test Conditions and Physical Properties of Liquid

The test conditions are summarized in Table 1. The Reynolds and Weber numbers of the liquid jet are based on the orifice diameter, liquid properties, and horizontal component of the liquid jet velocity ( $V_j \sin \theta$ ). The effect of the impingement angle, liquid jet velocity, and orifice diameter was examined in the series H of experiments with water. The condition for experiment H1 ( $D_j = 1.016 \text{ mm}$ ,  $2\theta = 90^\circ$ , and  $V_j = 12.0 \text{ m/s}$ ) is considered as the baseline condition. Three experiments with the baseline condition were performed to verify the repeatability of the experimental results. The effect of liquid properties on the spray characteristics was investigated with ethanol (E series) and three glycerol solutions (G series). The mixing percentage of glycerol solutions is by mass throughout this study.

The physical properties of the liquids used in the experiments at  $20^\circ\text{C}$  and  $1 \text{ atm}$  are shown in Table 2. The values in a parenthesis represent the ratio of the properties of ethanol and glycerol to the properties of water. The viscosity of the test liquid was varied by changing the mixing ratio of glycerin and water. It was increased up to 20 times that of water. Ethanol was selected to examine the effect of surface tension.

### 3.2b Overall Spray Pattern

Photographs of the reconstruction of spray holograms illustrating the overall spray pattern are shown in Fig. 12 (a) to (d). Visual observations indicated that the generated sprays with the liquid jet velocities up to  $12 \text{ m/s}$  were primarily two-dimensional (fan spray). However, they became three-dimensional (cone spray) when the liquid jet velocities exceeded  $15 \text{ m/s}$ . The spray image at the baseline condition (Fig. 12a) reveals clearly the typical disintegration process of the liquid sheet produced by two impinging jets. A fan-shaped liquid sheet is formed just near the impingement point due to the obliquely colliding high speed jets. Circumferentially aligned liquid ligaments, which are thicker at the center of the spray and become thinner as  $\phi$  increases, are directly detaching from the above liquid sheet. These ligaments progressively break up into droplets as they move downstream. Further downstream, only small size droplets

are observed. A group of droplets resulting from the disintegration of arc-shaped small liquid ligaments gives the impression of waves propagating from the origin at the impingement point. This can be more clearly seen in Fig. 12 (d) with the high viscosity glycerol solution.

The effect of the impingement angle on the spray pattern was also observed by fabricating holograms for  $2\theta = 90^\circ$ ,  $60^\circ$ , and  $120^\circ$  with  $D_j = 1.016 \text{ mm}$ ,  $V_j = 12.0 \text{ m/s}$ . Photographs of these holograms are not shown for brevity. The expanding angle of the liquid sheet and arc-shaped liquid ligaments greatly increased with an increase in the impingement angle. At the lowest impingement angle,  $2\theta = 60^\circ$ , the size of droplets was noticeably larger than that for the higher impingement angles. This is due to the fact that the size of liquid ligaments, which break up into droplets, is larger at this condition. Quantitative comparisons of droplet sizes will be discussed in the next section 3.2c.

Figures 12 (a) and (b) for  $V_j = 12.0$  and  $19.1 \text{ m/s}$  with  $D_j = 1.016 \text{ mm}$ ,  $2\theta = 90^\circ$  illustrate the effect of the liquid jet velocity on the spray pattern. The overall spray pattern was not substantially altered. However, smaller droplets are produced with an increase of the liquid jet velocity, as will be shown quantitatively in the next section. A small but noticeable difference is that with an increase of the liquid jet velocity, isolated liquid ligaments do not appear clearly. The shape and size of the liquid sheet are also very irregular and smaller compared to those appearing at low jet velocities.

An increase of the orifice diameter from  $D_j = 1.016 \text{ mm}$  to  $D_j = 1.534 \text{ mm}$  with  $V_j = 12.0 \text{ m/s}$ ,  $2\theta = 90^\circ$  generated an entirely different spray pattern (not shown for brevity). The liquid sheet around the impingement point becomes larger and there exist large liquid ligaments in the far downstream region of the spray. Due to the increase of the thickness of liquid ligaments, the boundary of the liquid ligaments contained liquid protrusions which will disintegrate into droplets.

The effect of liquid properties on the overall spray pattern was studied for  $D_j = 1.016 \text{ mm}$ ,  $2\theta = 90^\circ$ . The viscosity of ethanol does not change much compared to that

of water. However, the surface tension of ethanol is 30% that of water. In general, the surface tension of liquid represents the resisting force for the formation of the new surface area. This implies that liquid with lower surface tension is easier to disintegrate. The spray pattern in Fig. 12 (c) for ethanol can be compared with the one in Fig. 12 (a) for water at the same liquid jet velocity. No pronounced effect of surface tension on the overall spray pattern is observed. This fact is also confirmed by Heidmann et al. [4] using varsol the surface tension of which was reduced to about one half that of water. On the other hand, the effect of surface tension is more evident in the droplet size even though it is difficult to compare droplet sizes without magnifying the photographs. The mean droplet diameters of the ethanol spray even at lower jet velocity ( $V_j = 9.1 \text{ m/s}$ ) were found to be much smaller than those of the water spray. This will be discussed in detail quantitatively in the next section.

An example of the spray pattern for glycerol solution is shown in Fig. 12 (d). The viscosity of glycerol solution is increased to 10.2 times that of water for 59% glycerol without much change in surface tension (Table 2). The viscosity of liquid plays an important role in many aspects of atomization. An increase in viscosity lowers the Reynolds number and also prevents the progress of any natural instabilities. These instabilities in the jets and sheets are the main impetus for the atomization of liquid. Therefore, the combined effect of an increase in viscosity is to delay disintegration and increase the size of droplets in the spray.

In Fig. 12 (d), arc-shaped liquid ligaments are detaching earlier from the liquid sheet near the impingement point and stretch out further downstream region of the spray. This is attributed to the delay of the break-up of ligaments due to the high viscosity of glycerol. The sequence of the break-up of liquid ligaments can be clearly seen in this photograph. The liquid ligaments near the impingement point are larger and continuous without any breakage, whereas they become thinner and break up into small size ligaments or droplets downstream. The equally-spaced liquid ligaments imply the

existence of a wave originating from the impingement point. The spacing between liquid ligaments can be interpreted as one wavelength of that wave.

### 3.2c Droplet Size Measurements

Figure 13 shows typical photographs of droplet images at the first and second pulses, which are used for the measurements of droplet size and velocity. This figure demonstrates the ability of the double-pulse holographic technique to record the size and position of liquid elements at two different times. The region shown is downstream along the spray axis. The movement of droplets can be clearly seen and the identification of the same droplets between the two photographs is not difficult. For example, the droplet identified as No. 1 in Fig. 13 (a) corresponding to the first pulse moved to the location identified as No. 1 in Fig. 13 (b) corresponding to the second pulse. The benefit from the separation of the first and second droplet images is remarkable. In conventional double-pulse holography, the droplet images in Fig. 13 (b) would overlap with the images in Fig. 13 (a). This photograph also demonstrates the size diversity of the liquid elements as well as the fact that these elements are largely non-spherical.

To check the repeatability of the experimental results, preliminary experiments were conducted. Three experiments with the baseline condition ( $D_j = 1.016 \text{ mm}$ ,  $2\theta = 90^\circ$ ,  $V_j = 12.0 \text{ m/s}$ ) were performed for this purpose. The maximum changes in mean droplet diameters with respect to the averaged mean diameters for three runs are within 6% for  $D_{10}$  and 15% for  $D_{32}$ . Here,  $D_{10}$  and  $D_{32}$  are length- and Sauter-mean diameters. Based on above results, it is confirmed that the measurement results for mean droplet diameters are within allowable repeatability.

The effect of the impingement angle, liquid jet velocity, and orifice diameter on the droplet diameter is shown in Fig. 14.  $D_{MMD}$  (mass median diameter) is the drop size for which the masses in drops larger and smaller than this diameter are equal. In an average sense, smaller droplets (desirable from the combustion standpoint) are produced

with larger impingement angles, higher jet velocities, and smaller orifice diameters. As the impingement angle and liquid jet velocity are increased, the horizontal momentum of the liquid jet is increased resulting in the increase of the horizontal impact force between two liquid jets. Therefore, the liquid is more widely dispersed centering around the impingement point. Consequently, the thickness of the liquid sheet and liquid ligaments decreases, resulting in smaller droplets. An increase of the orifice diameter from  $D_j = 1.016 \text{ mm}$  to  $D_j = 1.534 \text{ mm}$  produced a spray characterized by large liquid ligaments in the far downstream region of the spray. Relatively large size droplets are produced by the break-up of these ligaments or by direct detachment of liquid from the boundary of ligaments.

Figure 15 shows the effect of liquid properties on the droplet diameter for  $D_j = 1.016 \text{ mm}$ ,  $2\theta = 90^\circ$ . The mean diameters of water and three glycerol solutions fall almost in a straight line regardless of the fact that these data represent the variation of liquid viscosity up to 20 times the viscosity of water. This finding is interesting because the spray pattern of the glycerol solutions (for example, Fig. 12d) was visibly different from that of water at the same liquid jet velocity. On the other hand, the mean diameters of the ethanol spray always fall in the lower region of the above-mentioned straight line even though there was not big difference in the overall spray patterns of ethanol and water. Based on the above findings, it can be concluded that the surface tension of the liquid plays an important role on the droplet size of the spray without noticeable change in the overall spray pattern, whereas viscosity affects the overall spray pattern without marked effects on the droplet size of the spray.

The present results for the droplet diameters are compared with existing available results in Fig. 16. It is worth noting that the orifice diameter used in the comparison for the present study is  $1.016 \text{ mm}$  and those for Heidmann and Foster [13], Dombrowski and Hooper [14], and Anderson et al. [16] are  $2.26$ ,  $0.5$ , and  $0.64 \text{ mm}$ , respectively. As we observed in Fig. 14 (c), the results with the larger orifice diameter (Fig. 16a) feature

larger droplet sizes and vice versa (Figs. 16b and 16c). A decrease of the droplet diameters with an increase of the impingement angle and liquid jet velocity is observed in all the results of other researchers in Fig. 16, which is in agreement with the trends of the present study.

### *3.2d Theoretical Prediction for Droplet Sizes*

There is no definitive theory predicting the droplet sizes in a spray created by two impinging jets. The best alternative is to adopt the theoretical predictions used for fan-spray nozzles. The first attempt for the theoretical prediction of droplet sizes is based on Dombrowski and Johns' analysis [5] discussed in connection with equations (1-3). Utilizing Weber's theory they proposed a droplet diameter given by eq. (3).

In Weber's theory, a liquid ligament is viewed as a liquid jet injected into quiescent air with low jet velocity. The movement direction of the liquid is parallel to the jet axis in this situation. On the other hand, the ligaments found in the spray created by fan-spray nozzles or two impinging jets move in the outward radial direction. This means that the direction of the liquid motion is practically normal to the axis of the ligament. In addition, the radial velocity of the liquid ligament is of the same order as that of the liquid jet velocity. This can be confirmed by considering the fact that the velocities of droplets are always higher than the liquid jet velocity. Based on above considerations, the present study will propose a different model for the break-up of liquid ligaments while maintaining the assumption that the ligaments are formed according to the Dombrowski and Johns' analysis [5].

The only model available (to the best of our knowledge) reflecting the real situation in the ligaments of impinging jets rather closely is the cross-flow atomization, where the liquid jet is injected normal to a gas stream. This model was published by Adelberg [21,22] who studied the penetration of a liquid jet in a gas stream [21] normal to the jet and obtained an expression for the mean droplet diameters due to the breakup of

a liquid jet [22]. A more tractable form of the droplet diameter expression can be found in Reardon [23]. The mean droplet diameter in the capillary regime, which is found at low air velocities, is given by

$$d_D = C \left\{ \frac{(2eR)^{\frac{1}{2}} - (\lambda_{\min})^{\frac{1}{2}}}{(\lambda_{\min})^{-\frac{1}{2}} - (2eR)^{-\frac{1}{2}}} \right\} \quad (13)$$

Here, the parameter  $e$  is the ratio of the longest significant wavelength to the liquid jet diameter,  $R$  is the liquid jet radius, and  $\lambda_{\min}$  is the minimum wavelength for the wave growth which is defined as

$$\lambda_{\min} = 2\pi (16)^{\frac{1}{3}} \left\{ \frac{\mu (\sigma / \rho_l)^{\frac{1}{2}}}{\rho V_a^2} \right\}^{\frac{2}{3}} \quad (14)$$

We attempted to predict droplet sizes by combining Adelberg's [21,22] analysis with Dombrowski and Johns' [23] analysis. To this end, the ligaments are formed based on Dombrowski and Johns' model and the break-up of ligaments is modeled by Adelberg's analysis. Modifications made to fit the notation of the present problem are the replacement of the liquid jet diameter,  $2R$ , with the diameter of a liquid ligament and the approximation of  $V_a$  with the liquid jet velocity,  $V_j$ . The value of the constant  $e$  is 0.06 as estimated by Adelberg [22]. The constant  $C$  in Eq. (13) is  $C = 4.70$ , which was experimentally obtained for the condition of  $D_j = 1.016$  mm and  $2\theta = 90^\circ$ .

The first and second models for the theoretical prediction of droplet sizes are compared with experimentally obtained values in Fig. 17 for  $D_j = 1.016$  mm and  $2\theta = 90^\circ$ . The first model is based on Dombrowski and Johns' analysis [5] and the second

model is the combination of Dombrowski and Johns' analysis [5] and Adelberg's analysis [21,22] proposed herein. For the water and glycerol spray, Dombrowski and Johns' analysis predicts smaller droplet sizes at high liquid jet velocities and larger droplet sizes at low liquid jet velocities than the experimental results. For the ethanol spray, their predictions are close to the experimental results. The theoretical predictions of the second model for the water spray are not much better than those of Dombrowski and Johns [5] although this model accounts for the fact that the gas velocity is normal to the ligament axis. The reasons are attributed to several unverified (for lack of better alternative) assumptions made in our adoption; the replacement of liquid jet diameter with the diameter of ligaments, the use of low liquid jet velocity for the air velocity which is usually above 100 *m/s*. Despite the disagreement between theoretical predictions and experimental results, these models can be used for the approximate estimation of the mean droplet diameters until more improved and refined modeling emerges, as long as reliable values of the constants are obtained from experiments for the specific operating conditions.

### *3.2e Droplet Size Distribution*

Numerous attempts have been made to obtain suitable mathematical or empirical expressions for the drop size distribution in sprays. In the present study, the Rosin-Rammler distribution (presented earlier in eq. 12) and the universal root-normal distribution proposed by Simmons [24] were employed. The universal root-normal distribution is based on the normal distribution which can be found in standard textbooks on statistics [25]. Simmons [24] proposed that a universal nondimensional correlation can be established for various sprays regardless of nozzle type, fuel viscosity, or technique of data acquisition, when the drop diameter is normalized with respect to the  $D_{MMD}$  of the spray and plotted against the cumulative volume percentage. Hence, the independent variable for the normal distribution is replaced by  $\sqrt{\frac{D}{D_{MMD}}}$ . The mean

value is 1.0 by definition and the standard deviation  $\sigma_n$  was 0.238, determined graphically. Given only the  $D_{MMD}$  of the spray, it is possible to predict the volume distribution for any nozzle and operating conditions.

The universal root-normal and Rosin-Rammler distributions are compared with the experimental results in Figs. 18 and 19. Relevant parameters obtained for the Rosin-Rammler distribution are shown in Table 3. The  $D_{MMD}$ , which was obtained from experiments, is compared to that obtained from the Rosin-Rammler distribution in the same table. In most of cases, the superiority of the universal root-normal distribution to the Rosin-Rammler distribution is obvious.

The effect of jet velocity on the cumulative volume distribution is shown in Fig. 18. The maximum diameter and the slope of the curve changes noticeably when the jet velocity changes from  $V_j = 12.0 \text{ m/s}$  to  $V_j = 15.4 \text{ m/s}$ . No substantial variation is observed once the liquid jet velocity is over  $15.0 \text{ m/s}$ . The slope of the curve becomes steeper as the jet velocity is increased. This implies that the droplet diameters which have the same percentage of total liquid volume become smaller. For example, the  $D_{MMD}$  (50% of total liquid volume is within this diameter) obtained from the experimental data is 523.41, 375.31, and 295.35  $\mu\text{m}$  for  $V_j = 12.0, 15.4$ , and  $19.1 \text{ m/s}$ , respectively.

The cumulative volume distribution for different liquids shown in Fig. 19 indicates that the slope of the curve is a bit steeper than that of water at similar operating conditions. This fact is quantitatively confirmed by considering the  $q$  values (4.46 for water and 4.84, 4.93, and 4.74 for ethanol, 59% glycerol, and 68% glycerol, respectively).

### 3.2f Droplet Velocity Measurements

The effect of the impingement angle, liquid jet velocity, and orifice diameter on the droplet velocities is shown in Fig. 20. The droplet velocity,  $V_m$ , will denote the magnitude of the velocity vector throughout this study. In an average sense, faster

droplets are generated with larger impingement angle, higher jet velocity, and smaller orifice diameter. The droplet velocities are almost linearly proportional to the liquid jet velocity as shown in Fig. 20 (b). The magnitude of the droplet velocities is similar to that of the liquid jet velocity, which implies that the velocities of other liquid elements (liquid sheet or liquid ligaments) are also close to the liquid jet velocity. The horizontal velocities do not change much by varying the primary parameters, whereas the vertical velocities show the same trend as the mean droplet velocities.

Figure 21 shows the effect of liquid properties on the droplet velocities for  $D_j = 1.016 \text{ mm}$  and  $2\theta = 90^\circ$ . The linear proportionality of the droplet velocities to the liquid jet velocity (already shown in Fig. 20 b) is still apparent in spite of the large variation in the physical properties of the liquid (surface tension and viscosity). According to this observation, we can conclude that, in the parametric domain studied, the physical properties of the liquid do not markedly affect the droplet velocities of the resulting spray, whereas they have an effect on the droplet diameters, as discussed earlier.

A comparison of mean droplet velocities by local regions is shown in Fig. 22 for the center and side regions of the spray. The mean droplet velocities in Fig. 22 are always greater for the center regions compared to those for the side regions. Foster and Heidmann [12] also observed the same trend, that the droplet velocities at the center are 93 to 99% of the liquid jet velocities, whereas those at the  $80^\circ$  position are 72 to 77% of the liquid jet velocities. The difference is larger for sprays with bigger droplets (Fig. 14a for  $2\theta = 60^\circ$  and Fig. 14c for  $D_j = 1.534 \text{ mm}$ ).

Limited experimental data are available for the comparison of measurements of droplet velocities. Figure 23 shows the comparison of the results of the present velocity measurements with those of Anderson et al. [16]. It is worth noting that the orifice diameter they used is smaller ( $D_j = 0.64 \text{ mm}$ ) than that of the present study ( $D_j = 1.016 \text{ mm}$ ) and the position they probed was  $y = 41 \text{ mm}$  at the spray axis, while the present results were taken from  $y = 50 \sim 70 \text{ mm}$  at the spray axis. The data shown in this figure

are values obtained at one location of the spray and they should not be confused with the representative values obtained by averaging results from several measurement locations. The velocities in [16] are generally smaller than those of the present study. The trends agree rather well.

### 3.3 Experiments in an Elevated Temperature Environment

A preliminary study of impinging jet sprays formed by a pair of 0.8 mm jets impinging at an angle of  $90^\circ$  at ambient temperatures from  $25^\circ\text{C}$  to  $250^\circ\text{C}$  has also been conducted in the course of this work. The fluids utilized were water, a 59% weight percent aqueous glycerol solution, and ethanol. No details of the experimental apparatus are included herein for brevity. Holography was utilized in the manner described earlier in this report. Diameter measurements were obtained for various regions of the spray. Generally, the qualitative nature of the spray pattern remained the same as temperature increased, however, the size of the resulting droplets decreased slightly.

Figures 24a and 24b are plots of the Sauter and length mean diameters versus temperature for ethanol and water, respectively. Both the Sauter and length mean diameters decrease with increasing temperature. For the dense region of the water spray, the rates of decrease are  $0.04\ \mu\text{m}/^\circ\text{C}$  for the length mean diameter and  $0.17\ \mu\text{m}/^\circ\text{C}$  for the Sauter mean diameter. Ethanol features a slightly greater rate of decrease, with values of  $0.1\ \mu\text{m}/^\circ\text{C}$  and  $0.29\ \mu\text{m}/^\circ\text{C}$  in the dense region for the length and Sauter mean diameters, respectively. The temperature effect within the side region is weak. Furthermore, the Sauter mean diameter of the water spray is approximately  $100\ \mu\text{m}$  greater than the ethanol case in both the middle and side regions.

Figures 25a and 25b are plots of the Sauter and length mean diameters respectively for the bottom portion of the spray. As discussed earlier, the viscosity ratio between the spray fluid and the ambient air is decreasing with temperature, therefore, the aerodynamic instabilities will lead to primary atomization of the large droplets and ligaments sooner than

at atmospheric conditions. As the larger structures break into the smaller droplets, the Reynolds number decreases and the aerodynamic instabilities become less of a factor. However, as observed in Figure 25, increased environmental temperature still has an effect on the diameter of the droplets in the bottom portion of the spray where most of the large ligaments have been broken down into smaller droplets. This is a result of partial evaporation of the droplet mass, which leads to slightly decreased droplet diameters with increased temperature. Also, the value of the length mean diameter of the water droplets is approximately 200  $\mu\text{m}$  in both the middle and bottom regions. However, the dense region diameter data do not reflect the presence of the large liquid structures (ligaments) that have not yet disintegrated into droplets. Therefore, even though the diameters of the droplets are approximately the same, one should be cognizant of the fact that the droplets account for a much smaller percentage of the spray mass in the dense region than in the bottom portion.

The change in the diameter of the droplets with respect to temperature is found to not be drastic due to two factors: the large sample regions and the vaporization of the smaller droplets. First, the analysis presented earlier indicates that one of the primary effects of an increased environmental temperature is the magnification of the aerodynamic instabilities that lead to the breakup of large spray structures. Therefore, the droplets breakup earlier, but the resulting size after breakup is not fundamentally different than the atmospheric temperature situation. By averaging the droplet diameters over a large region, the early breakup effect is diluted. Furthermore, once the surface area of the spray structure is increased through primary atomization of the ligaments, the transfer of heat into the spray fluid is enhanced. Evaporation then becomes relevant and it leads to a slightly decreased size of the larger droplets and a disappearance of the smaller droplets. Thus, the small diameter droplets are not present at downstream locations and the mean size is therefore biased towards the larger particles. These two processes together effectively reduce the apparent impact of the temperature on the mean diameter for a large region of the spray.

## REFERENCES

1. Sutton, G. P., *Rocket propulsion element: an introduction to the engineering of rockets*, John Wiley & Sons, 1992.
2. Harrje, D. T., *Liquid Propellant Rocket Combustion Instability*, NASA SP-194, 1972.
3. Heidmann, M. F., and Humphrey, J. C., "Fluctuations in a Spray Formed by Two Impinging Jets," NACA TN 2349, 1951.
4. Heidmann, M. F., Priem, R. J., and Humphrey, J. C., "A Study of Sprays Formed by Two Impinging Jets," NACA TN 3835, 1957.
5. Dombrowski, N. and Johns, W. R., The Aerodynamic Instability and Disintegration of Viscous Liquid Sheets, *Chemical Engineering Science*, vol. 18, pp. 203 - 214, 1963.
6. Hasson, D. and Peck, R. E., Thickness Distribution in a Sheet Formed by Impinging Jets, *A.I.Ch.E. Journal*, vol. 10, pp. 752 - 754, 1964.
7. Couto, H. S., Bastos-Netto, D. and Migueis, C. E., Modeling of the Initial Droplet Size Distribution Function in the Spray Formed by Impinging Jets, *Journal of Propulsion*, vol. 8, pp. 725 - 728, 1992.
8. Clark, J. C. and Dombrowski, N., On the Formation of Drops from the Rims of Fan Spray Sheets, *Aerosol Science*, vol. 3, pp. 173 - 183, 1972.
9. Ibrahim, E. A. and Przekwas, A. J., Impinging Jet Atomization, *Physics of Fluids A*, vol. 3, pp. 2981 - 2987, 1991.
10. Naber, J. D. and Reitz, R. D., Modeling Engine Spray/Wall Impingement, SAE Paper No. 880107, 1988.
11. Taylor, G. I., Formation of Thin Flat Sheets of Water, *Proceedings of the Royal Society of London A*, vol. 259, pp. 1-17, 1960.

12. Foster, H. H., and Heidmann, M. F., "A Spatial Characteristics of Water Spray Formed by Two Impinging Jets at Several Jet Velocities in Quiescent Air," NASA TN D-301, 1960.
13. Heidmann, M. F., and Foster, H. H., "Effect of Impingement Angle on Drop Size Distribution and Spray Pattern of Two Impinging Water Jets," NASA TN D-872, 1961.
14. Dombrowski, N., and Hooper, P. C., "A Study of the Sprays Formed by Impinging Jets in Laminar and Turbulent Flow," *Journal of Fluid Mechanics*, Vol. 18, 1963, p. 392.
15. Huang, J. C. P., "The Break-up of Axisymmetric Liquid Sheets," *Journal of Fluid Mechanics*, Vol. 43, 1970, p. 305.
16. Anderson, W. E., Ryan, H. M., Pal, S., and Santoro, R. J., "Fundamental Studies of Impinging Liquid Jets," AIAA Paper 92-0458, 1992.
17. Ryan, H. M., Anderson, W. E., Pal, S., and Santoro, R. J., "Atomization Characteristics of Impinging Liquid Jets," accepted for publication in *Journal of Propulsion and Power*.
18. Ibrahim, E. A. and Przekwas, A. J., "Impinging Jets Atomization," *Physics of Fluids A*, Vol. 3, 1991, p. 2981.
19. Vassallo, P., and Ashgriz, N., "Effect of Flow Rate on the Spray Characteristics of Impinging Water Jets," *Journal of Propulsion and Power*, Vol. 8, 1992, p. 980.
20. Lefebvre, A. H., *Atomization and Sprays*, Hemisphere Publishing Co., 1989.
21. Adelberg, M., "Breakup Rate and Penetration of a Liquid Jet in a Gas Stream," *AIAA Journal*, Vol. 5, No. 8, 1967, p. 1408.
22. Adelberg, M., "Mean Drop Size Resulting from the Injection of a Liquid Jet into a High-speed Gas Stream," *AIAA Journal*, Vol. 6, No. 6, 1968, p. 1143.

23. Reardon, F. H., "Development and Verification of a Computer Model of Cross-flow Atomization," *Proceedings of 33rd Heat Transfer and Fluid Mechanics Institute*, California State University, 1993, p. 85.
24. Simmons, H. C., "The Correlation of Drop-Size Distributions in Fuel Nozzle Sprays," *Journal of Engineering for Power*, Vol. 99, No. 3, 1977, p. 309.
25. Belz, M. H., *Statistical Methods in the Process Industries*, New York, John Wiley & Sons, 1973.

Table 1 Summary of test conditions

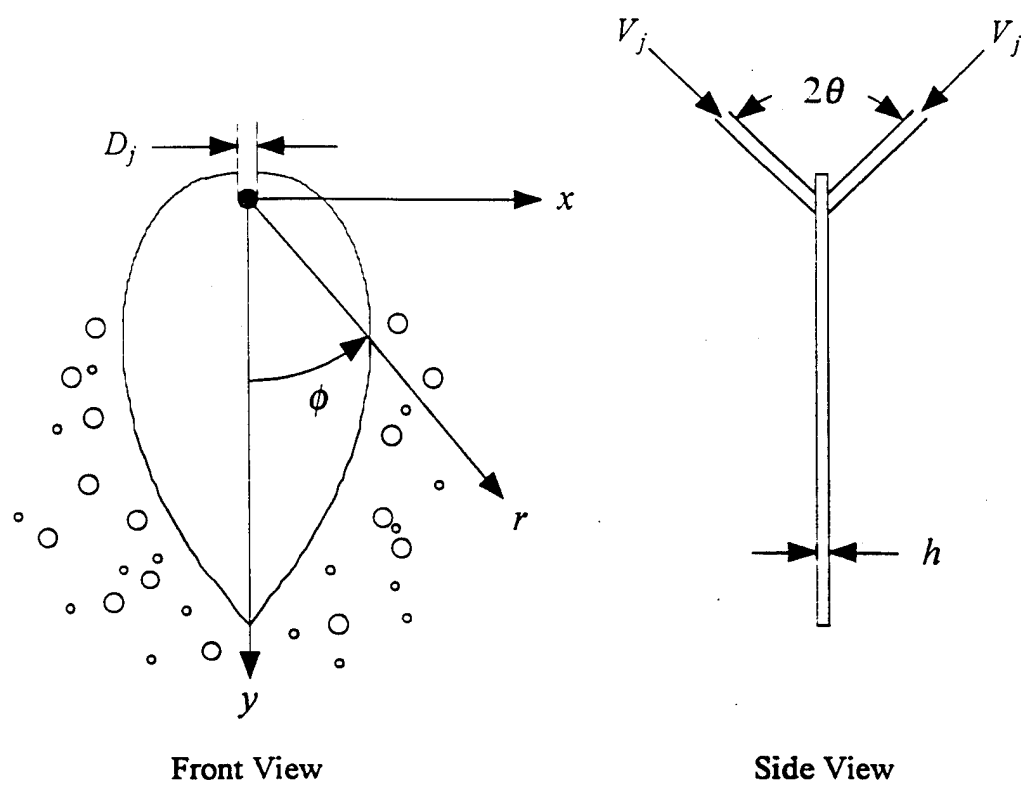
Case	Liquid	Orifice Diameter, $D_j$ (mm)	Impingement Angle, $2\theta$ (°)	Liquid Jet Velocity, $V_j$ (m/s)	$Re_j$	$We_j$
H1-1	water	1.016	90	12.0	8590	1000
H1-2	water	1.016	90	12.0	8590	1000
H1-3	water	1.016	90	12.0	8590	1000
H2	water	1.016	60	12.0	6070	500
H3	water	1.016	120	12.0	10520	1500
H4	water	1.016	90	15.4	11020	1650
H5	water	1.016	90	19.1	13670	2540
H6	water	1.534	90	11.9	12860	1490
E1	ethanol	1.016	90	7.2	3410	920
E2	ethanol	1.016	90	9.1	4300	1460
E3	ethanol	1.016	90	11.9	5640	2520
G1	50% glycerol	1.016	90	8.0	1070	530
G2	59% glycerol	1.016	90	12.3	990	1290
G3	68% glycerol	1.016	90	11.7	510	1210

Table 2 Physical properties of the liquids used in the experiment at 20°C and 1 atm.

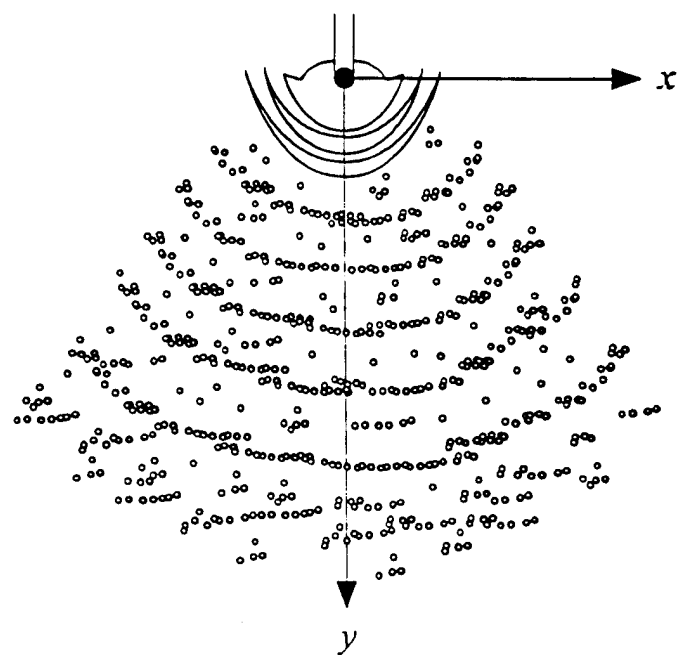
Liquid	Density ( $kg/m^3$ )	Viscosity $\times 10^3$ ( $N\ s/m^2$ )	Surface tension $\times 10^3$ ( $N/m$ )
water	998 (1.0)	1.002 (1.0)	72.88 (1.0)
ethanol	791 (0.79)	1.200 (1.20)	22.80 (0.31)
50% glycerol	1124.9 (1.13)	6.05 (6.04)	69.68 (0.96)
59% glycerol	1149.5 (1.15)	10.25 (10.23)	68.70 (0.94)
68% glycerol	1174.2 (1.18)	19.40 (19.36)	67.72 (0.93)

Table 3  $D_{MMD}$  and parameters obtained for Rosin-Rammler distribution

Case	$D_{MMD} ( \mu m )$		Rosin-Rammler	
	Experiment	Rosin-Rammler	$q$	$X ( \mu m )$
H1	523.41	583.76	4.46	633.76
H2	778.87	768.88	3.99	842.85
H3	424.27	461.81	5.15	495.88
H4	375.31	483.29	4.78	521.81
H5	295.35	363.90	5.27	390.15
H6	696.84	672.92	4.21	734.20
E1	439.68	498.80	4.61	540.10
E2	378.99	445.81	4.84	480.93
G1	540.41	551.09	4.46	598.26
G2	446.46	499.13	4.93	537.66
G3	458.95	510.13	4.74	551.15



(a)



(b)

Figure 1 Liquid sheet formed by impinging jets.

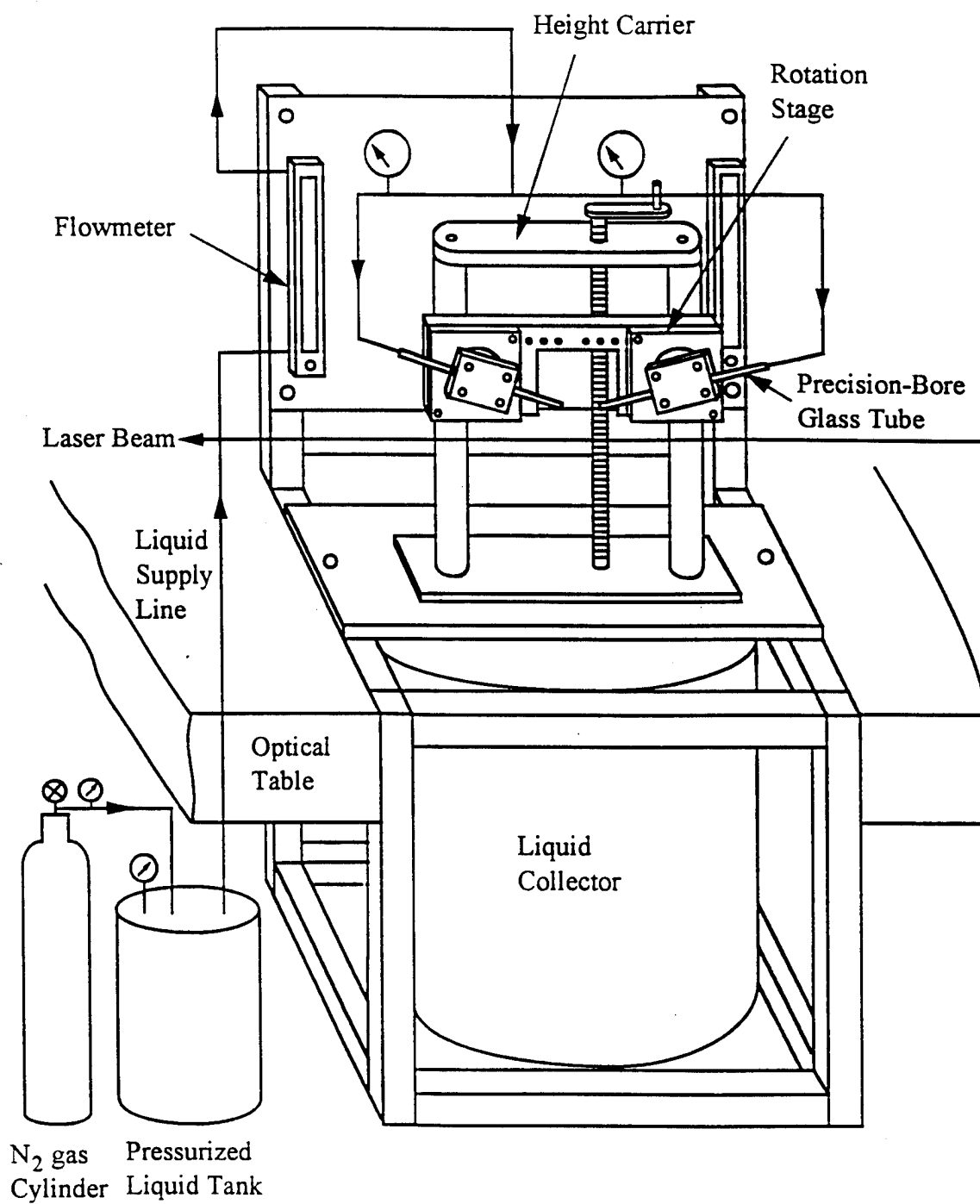
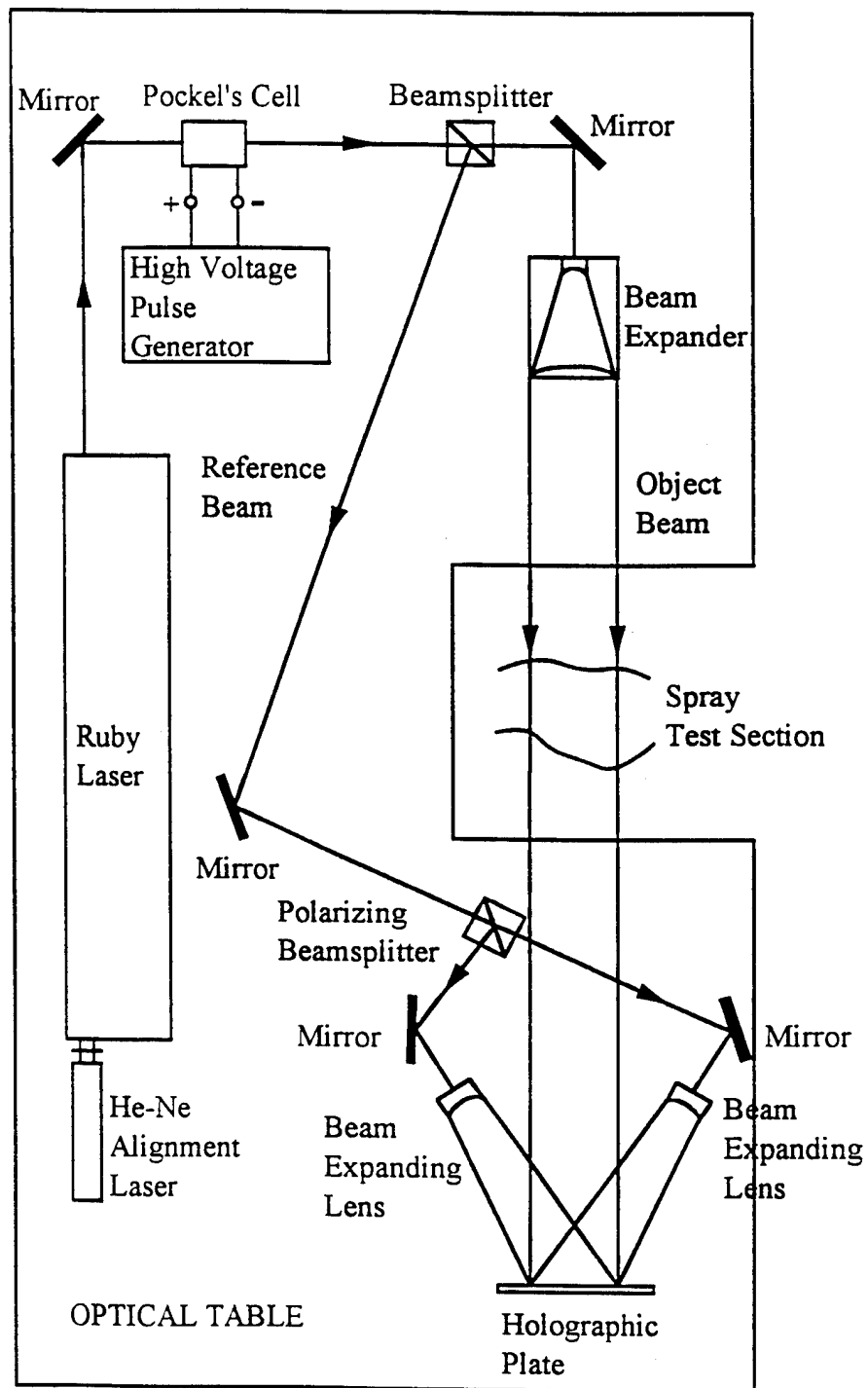


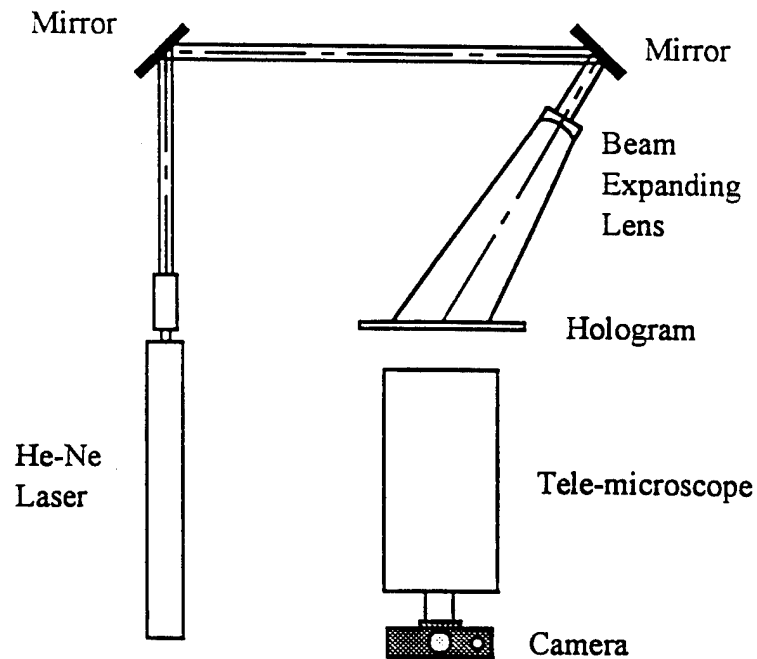
Figure 2 Schematic of the experimental apparatus.



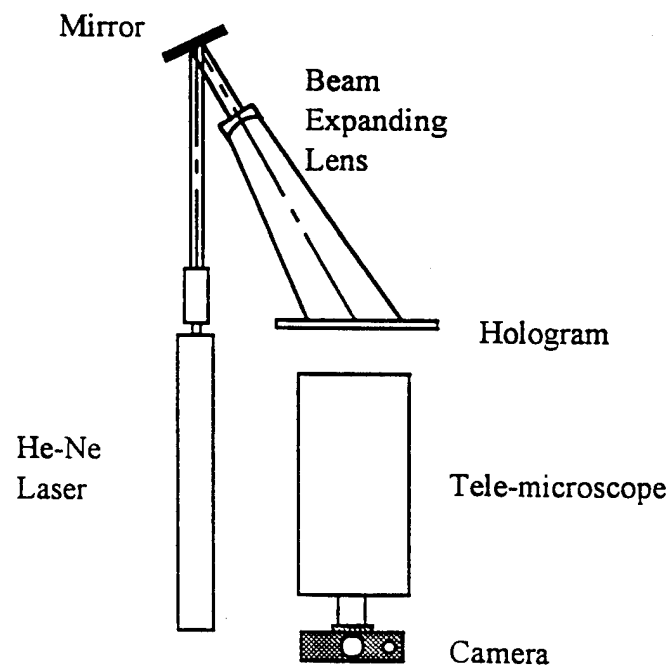
(a)

Figure 3a Schematic of the optical setup for double pulse holograms with two reference beams: recording system.

### First Pulse Image Reconstruction



### Second Pulse Image Reconstruction



(b)

Figure 3b Schematic of the optical setup for double pulse holograms with two reference beams: reconstruction system.

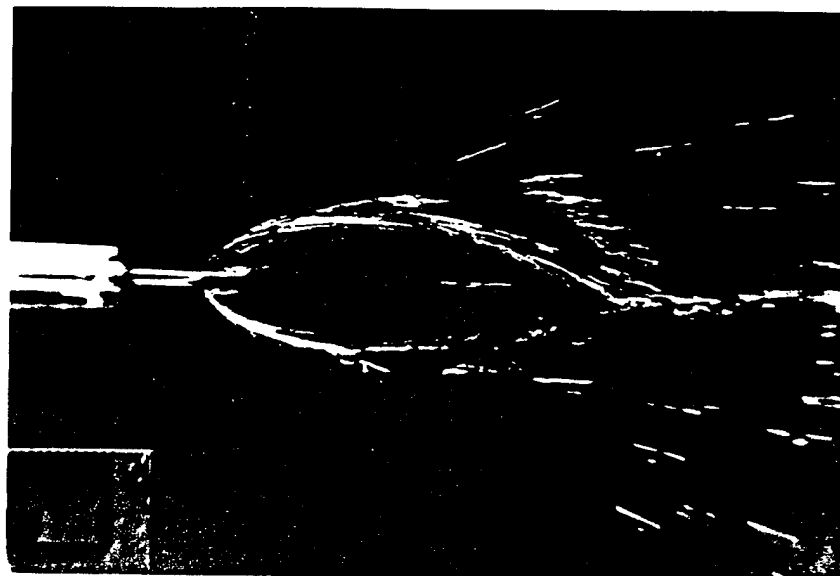
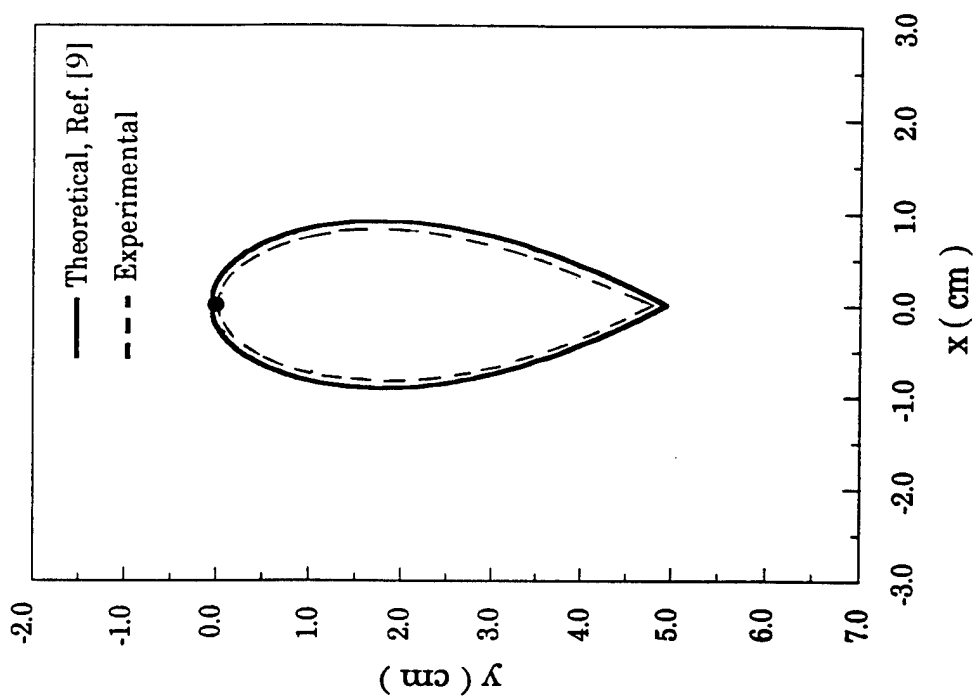


Figure 4 Comparison of the photographed shape of the liquid sheet with the theoretically predicted shape for  $D_j = 1.5$  mm,  $V_j = 2.49$  m/s,  $2\theta = 60^\circ$ .

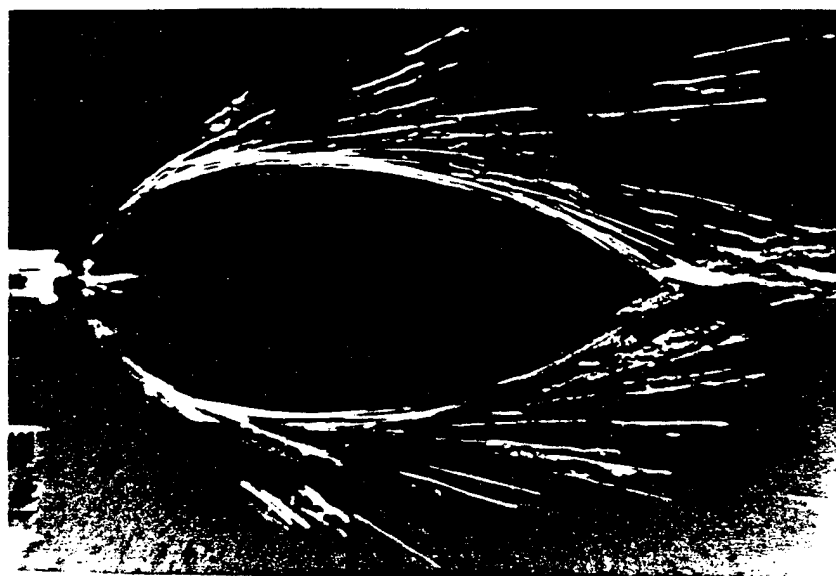
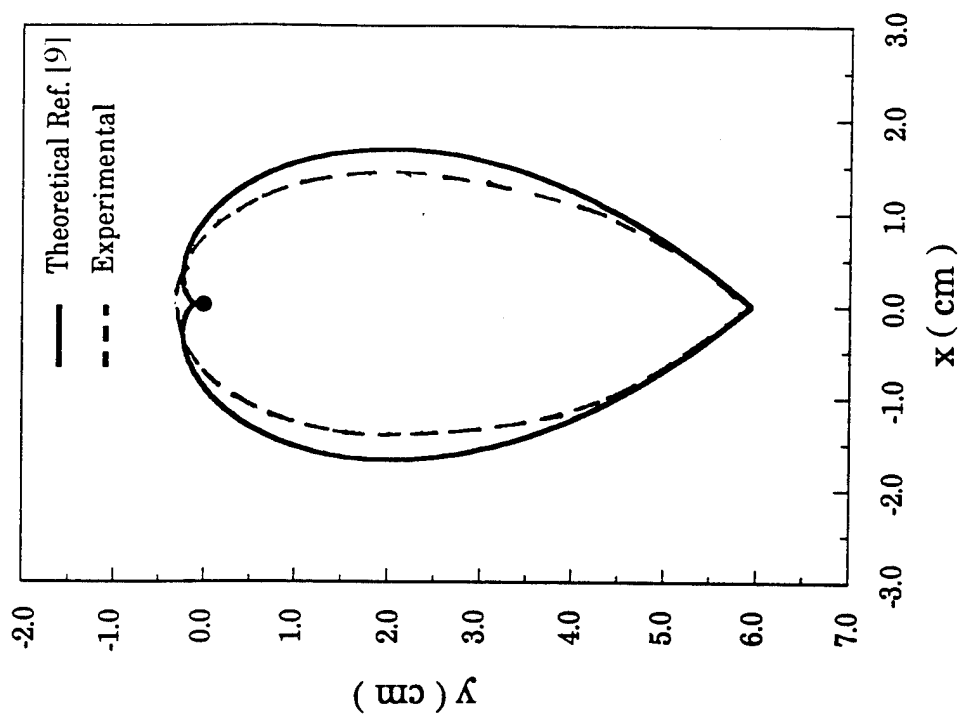


Figure 5 Comparison of the photographed shape of the liquid sheet with the theoretically predicted shape for  $D_j = 1.5$  mm,  $V_j = 2.49$  m/s,  $2\theta = 90^\circ$ .

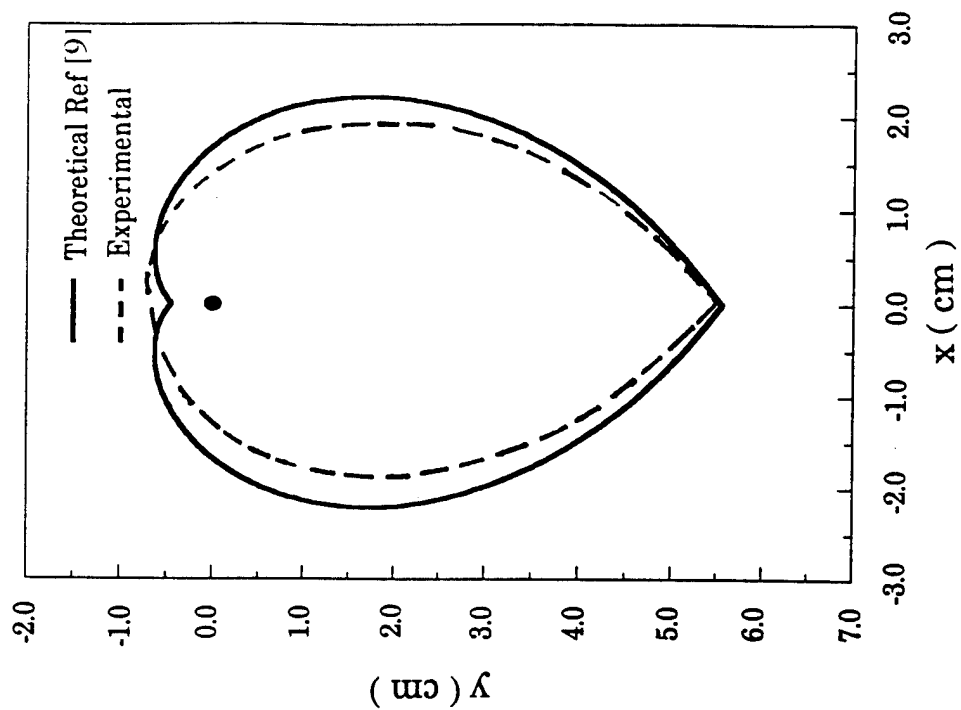
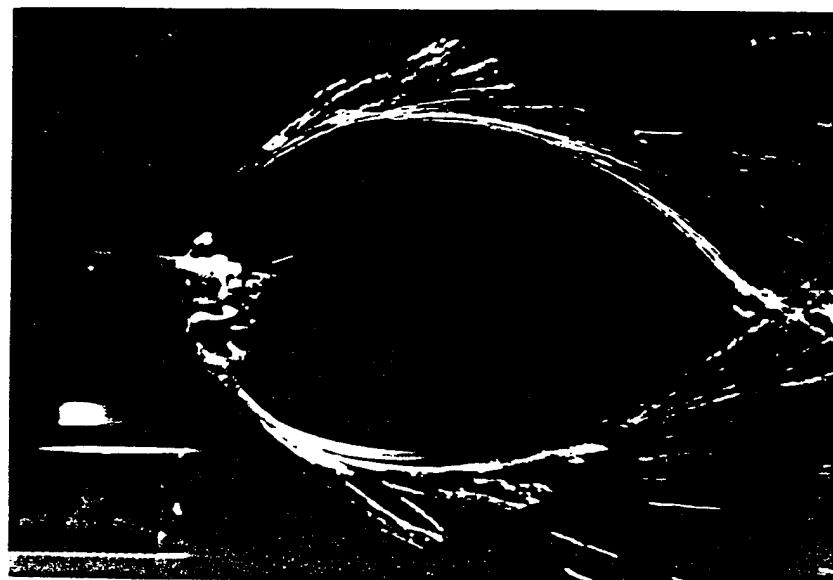
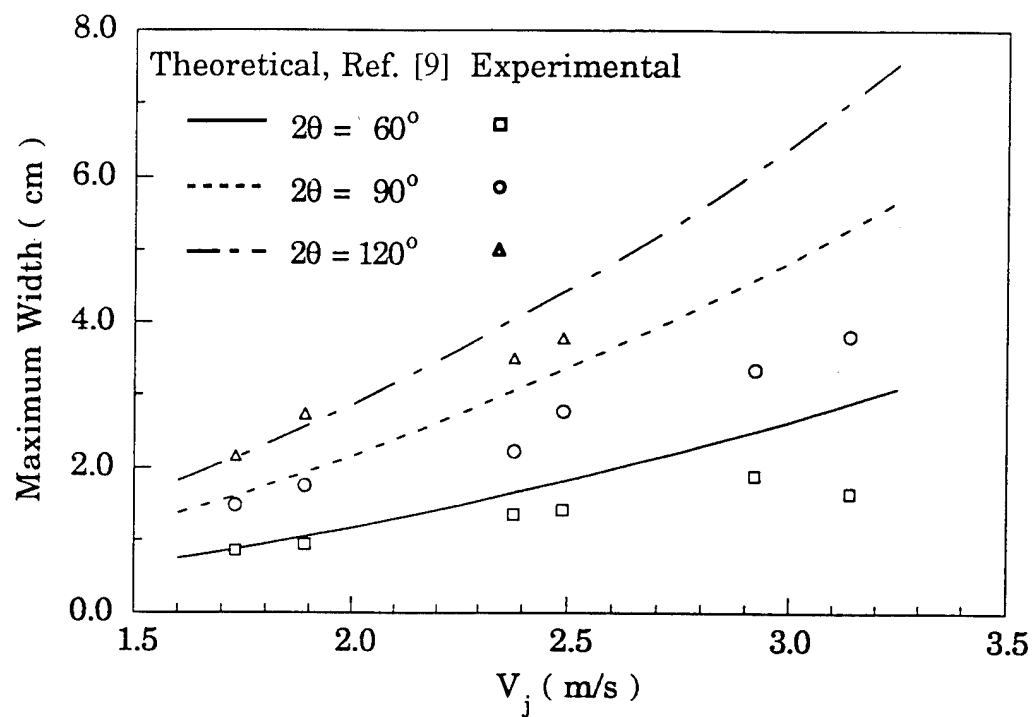
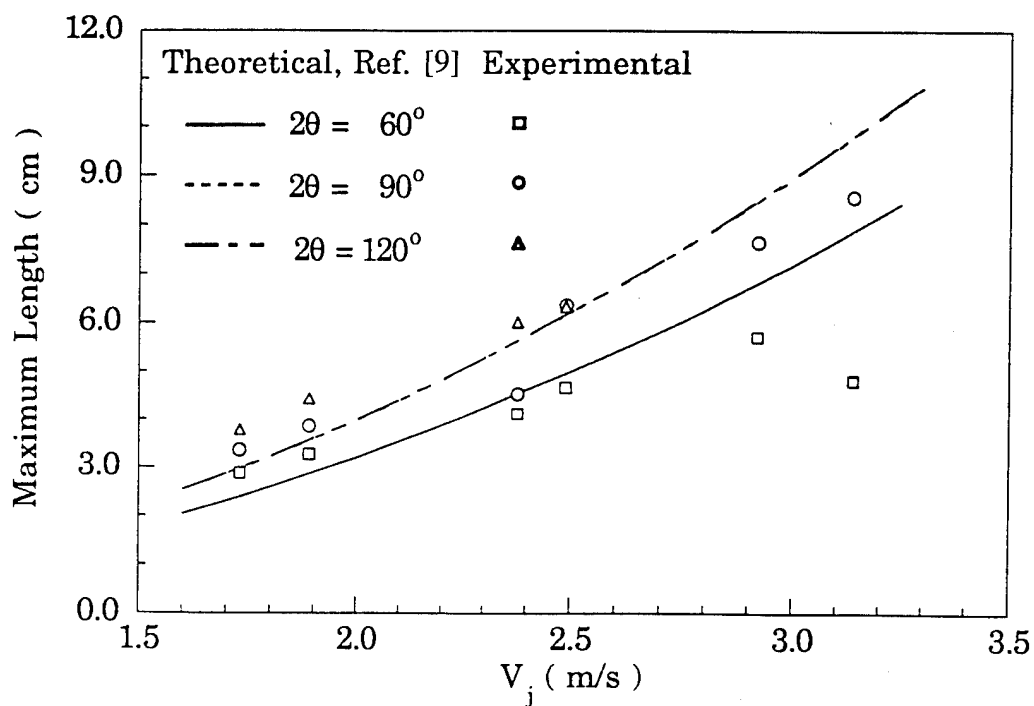


Figure 6 Comparison of the photographed shape of the liquid sheet with the theoretically predicted shape for  $D_j = 1.5$  mm,  $V_j = 2.49$  m/s,  $2\theta = 120^\circ$ .



(a)

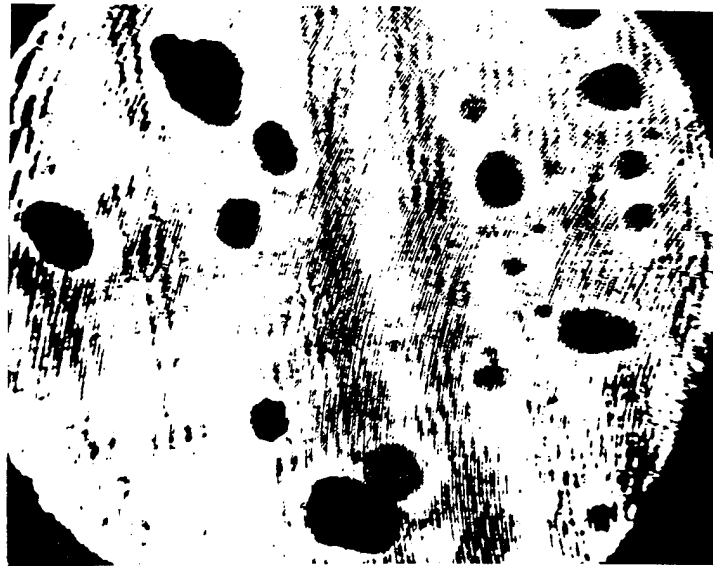


(b)

Figure 7 Comparison of the measured maximum width and length of the liquid sheet with theoretically predicted values for  $D_j = 1.5$  mm,  $V_j = 2.49$  m/s (a) maximum width (b) maximum length.



(a)



(b)

Figure 8 Typical photographs of a hologram revealing droplet images at two different locations for  $D_j = 1.5$  mm,  $V_j = 2.49$  m/s,  $2\theta = 120^\circ$  (a) upper right region of the sheet (  $x = 1.6$  to  $3.3$  cm,  $y = -0.5$  to  $2.0$  cm ) (b) lower left region (  $x = -2.5$  to  $-1.0$  cm,  $y = 4.0$  to  $5.7$  cm ).

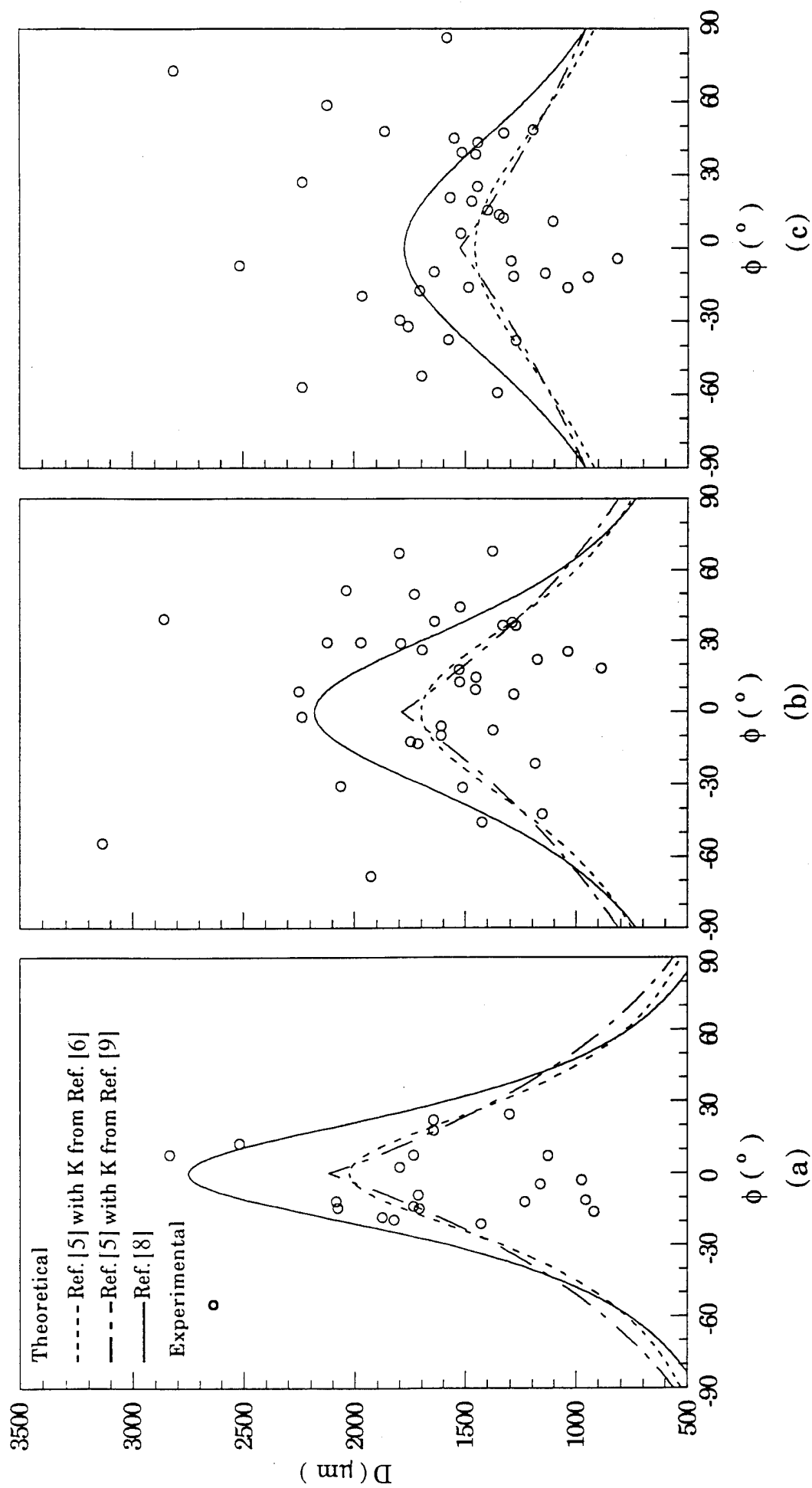


Figure 9 Measured droplet size distribution and comparison with theoretical predictions for  $D_j = 1.5$  mm,  $V_j = 2.5$  m/s (a)  $\theta = 60^\circ$  (b)  $\theta = 90^\circ$  (c)  $\theta = 120^\circ$ .

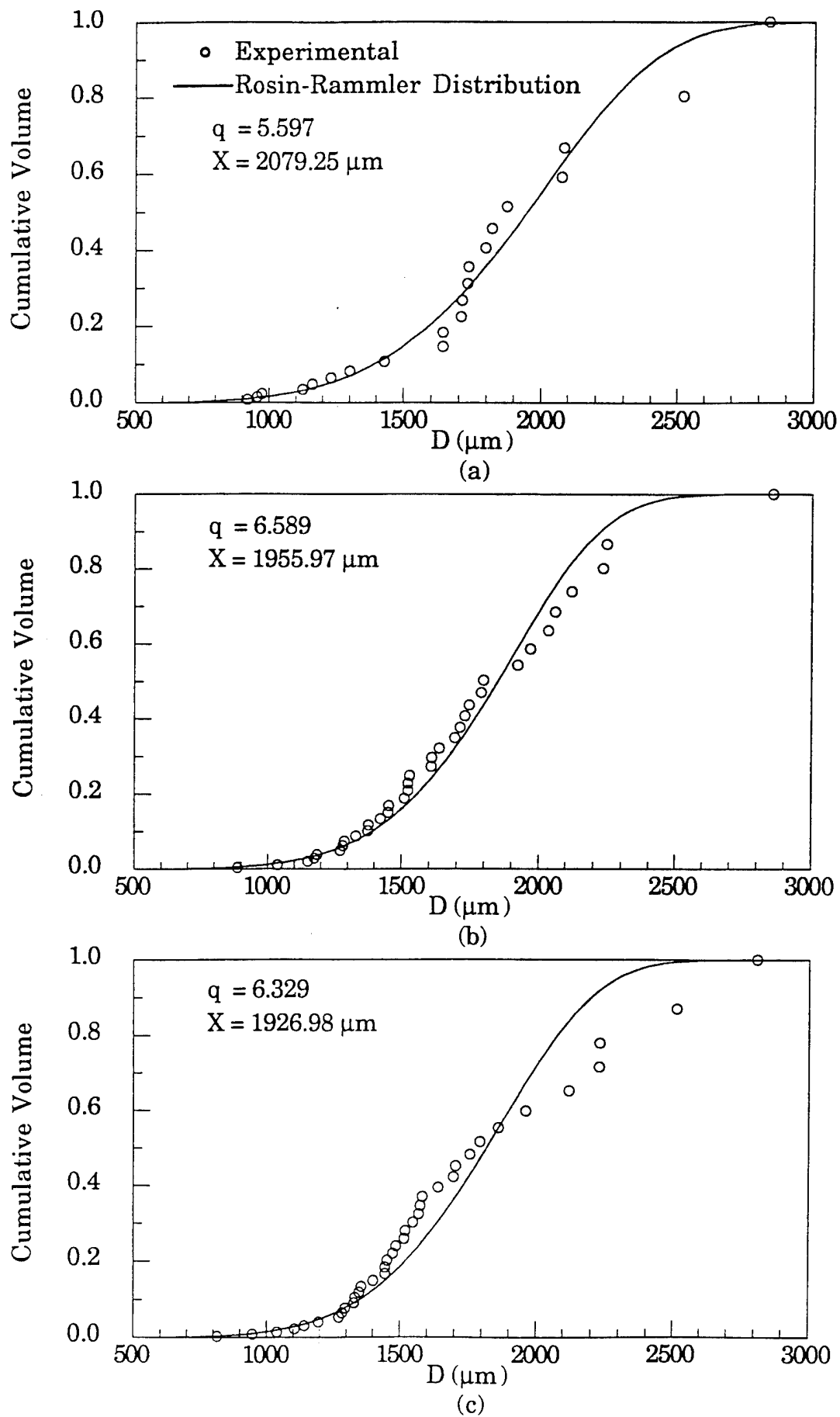


Figure 10 Cumulative droplet size distribution and comparison with Rosin-Rammler distribution for  $D_j$  = 1.5 mm,  $V_j = 2.5$  m/s (a)  $2\theta = 60^\circ$  (b)  $2\theta = 90^\circ$  (c)  $2\theta = 120^\circ$ .

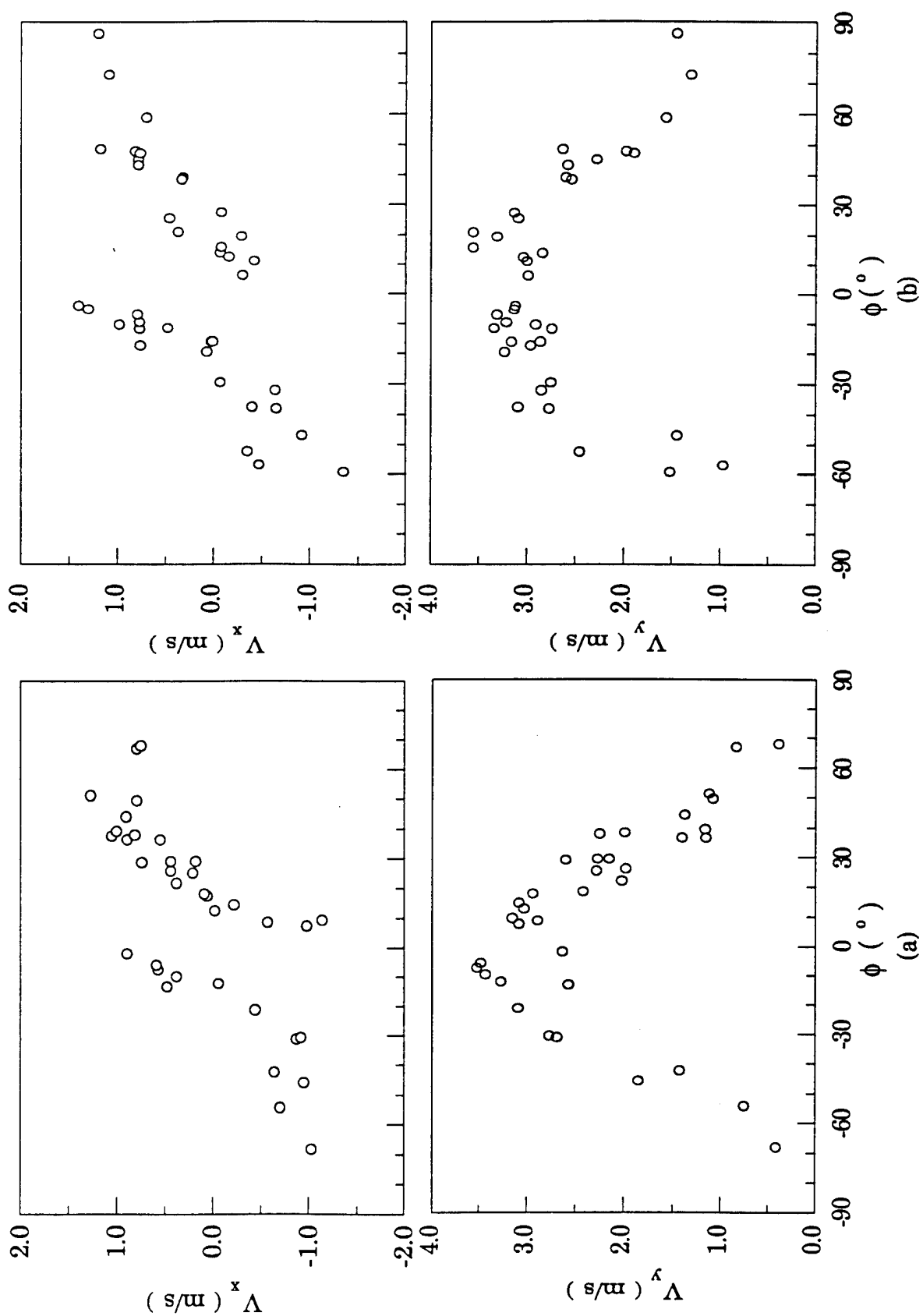
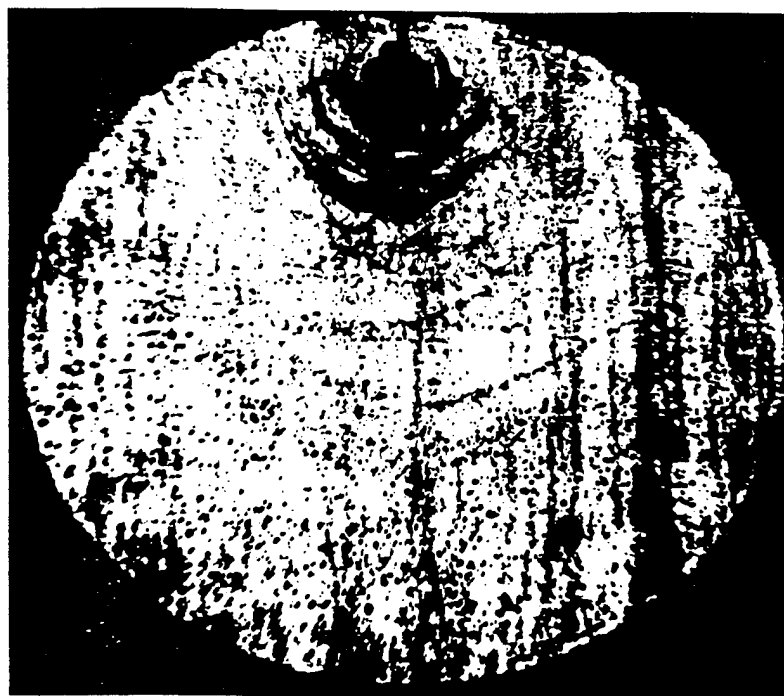
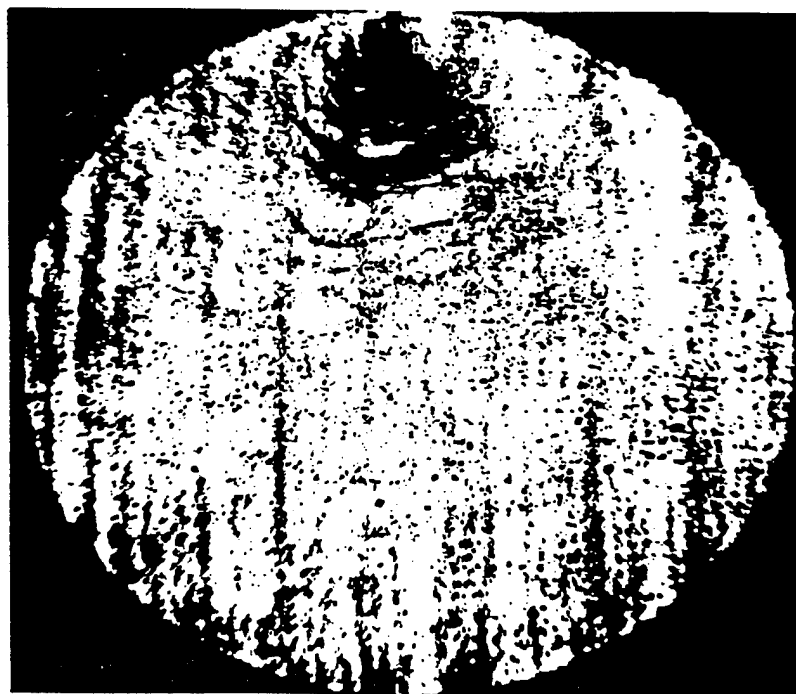


Figure 11 Measured velocity components of the liquid droplets for  $D_j = 1.5$  mm,  $V_j = 2.5$  m/s (a)  $\theta = 90^\circ$  (b)  $\theta = 120^\circ$ .



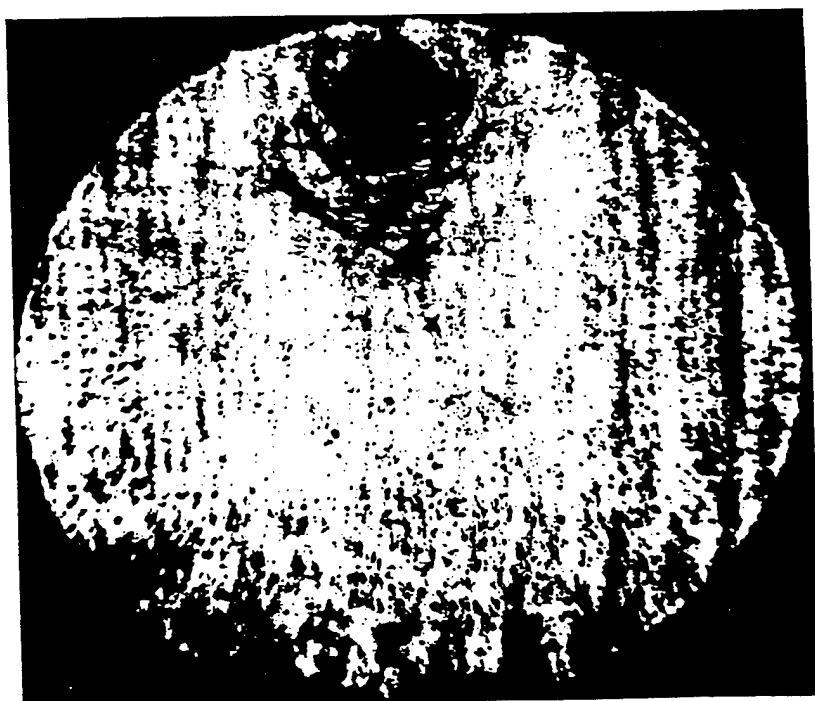
(a)



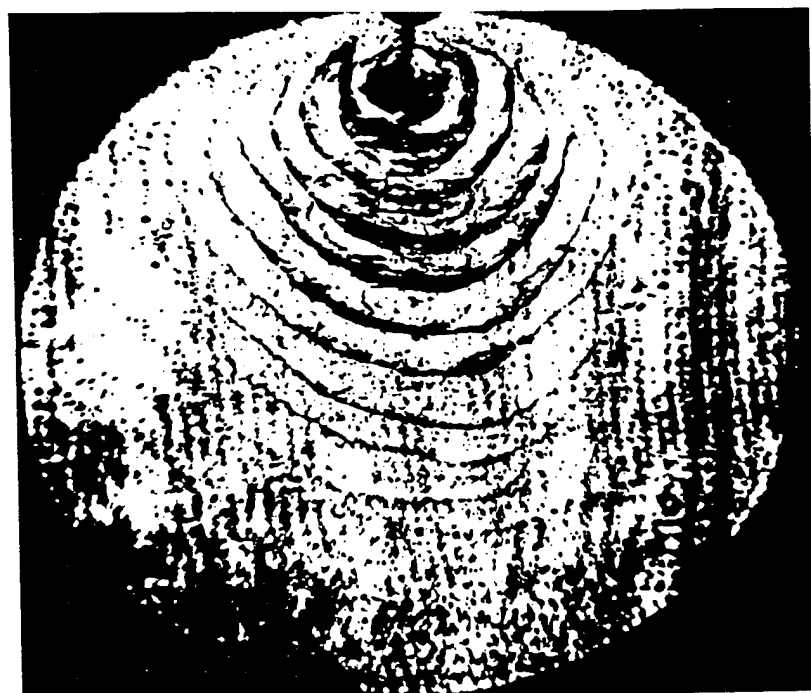
(b)

10 mm

Figure 12 Reconstruction photographs of spray holograms illustrating the overall spray pattern (a) water,  $D_j = 1.016 \text{ mm}$ ,  $2\theta = 90^\circ$ ,  $V_j = 12.0 \text{ m/s}$  (b) water,  $D_j = 1.016 \text{ mm}$ ,  $2\theta = 90^\circ$ ,  $V_j = 19.1 \text{ m/s}$  .



(c)



(d)

10 mm

Figure 12 (continued) (c) ethanol,  $D_j = 1.016 \text{ mm}$ ,  $2\theta = 90^\circ$ ,  $V_j = 11.9 \text{ m/s}$  (d) 59% glycerol,  $D_j = 1.016 \text{ mm}$ ,  $2\theta = 90^\circ$ ,  $V_j = 12.3 \text{ m/s}$ .

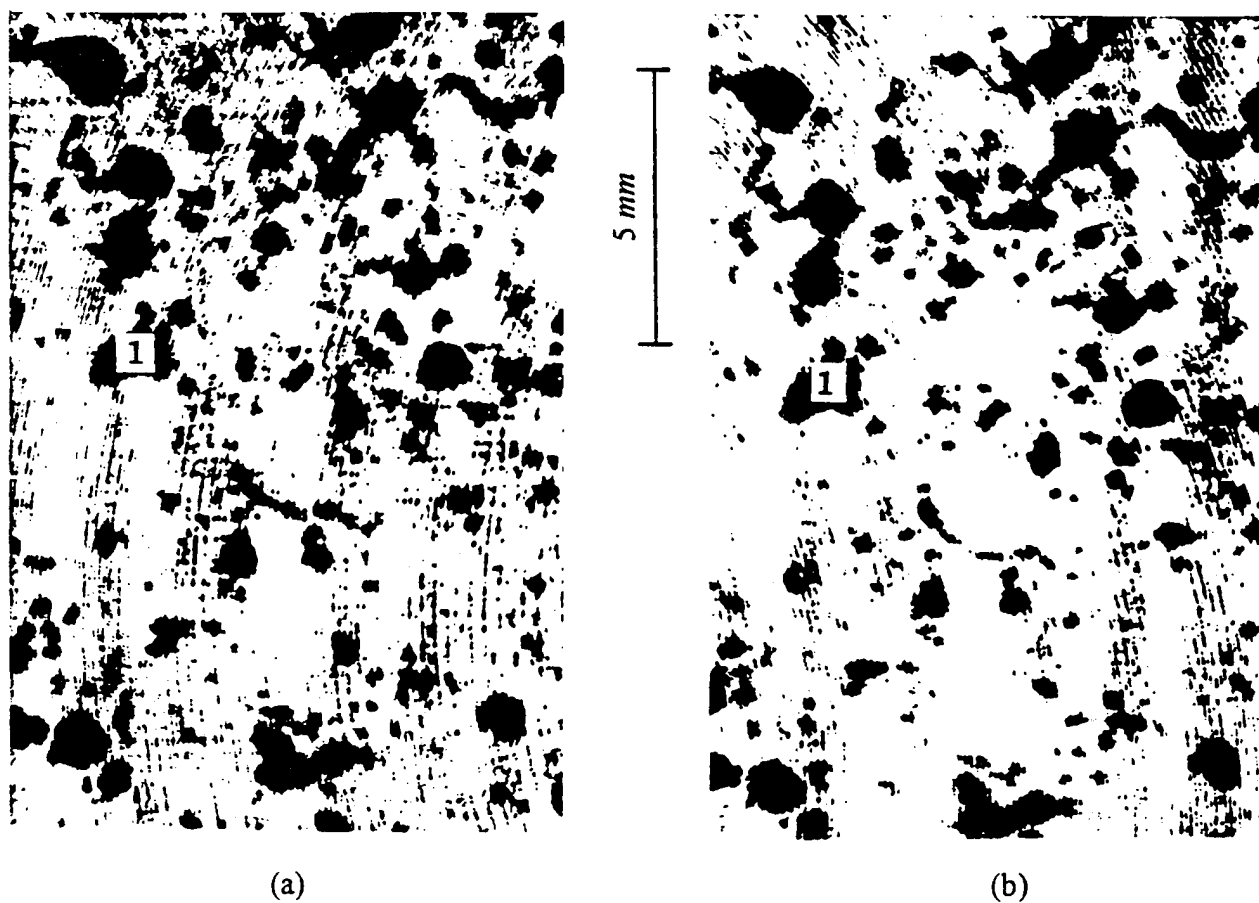


Figure 13 Photographs of hologram revealing droplet images at the first and the second pulse with  $D_j = 1.016 \text{ mm}$ ,  $2\theta = 60^\circ$ ,  $V_j = 12.0 \text{ m/s}$ ,  $(x, y) = (0.0 \text{ cm}, 4.0 \text{ cm})$  (a) droplet images at the first pulse (b) droplet images at the second pulse.

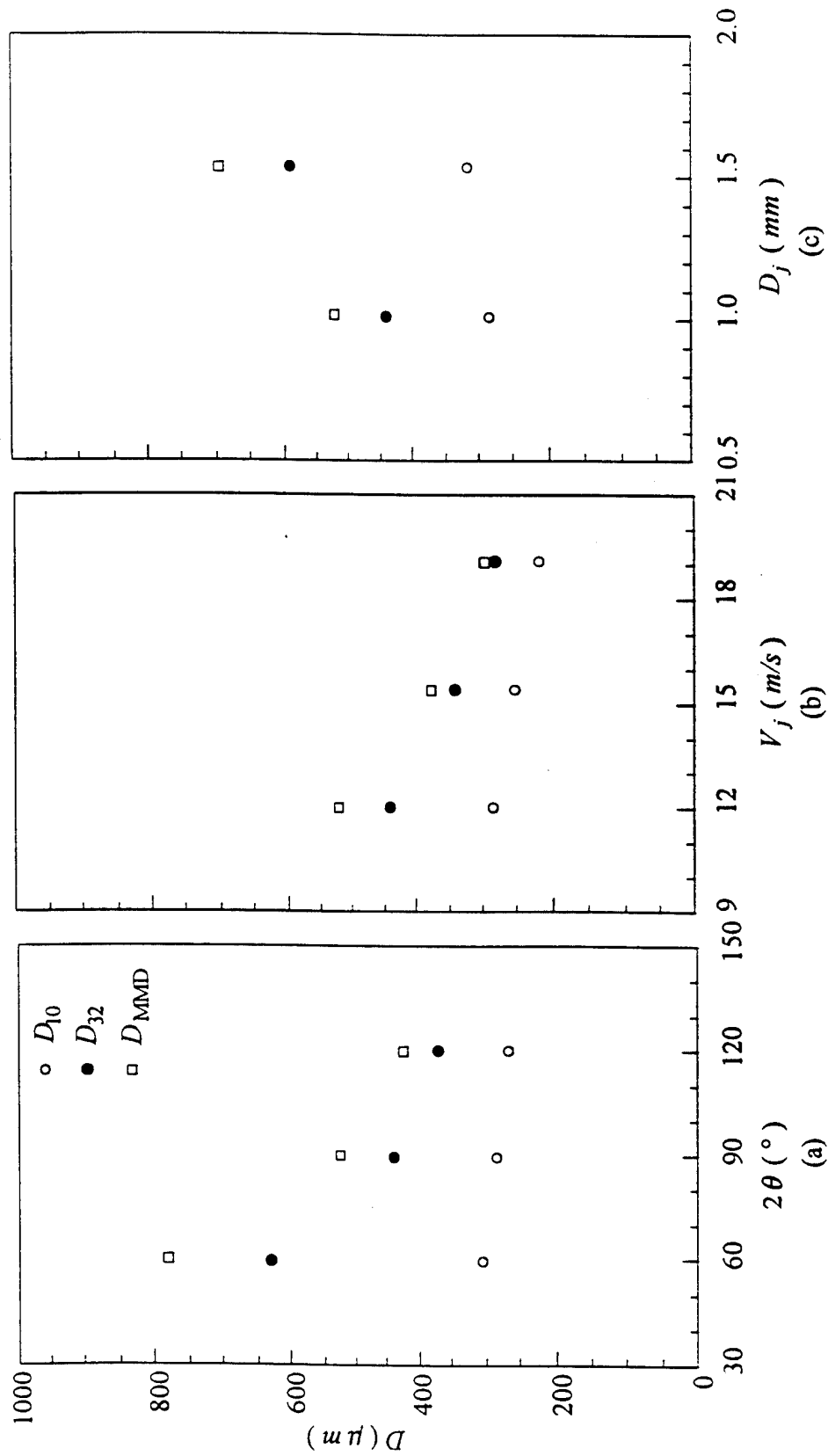


Figure 14 Effect of the impingement angle, liquid jet velocity, and orifice diameter on mean diameters (a)  $D_j = 1.016$  mm,  $V_j = 12.0$  m/s (b)  $D_j = 1.016$  mm,  $2\theta = 90^\circ$  (c)  $V_j = 12.0$  m/s,  $2\theta = 90^\circ$ .

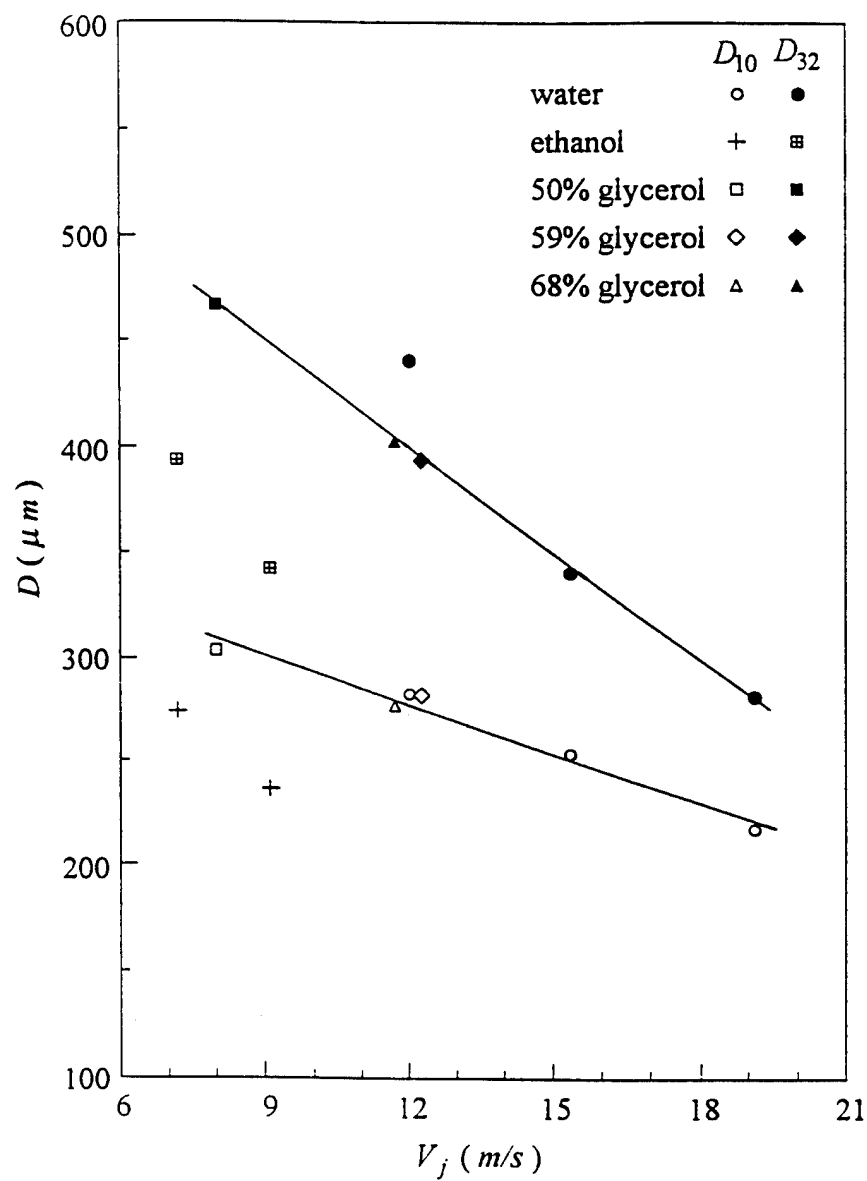


Figure 15 Effect of liquid properties on mean diameters for  $D_j = 1.016 \text{ mm}$ ,  $2\theta = 90^\circ$ .

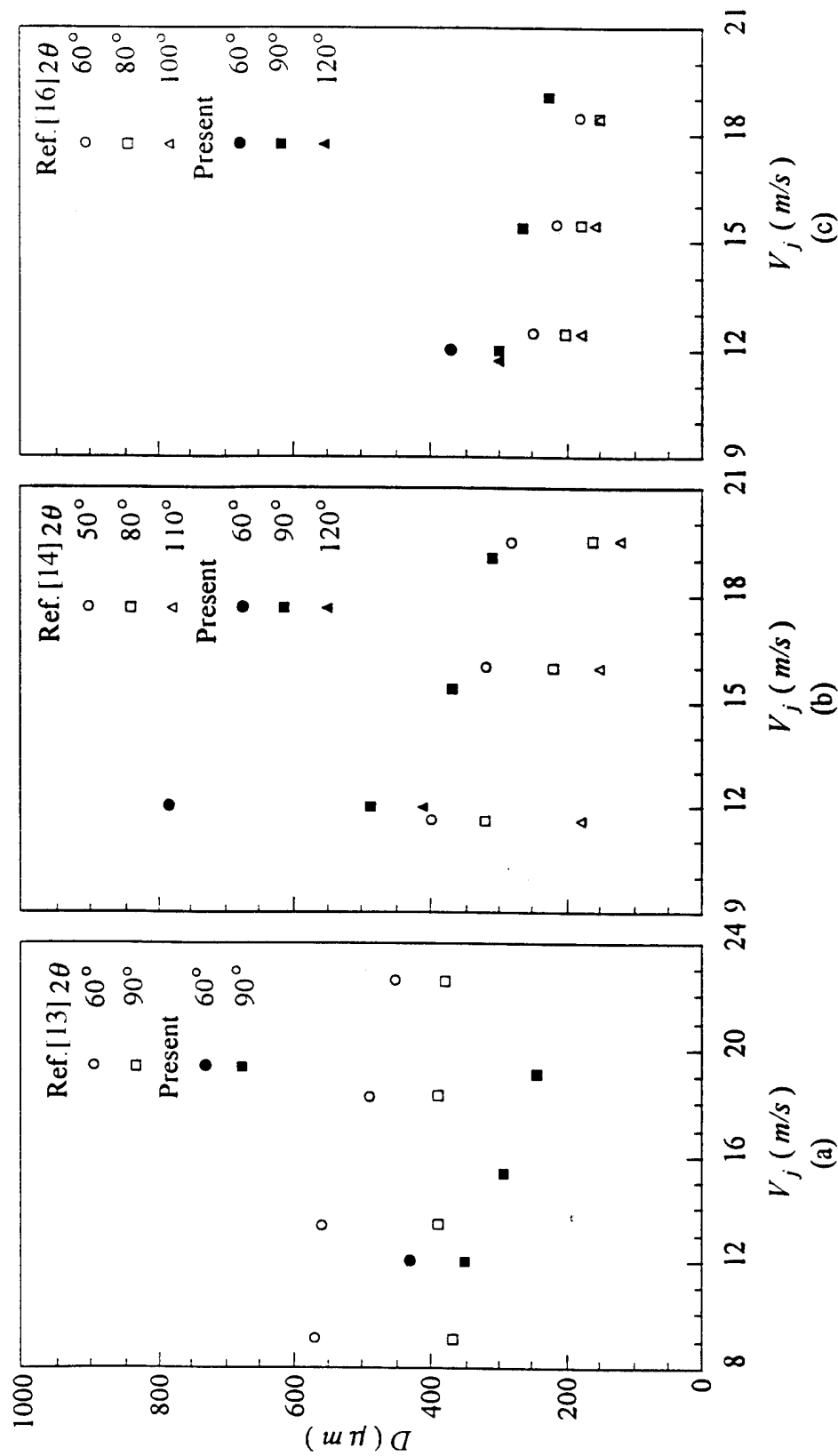


Figure 16 Comparison of the size measurement results with previous ones (a)  $D_{30}$  from Heidmann and Foster [13] (b)  $D_{32}$  from Dombrowski and Hooper [14] (c)  $D_{10}$  from Anderson et al. [16].

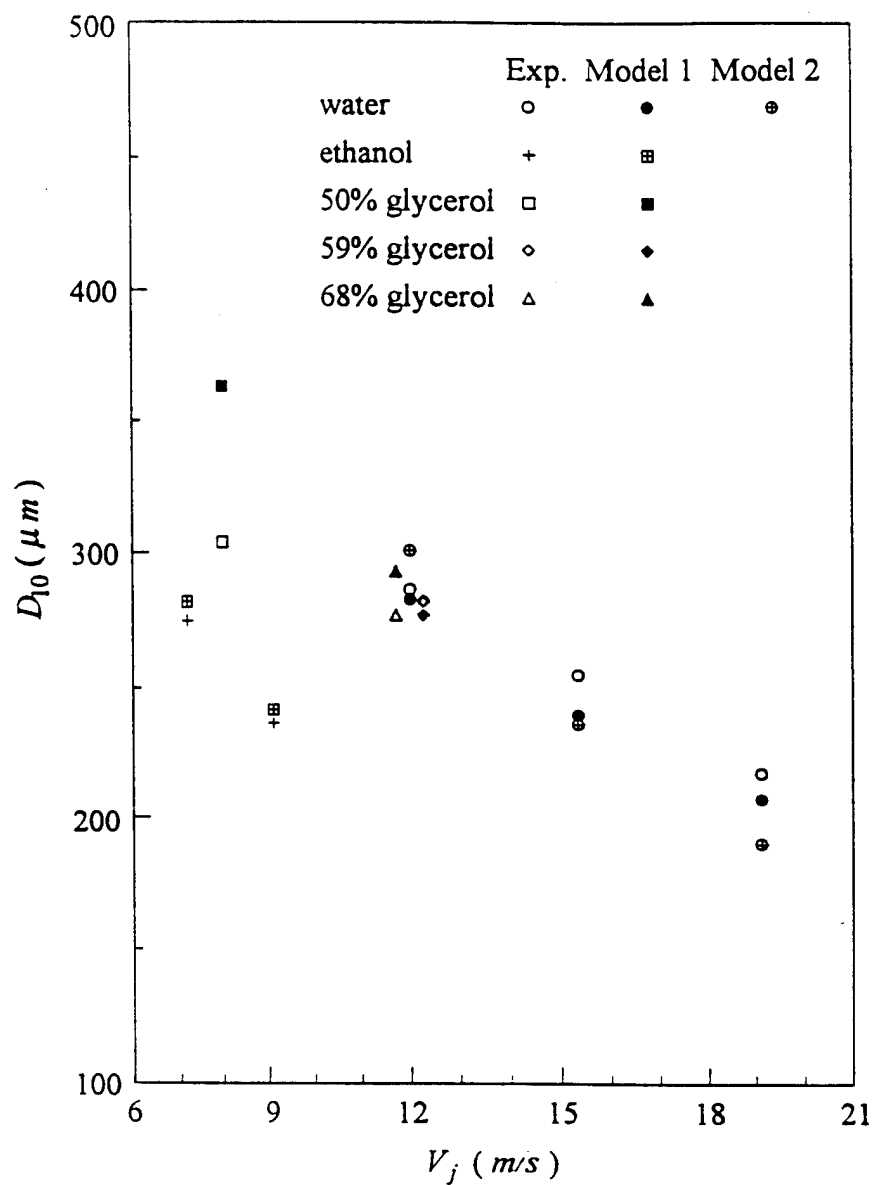


Figure 17 Comparison of measurement results for  $D_j = 1.016 \text{ mm}$ ,  $2\theta = 90^\circ$  with related theoretical predictions (Model 1 is based on Dombrowski and Johns' analysis [5] and Model 2 is the combination of Dombrowski and Johns' [5] and Adelberg's analysis [21,22]).

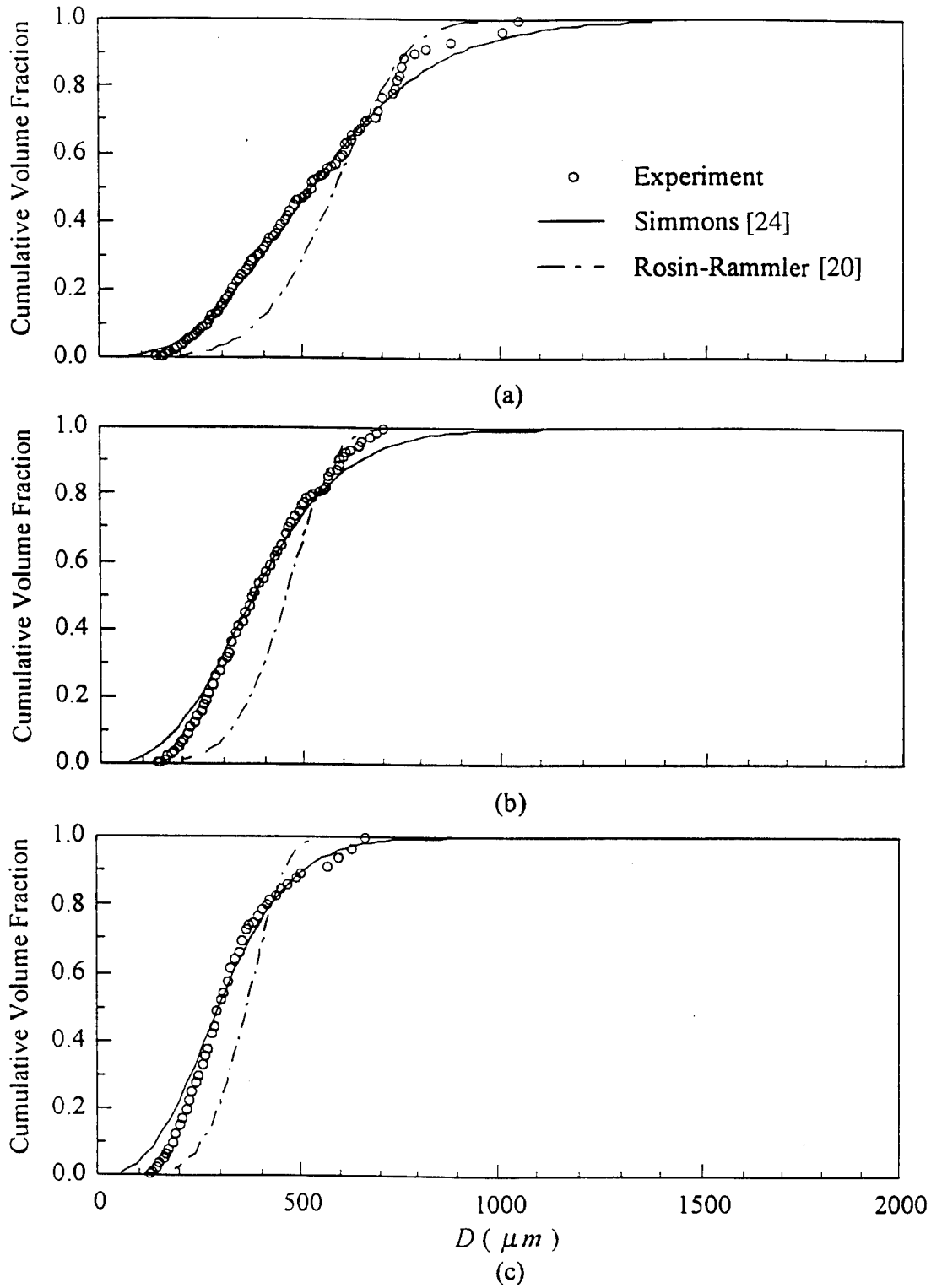


Figure 18 Comparison of cumulative volume distributions with the Simmons and Rossin-Rammler distributions for water,  $D_j = 1.016 \text{ mm}$ ,  $2\theta = 90^\circ$  (a)  $V_j = 12.0 \text{ m/s}$  (b)  $V_j = 15.4 \text{ m/s}$  (c)  $V_j = 19.1 \text{ m/s}$ .

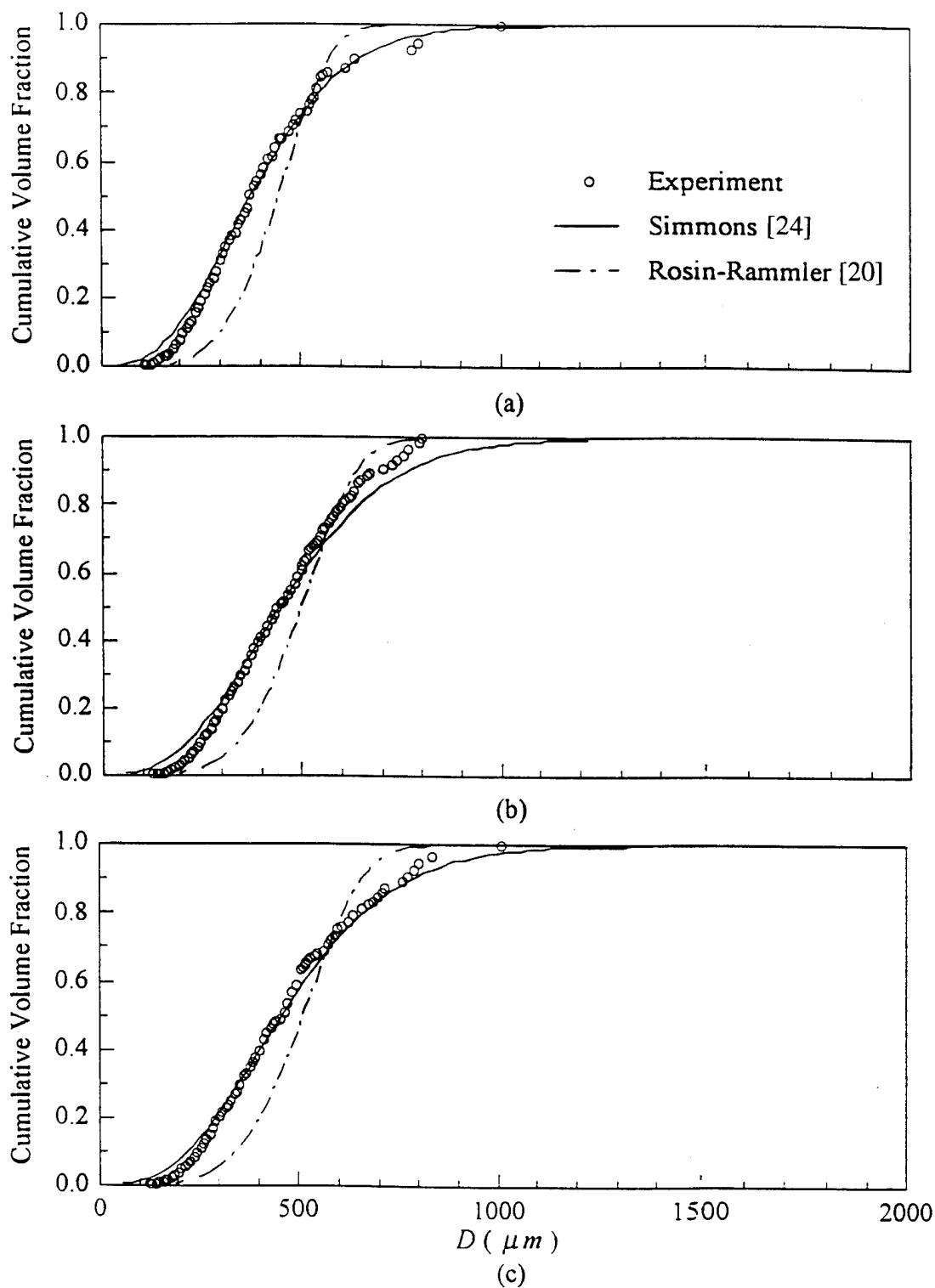


Figure 19 Comparison of cumulative volume distributions with the Simmons and Rosin-Rammler distributions for  $D_j = 1.016 \text{ mm}$ ,  $2\theta = 90^\circ$  (a) Ethanol,  $V_j = 11.9 \text{ m/s}$  (b) Glycerol (59 %),  $V_j = 12.3 \text{ m/s}$  (c) Glycerol (68 %),  $V_j = 11.7 \text{ m/s}$ .

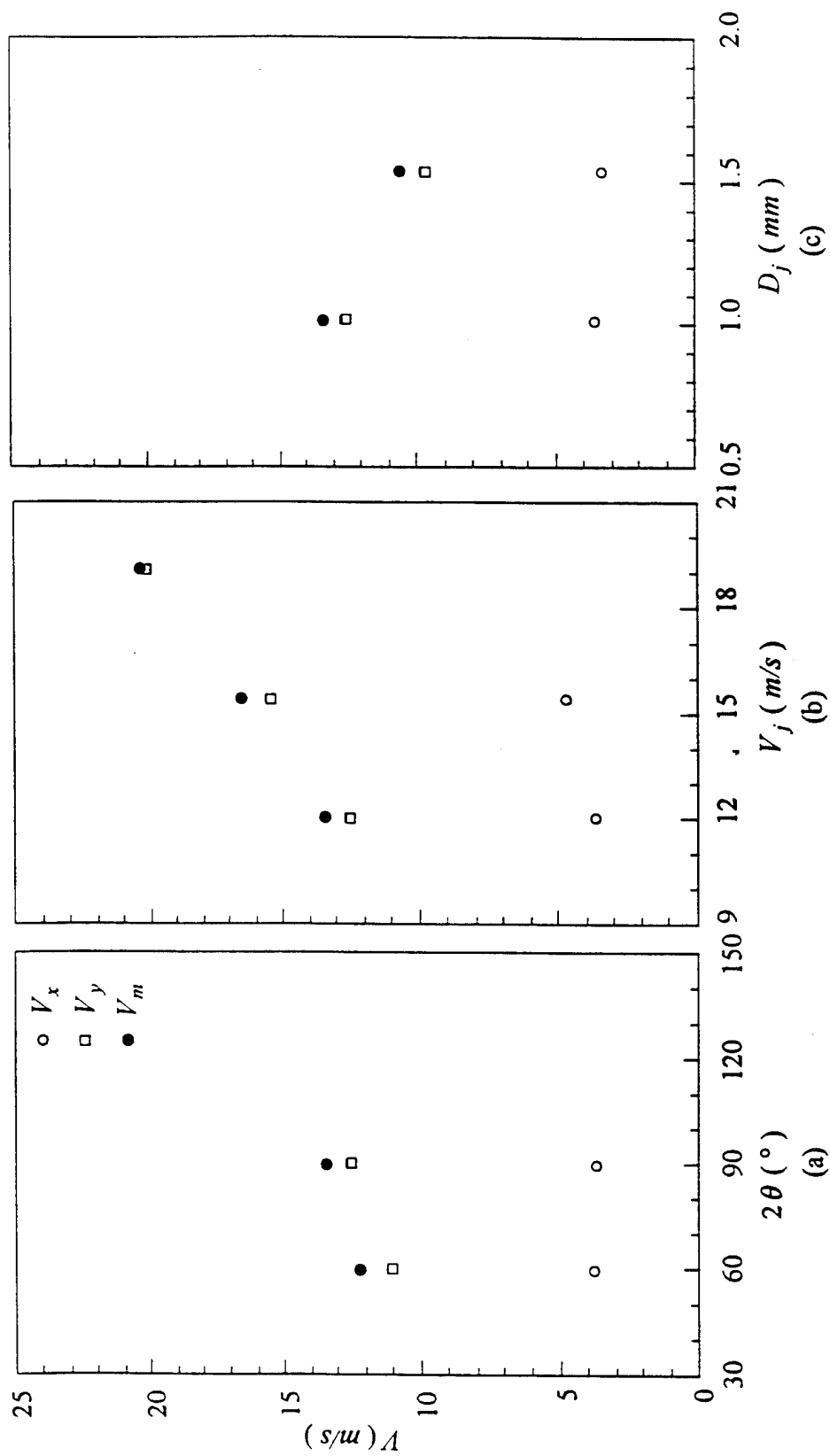


Figure 20 Effect of the impingement angle, liquid jet velocity, and orifice diameter on mean velocities  
 (a)  $D_j = 1.016 \text{ mm}$ ,  $V_j = 12.0 \text{ m/s}$  (b)  $D_j = 1.016 \text{ mm}$ ,  $2\theta = 90^\circ$  (c)  $V_j = 12.0 \text{ m/s}$ ,  $2\theta = 90^\circ$ .

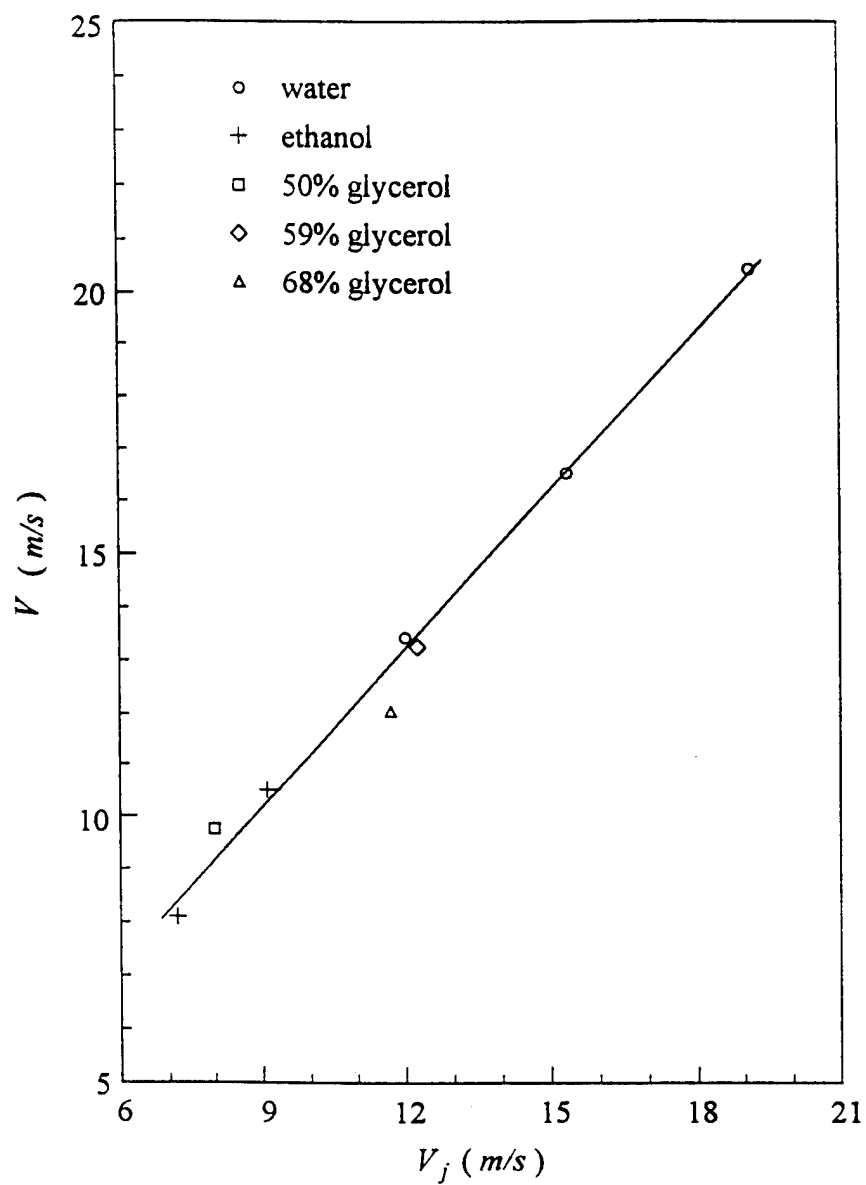


Figure 21 Effect of liquid properties on mean velocities for  $D_j = 1.016 \text{ mm}$ ,  $2\theta = 90^\circ$

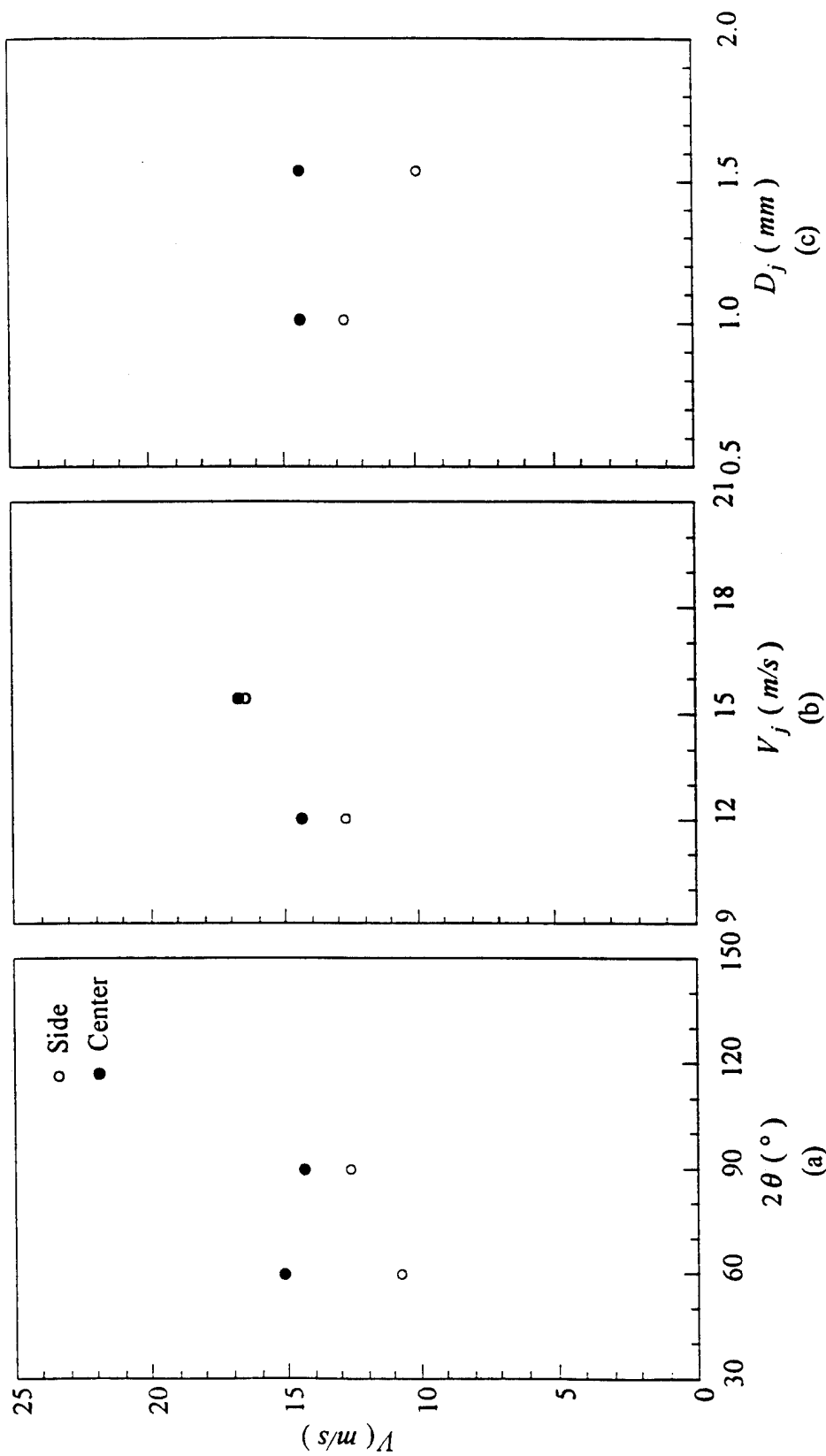


Figure 22 Droplet velocities for the center and side regions of the spray (a)  $D_j = 1.016$  mm,  $V_j = 12.0$  m/s (b)  $D_j = 1.016$  mm,  $2\theta = 90^\circ$  (c)  $V_j = 12.0$  m/s,  $2\theta = 90^\circ$ .

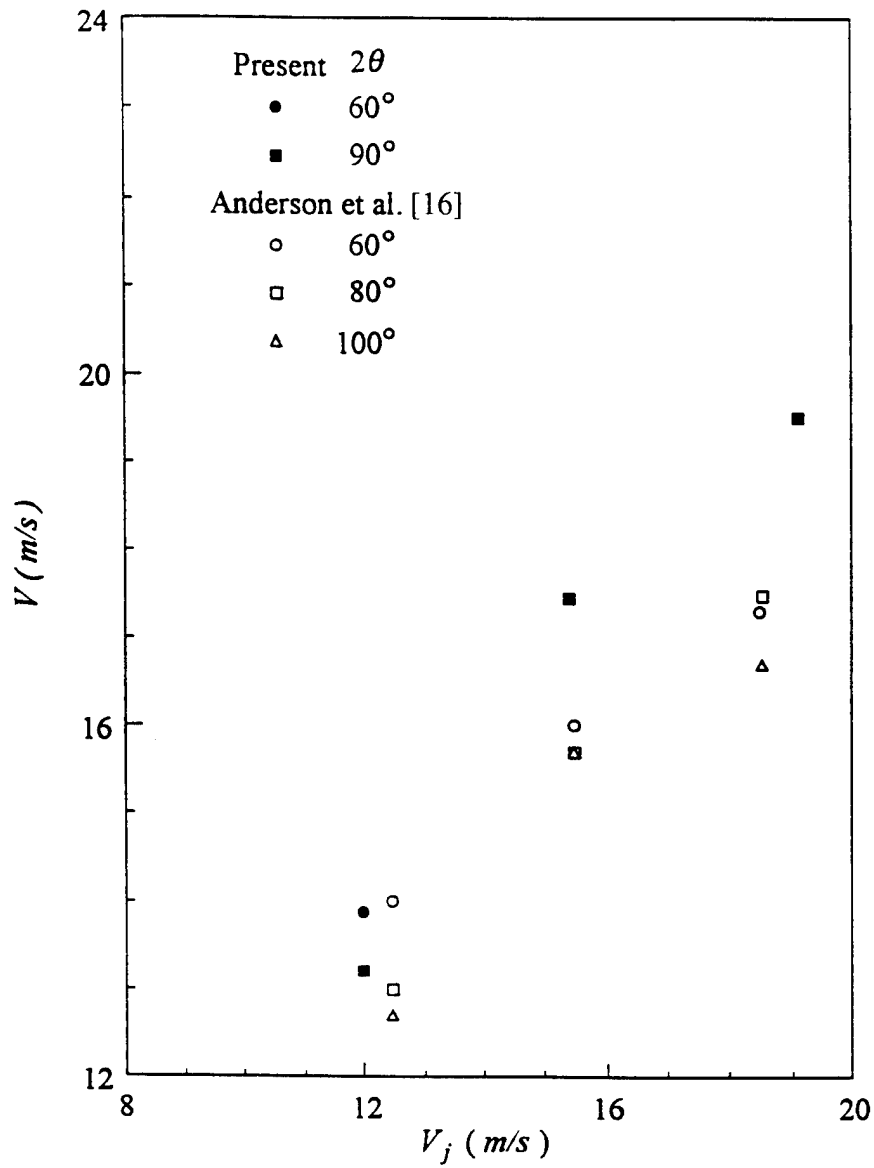
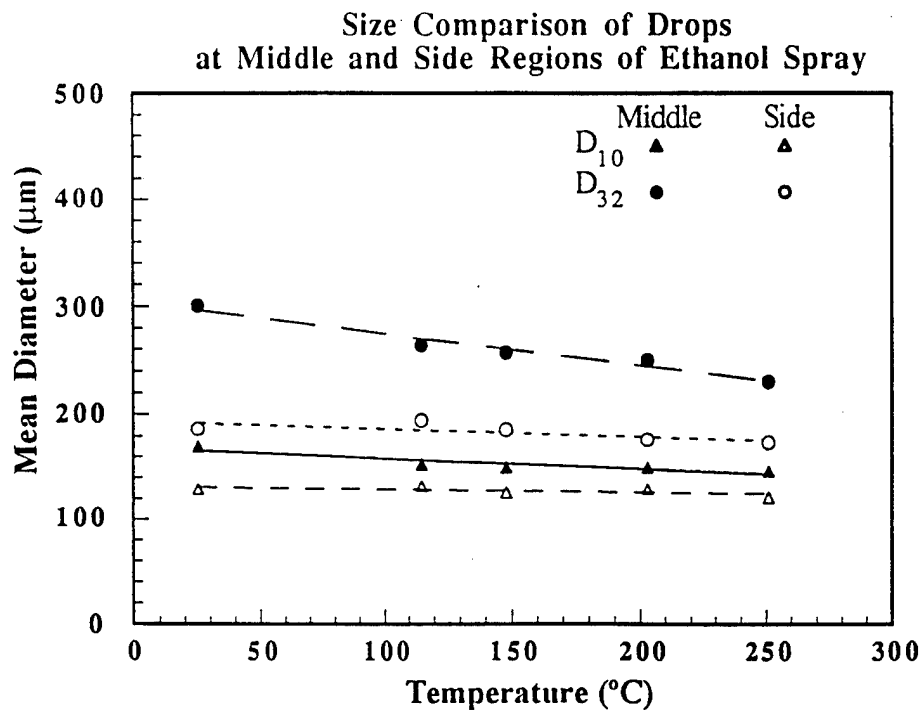
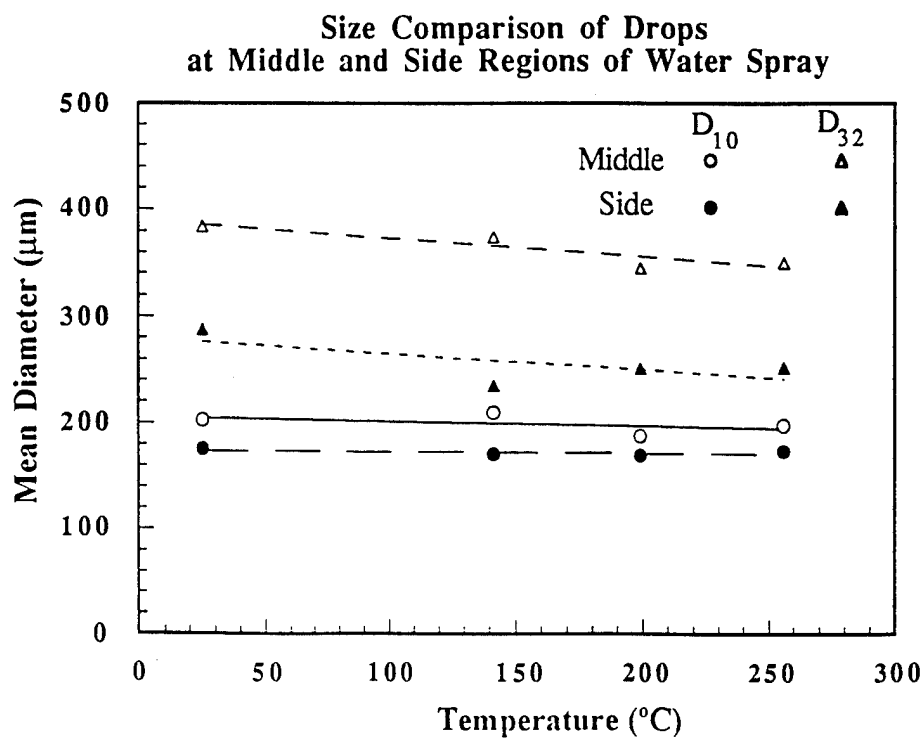


Figure 23 Comparison of velocity measurement results with those of Anderson et al. [16] ( $D_j = 1.016$  and  $0.64$  mm for the present study and Anderson et al. [16], respectively).

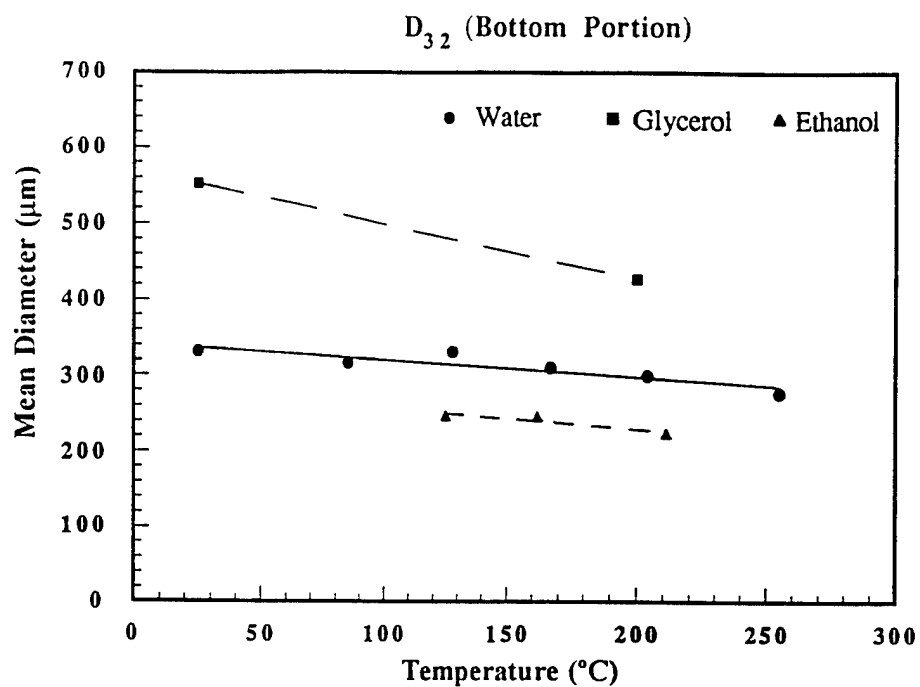


(a)

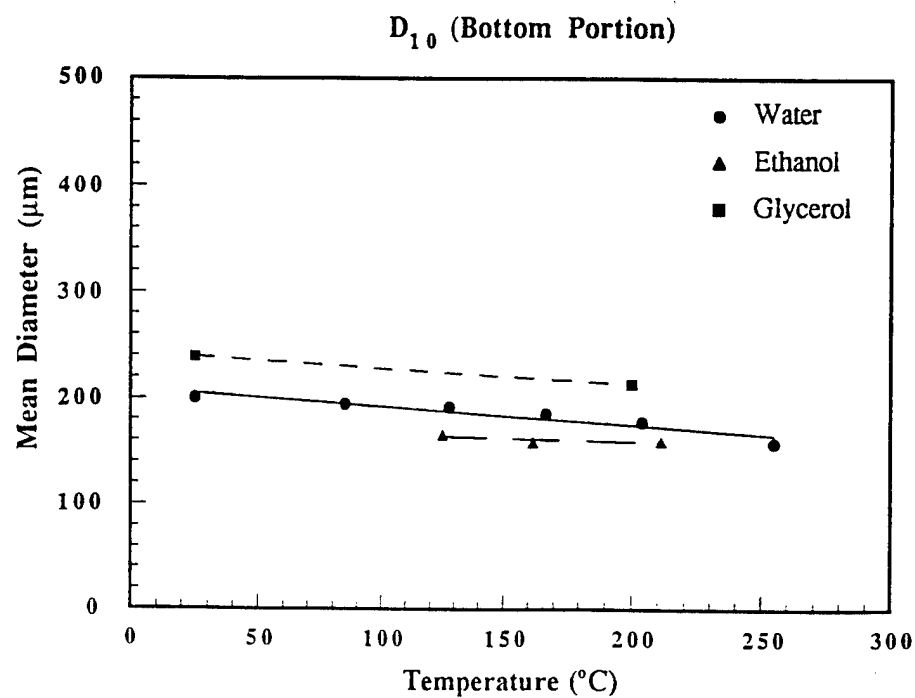


(b)

Figure 24 Comparison of the length and Sauter mean versus temperature in the side and middle regions of the impinging jet sprays for (a) ethanol and (b) water.



(a)



(b)

Figure 25 Comparison of ethanol, glycerol and water droplet size versus temperature in the bottom region of the spray for (a) Sauter mean and (b) length mean.

## LIST OF PROFESSIONAL PERSONNEL AND PUBLICATIONS

### Publications in Refereed Journals

1. B. Kang, D. Poulikakos and Y. Shen, "Holography Experiments in the Breakup Region of a Liquid Sheet Formed by Two Impinging Jets," *Atomization and Sprays*, Vol. 5, pp. 387-402, 1995.
2. B. Kang and D. Poulikakos, "A Holographic Study of the Dense Spray Region Created by Two High-Speed Impinging Jets," *AIAA Journal of Propulsion and Power*, Vol. 12, No.2, March-April 1996 (to appear).
3. Y. Shen, C. Mitts and D. Poulikakos, "A Holographic Investigation on the Effect of Elevated Ambient Temperature on the Atomization Characteristics of Impinging Jet Sprays," submitted for publication to *Atomization and Sprays*.

### Graduate Students

1. Boseon Kang, "A Holographic Study of the Dense Spray Region Created by Two Impinging Jets," *Ph.D. Thesis*, University of Illinois at Chicago, 1995.
2. Yunbiao Shen, "A Holographic Study of Supercritical Liquid Jet Breakup in Rocket Propulsion," *Ph.D. Thesis*, University of Illinois at Chicago, in progress, to be completed December, 1996.

## **APPENDIX A**

## HOLOGRAPHY EXPERIMENTS IN THE BREAKUP REGION OF A LIQUID SHEET FORMED BY TWO IMPINGING JETS

**B. S. Kang, Y. B. Shen, and D. Poulikakos**

*Department of Mechanical Engineering, University of Illinois at Chicago, Chicago, Illinois*

*In this article an experimental study is presented of the problem of disintegration of a liquid sheet created by two impinging jets. Utilizing a novel pulse holography technique, measurements of the size and velocity of all the liquid elements around the edge of the sheet were performed. Existing theoretical predictions on the size and shape of the liquid sheet as well as on the size distribution of the droplets around the sheet boundary were also tested against the experimental measurements. For most part, the predicted shape agreed rather well with the experimental observations, qualitatively as well as quantitatively. As the impingement velocity increased, the agreement on the maximum sheet thickness deteriorated. The experiments clearly indicated that the liquid elements are largely nonspherical and that they exhibit large size variations in the neighborhood of the same location. This behavior is not predicted by the theories, which are based on the premise that the droplets at each angular position are monodispersed.*

### BACKGROUND AND REVIEW OF EXISTING THEORIES

Impinging-jet atomizers are commonly used in liquid-fueled rocket engines because they combine simplicity, good atomization characteristics, and, in the case where the impinging jets are "unlike" (fuel on oxidant), they yield good mixing simultaneously with the atomization. The impinging-jet injector achieves the disintegration of the liquid by the impingement (one upon the other) of two identical cylindrical jets. As shown in Fig. 1, an expanding sheet in the plane perpendicular to the plane containing the two liquid jets is produced when the jet velocity is low and liquid drops are disintegrating from the edge of this liquid sheet. The shape and the thickness of the sheet depend on the impingement angle  $\theta$ , the jet diameter  $D_j$ , the jet velocity  $V_j$ , and the physical properties of the liquid. The size and the distribution of the liquid droplets detaching from the rim of the liquid sheet depends on the thickness and orientation of this rim.

Several investigations have been conducted over the years with the aim of understanding the mechanism of disintegration of a liquid sheet and predicting its thickness, which plays a key role in the resulting droplet sizes. The mechanism of disintegration of a semiinfinite plane liquid sheet where the liquid has finite viscosity and the thickness of the sheet decreases with distance from the orifice was explored by Dombrowski and Johns [1]. They attributed the disintegration process to the rapidly growing surface waves resulting from interaction with the surrounding gaseous medium. Disintegration occurs when the wave amplitude reaches a critical value and ligaments of the sheet are torn off. These ligaments rapidly contract into unstable ligaments under the action of surface tension, and

---

The support of the Air Force Office of Scientific Research under grant number AFOSR F49620-92-J-0343 is gratefully acknowledged.

## NOMENCLATURE

$d_D$	droplet diameter	$V_y$	vertical velocity component of droplet (Fig. 1)
$d_L$	ligament diameter	$x$	horizontal coordinate from impingement point (Fig. 1)
$D_j$	orifice diameter	$X$	characteristic diameter in Rosin-Rammler distribution
$h$	liquid sheet thickness	$y$	vertical coordinate from impingement point (Fig. 1)
$h_e$	liquid sheet edge thickness	$\beta$	constant in Eq. (7)
$h_i$	initial thickness of liquid sheet	$\theta$	half of the impingement angle (Fig. 1)
$K$	coefficient defined in Eq. (2), from [1]	$\mu$	viscosity of liquid
$q$	Rosin-Rammler drop size distribution parameter	$\rho$	density of air
$Q$	liquid volume fraction containing drops of diameter smaller than $d_D$	$\rho_L$	density of liquid
$r$	radial distance from the impingement point	$\sigma$	surface tension of liquid
$r_e$	radial distance of liquid sheet edge	$\phi$	azimuthal angle measured counterclockwise from the $y$ axis (Fig. 1)
$R$	liquid jet radius	$\psi$	angle between the tangent to the rim of the cardioid sheet and the radius vector [7]
$s$	direction of motion of a plane liquid sheet [1]		
$U$	velocity of liquid sheet		
$V_j$	velocity of liquid jet		
$V_x$	horizontal velocity component of droplet (Fig. 1)		

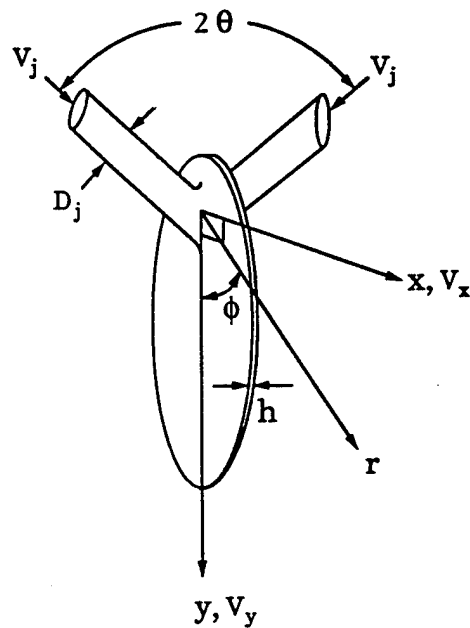


Fig. 1 Liquid sheet formed by impinging jets (abstracted from Hasson and Peck [2]).

droplets are produced by the breakup of these unstable ligaments. Dombrowski and Johns [1] proposed the following diameter for such ligaments:

$$d_L = 0.9614 \left( \frac{K^2 \sigma^2}{\rho \rho_L U^4} \right)^{1/6} \left( 1 + 2.6 \mu \sqrt[3]{\frac{K \rho^4 U^7}{72 \rho_L^2 \sigma^5}} \right)^{1/5} \quad (1)$$

where  $\sigma$  is the liquid surface tension,  $\mu$  is the liquid viscosity,  $\rho$  is the density of the surrounding medium,  $\rho_L$  is the density of the liquid, and  $U$  is the velocity of the liquid sheet moving in the  $z$  direction. The constant  $K$  is defined in the expression for the thickness of the liquid sheet  $h$ :

$$h = \frac{K}{s} \quad (2)$$

The (assumed uniform) diameter of the droplets disintegrating from the above ligaments is [1]

$$d_D = \left( \frac{3\pi}{\sqrt{2}} \right)^{1/3} d_L \left[ 1 + \frac{3\mu}{(\rho_L \sigma d_L)^{1/2}} \right]^{1/6} \quad (3)$$

The variation of the thickness of a liquid sheet created by two impinging jets with radial distance  $r$  and angular position  $\phi$  has been determined by Hasson and Peck [2]:

$$\frac{hr}{R^2} = \frac{\sin^3 \theta}{(1 - \cos \phi \cos \theta)^2} \quad (4)$$

Here,  $R$  is the radius of liquid jet. The basic idea of their analysis is that a cross section through the jet in a plane parallel to the sheet is an ellipse, and mass and momentum is conserved between an angular element in an ellipse and a corresponding element in the liquid sheet. Note that the expressions for the liquid sheet thickness [Eqs. (2) and (4)] have not been verified experimentally.

Couto and Bastos-Netto [3] combined Dombrowski and John's analysis [1] and Hasson and Peck's expression [2] for the thickness distribution of the liquid sheet to predict the droplet size distribution. The constant  $K$  required in Eqs. (1) and (2) is obtained from Eq. (4):

$$K = hr = \frac{R^2 \sin^3 \theta}{(1 - \cos \phi \cos \theta)^2} \quad (5)$$

Note that the coordinate  $s$  in Eq. (2) is replaced by  $r$  in Eq. (5) in order to be consistent with the notation of the direction of motion of the liquid in the sheet in Fig. 1.

Clark and Dombrowski [4] obtained an expression for the size of droplets formed from the rim of a fan spray sheet. They used a perturbation analysis based on total energy conservation for inviscid flow. Their correlation, including a constant obtained from experimental data, reads

$$d_D = 2.41 \times 10^6 \left( \frac{\sigma}{\rho_L} \right)^{1/9} \left( \frac{K^2}{U} \right)^{2/9} \quad (6)$$

This expression for the droplet size is more applicable to the droplets generated by two impinging jets because it considers droplets shedding tangentially from the edge of an oval liquid sheet, whereas Dombrowski and Johns [1] considered droplets generated at the leading edge of a semiinfinite liquid sheet.

Ibrahim and Przekwas [5] obtained theoretical expressions for the thickness and the shape of the liquid sheet. They adopted the expression for the initial sheet thickness obtained by Naber and Reitz [6] in their study of engine spray/wall impingement. This expression reads

$$h_i = \left( \frac{\beta R \sin \theta}{e^\beta - 1} \right) e^{\beta(1 - \phi/\pi)} \quad (7)$$

where  $\beta$  is determined from mass and momentum conservation. The thickness at any position  $r$  is expressed as

$$h = \frac{R/\sin \theta}{r} h_i \quad (8)$$

Another value for the constant  $K$  required in Eqs. (1) and (2) is obtained from Eq. (8):

$$K = h r = \frac{R}{\sin \theta} h_i \quad (9)$$

To predict the shape of the liquid sheet, they used Taylor's expression [7] for the thickness at the edge of the sheet. Taylor showed that the form of cardioid waves that can remain at rest to form the boundary of the liquid sheet is described by

$$h_e = \frac{2\sigma}{\rho_L U^2 \sin^2 \psi} \quad (10)$$

where  $\psi$  is the angle between the wave front and the radius vector. They developed an expression for  $\psi$  satisfying all boundary conditions:

$$\psi = \left( \frac{\pi}{2} \right) e^{[\ln(2\theta/\pi)](1 - \phi/\pi)} \quad (11)$$

The shape of the liquid sheet can be predicted by calculating the radial distance  $r_e$  between the edge of the sheet and the point of impact from Eq. (8) utilizing Eqs. (7), (10), and (11):

$$r_e = \frac{R}{\sin \theta} \frac{h_i}{h_e} \quad (12)$$

It is worth noting that experimental results were recently reported [8] for the atomization created by moderate and high-speed impinging jets. These results are not discussed here in detail because the present study focuses on low-speed jet impingement.

Experimental verification of the theoretical predictions discussed above is scarce. The work presented in this article aims at this deficiency. To this end, this study reports the main results of an experimental investigation, based on pulse holography, for the determination of the dimensions of the liquid sheet as well as the size distribution and velocity of the liquid droplets generated at the edge of this sheet. The experimental results for the sheet size and shape as well as for the droplet size are used to test many of the aforementioned theoretical predictions. Since the theories are for the low-speed impingement regime, the experiments had to be designed for the same impingement velocity regime. In addition, a natural progression requires understanding of the low-speed impingement process before embarking on the study of the more complex high-speed impingement process.

## EXPERIMENTS

### Impinging Jet Apparatus

The experimental apparatus for two impinging jets is shown schematically in Fig. 2. High-pressure  $N_2$  gas from a  $N_2$  gas cylinder is used to pressurize a water reservoir. The

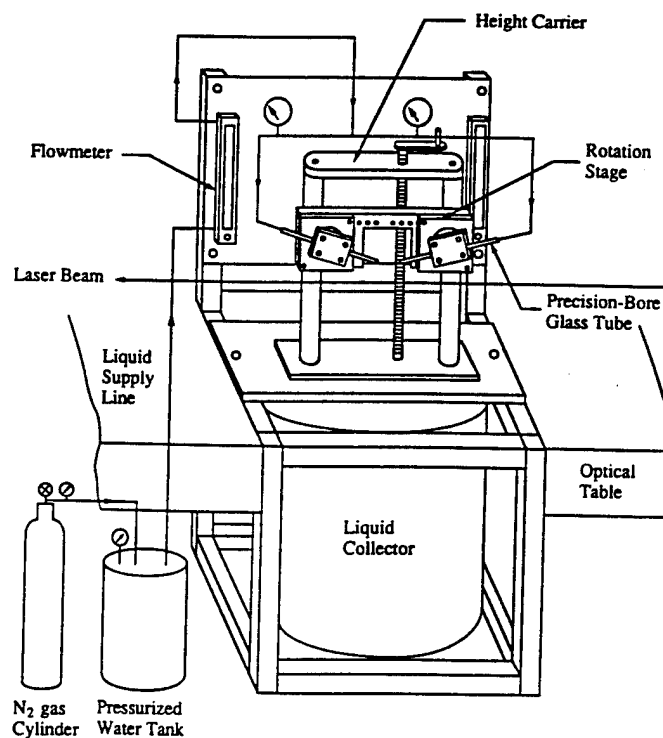


Fig. 2 Schematic of the experimental apparatus.

liquid flow from the flow meter passes through an on-off valve and is divided into two identical branches for the two individual impinging liquid jets. Precision-bore glass tubes are used as the impinging jet injectors. These tubes feature highly accurate inner diameter despite their small size and are practically free from surface roughness problems. The inner diameter of each tube is 1.534 mm and its length 15.24 cm. A 5.08-cm-long, 0.635-cm-O.D. copper tube bonded at one end of each glass tube is connected to the liquid supplying plastic tube.

The injector is placed through a hole in a square aluminum block mounted on a rotation stage by four threaded rods. Each injector can slide freely and be fixed by three set screws to adjust the preimpingement length, defined as the length from the liquid jet exit to the impacting point of the obliquely colliding liquid jets. A very accurate adjustment method is required to assure that the axes of the two liquid jets exist on the same plane. Otherwise, the liquid sheet produced by the two impinging jets will not be perpendicular to the plane containing the jets. Four very finely threaded rods mounting the aluminum block to the rotation stage are used to fine-tune the liquid jet plane so that a "perfect" liquid sheet is created normal to the jet plane. The impingement angle, defined as half the angle between the jets, can be adjusted accurately by the rotation stage. The falling liquid is collected into a cylindrical water tank. Distilled water was used as the working fluid in all the experiments.

### Optical System for Hologram Recording

A novel technique was employed for the recording of the holograms used for the velocity measurements. This technique allows for the separate reconstruction of the spray image obtained by different pulses of the light source, an advantage that greatly facilitates the image processing of the holograms, particularly in dense sprays. Figure 3a shows the schematic layout of the holographic recording system. The light source is a ruby laser, either single or double pulsed, of 2 J output energy, which can generate a 694-nm-wavelength, vertically polarized laser beam. The pulse interval for the velocity measurements was selected to be (after a trial-and-error process) 400  $\mu$ s and the pulse duration 30 ns, which is short enough to freeze the motion of the liquid sheet or droplets. For the alignment of all optical components before firing the ruby laser, a He-Ne alignment laser that is mounted on the ruby laser box is used. A Pockels cell is used to change the polarization direction of the laser light of the first pulse. To drive the Pockels cell, a high-voltage pulse generator is utilized. The input signal to this device comes from a synchronization socket in the ruby laser control box. To change the polarization direction of the first pulse only, the Pockels cell was activated just before the first pulse, throughout the duration of the first pulse. To this end, the high-voltage pulse generator yields an adjustable input/output delay and pulse width, from 0.2 ms to 1.2 ms and from 40 ns to 1.2 ms, respectively. The output pulse amplitude ranges from 2.0 kV to 7.5 kV.

A beam splitter is used to divide the incoming laser beam into an object beam and a reference beam. The object beam is expanded and collimated by a Galilean-type beam expander. The diameter of the object beam is increased up to 10.0 cm to cover entirely the spray region of interest. This plane wave passes through the spray region and finally is intercepted at the 10.16-cm  $\times$  12.7-cm holographic glass plate. The reference beam passes through a cube-type polarization beam splitter. This beam splitter reflects the vertical

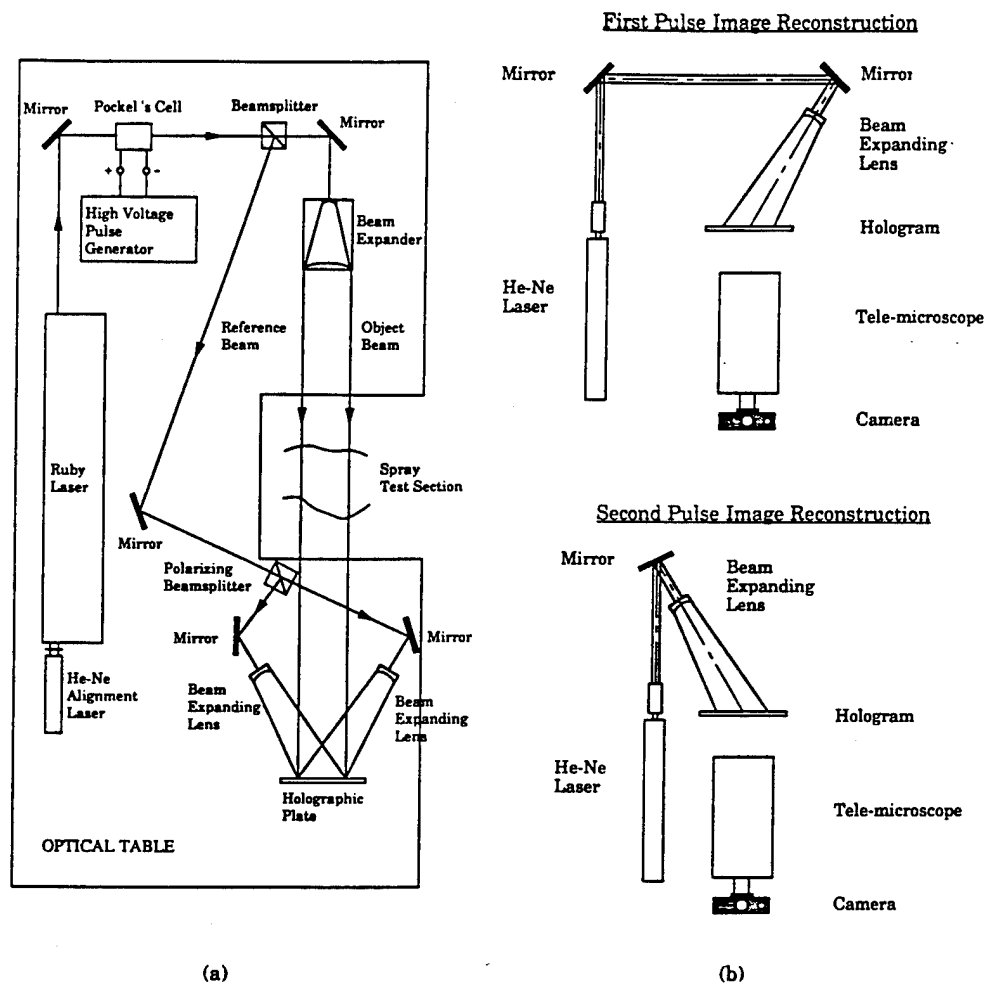


Fig. 3 Schematic of the optical setup for double-pulse holograms with two reference beams: (a) recording systems; (b) reconstruction system.

components of the incident light while permitting the horizontal components to pass undeviated. Therefore, the reference beam of the first pulse, whose polarization direction is changed to horizontal by the Pockels cell, passes through the beam splitter without any change of direction, while the reference beam of the second pulse is reflected in the direction diagonal to the beam splitter. In this manner, two reference waves that have different incident angles interfere with the object wave. This produces two separate holograms, each corresponding to a laser pulse. Each reference wave is diverged by a plano-concave lens to cover the entire holographic plate. Neutral-density filters are used to control the reference-to-object-beam ratio as well as the total irradiance at the holographic plate to improve the quality of the holograms. The entire setup is placed on a vibration-isolation optical table.

To find the magnification factor and locate the droplet position, one more hologram of a grid object was taken just after fabricating the spray hologram, without any changes

in the optical system. The grid, with numbered horizontal and vertical lines at 5.0-mm intervals, was drawn by a computer, copied onto transparent paper, and attached to a transparent glass plate.

### Hologram Reconstruction and Image Processing System

The holograms were reconstructed using a 10-mW He-Ne laser as shown in Fig. 3b. The reference wave is expanded up to 20 mm diameter by a beam expander and converted to a spherical diverging wave by a plano-concave lens, the same as at recording. The reconstructed virtual image of the droplet is magnified by a Questar telescope macrolens system (long-distance microscope). A camera that is attached to the end of this system can record the magnified microscopic images of the liquid droplets. Seven different locations around the liquid sheet were monitored for both pulses. The observation area at each location is approximately 2.0 cm  $\times$  2.0 cm. At each location, the droplet images and the grid are photographed. The droplet images can be magnified fourfold in the final photographic print (7.5 cm  $\times$  11.0 cm).

The photographed images were recorded by a CCD camera and inputted to a personal computer for image analysis. Noise or speckle effects did not present a problem. IMAGE ANALYST, provided by Automatrix, Inc., was used as the image processing software. The values of the magnification factor at each location ranged from 40.0  $\mu\text{m}$  to 45.0  $\mu\text{m}$  per 1 pixel of the monitor. The diameters of droplets were obtained by measuring the total area of droplets and calculating the equivalent diameter corresponding to the total area. The droplets were on the same plane as the liquid sheet, and they were simultaneously in focus. To measure the horizontal and vertical velocities of droplets, the absolute coordinates of the centroid of the droplets from the origin of the grid for both pulses were measured. Next, the difference in the coordinates of the centroid in each direction between two pulses was divided by the pulse separation time. To verify the accuracy of the diameter measurements, the holograms of a 4.76-mm precision steel ball and a 307- $\mu\text{m}$ -diameter steel wire were fabricated and the diameters of the steel ball and the wire were measured from the holograms. The measurement error was less than 4% in both cases. The average error for the velocity measurements was estimated to be approximately 10%.

## RESULTS

The shapes of the liquid sheet (obtained with strobe photography) at three different impingement angles are compared with the theoretically predicted shapes in Figs. 4–6. The dotted shapes (corresponding to the outline of the photographed liquid sheet) match rather well with the theoretical predictions of Ibrahim and Przekwas [5] for all impingement angles examined. The only noticeable difference appears at  $\phi = 180^\circ$ . A “V” shape is observed in the theoretical prediction above the impingement point (denoted with a dark circle) as the impingement angle increases (Figs. 5 and 6). No such shape was visually observed in the experiments (note that the physical presence of the glass tubes prohibits the photographic recording of the liquid sheet in the neighborhood of  $\phi = 180^\circ$ ). As expected, the maximum width of the liquid sheet increases with increasing impingement angle. However, the maximum length of the liquid sheet is considerably less sensitive to the value of the impingement angle in the range from  $2\theta = 90^\circ$  to  $2\theta = 120^\circ$ . The streaklines due to

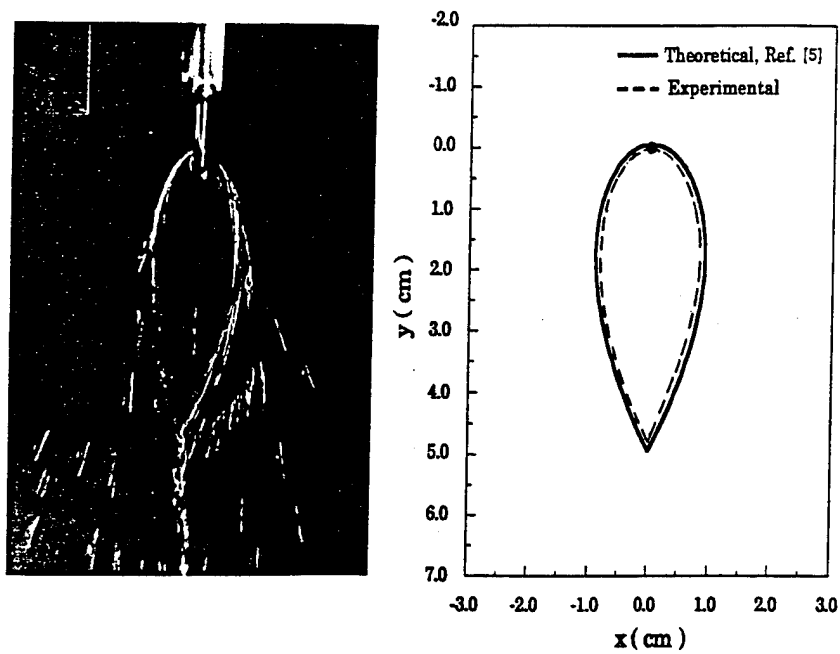


Fig. 4 Comparison of the photographed shape of the liquid sheet with the theoretically predicted shape for  $D_j = 1.5 \text{ mm}$ ,  $V_j = 2.49 \text{ m/s}$ ,  $2\theta = 60^\circ$ .

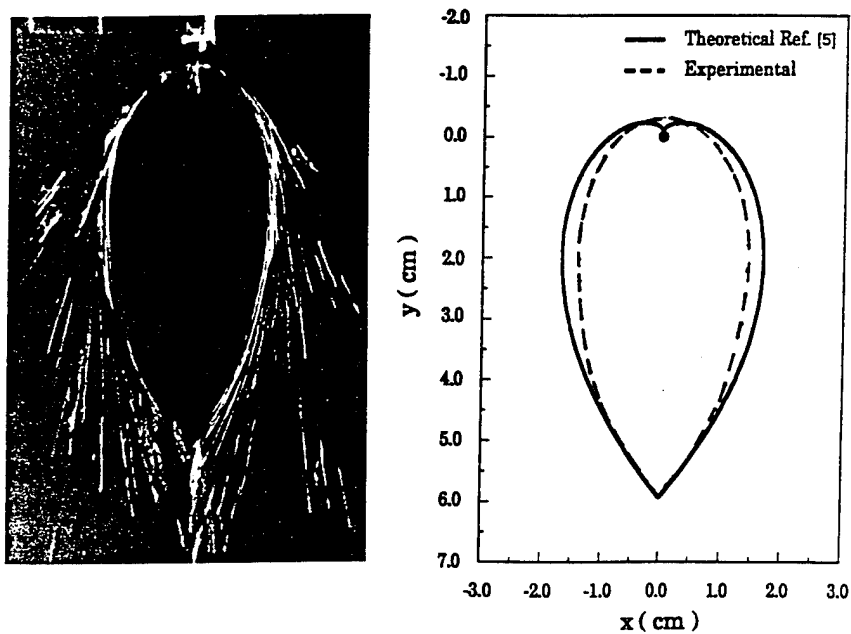


Fig. 5 Comparison of the photographed shape of the liquid sheet with the theoretically predicted shape for  $D_j = 1.5 \text{ mm}$ ,  $V_j = 2.49 \text{ m/s}$ ,  $2\theta = 90^\circ$ .

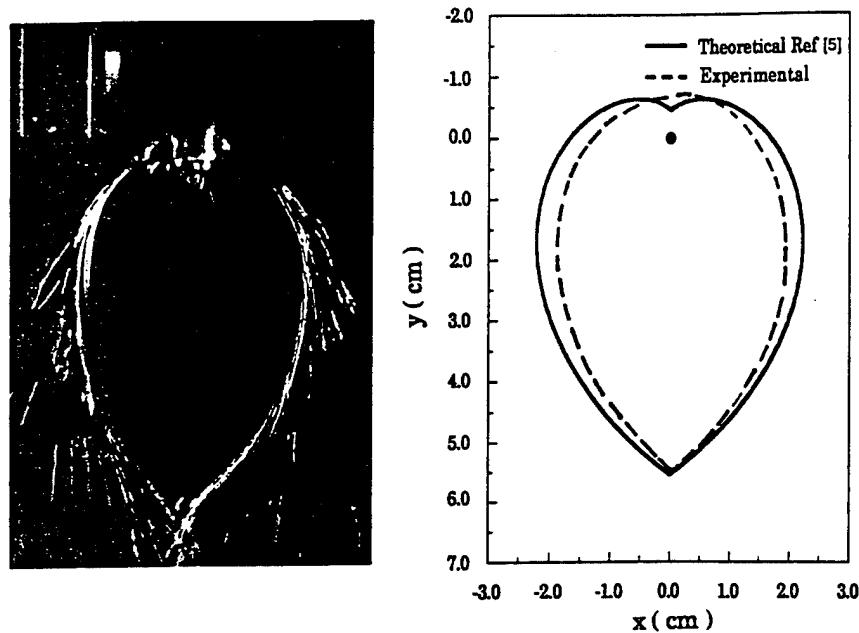


Fig. 6 Comparison of the photographed shape of the liquid sheet with the theoretically predicted shape for  $D_j = 1.5$  mm,  $V_j = 2.49$  m/s,  $2\theta = 120^\circ$ .

the movement of droplets indicate that the droplets are shedding from the edge of the liquid sheet in the tangential direction along the edge, instead of moving in the radial direction. This fact is also verified by the measurement of droplet velocities, which will be described later.

The quantitative comparison of the maximum width and the maximum length of the liquid sheet between experimental measurements and theoretical predictions is shown in Fig. 7. The theoretically predicted values of the maximum width [5] in Fig. 7a at low jet impingement velocities match very well with the measured values. However, the theory overestimates the maximum width of the liquid sheet as the jet velocity is increased up to  $V_j = 2.5$  m/s. The disagreement becomes greater at higher velocities, around  $V_j = 3.0$  m/s, especially for  $2\theta = 90^\circ$ . The experiments agree with the predicted trend that the dependence of the maximum width of the sheet on the jet impingement velocity is stronger for high impingement angles. The predicted maximum length of the liquid sheet agrees reasonably with the measured values, even though the theory underestimates at low jet velocities and overestimates at high jet velocities of the experiments (Fig. 7b). The theory predicts practically no difference in the maximum length between  $2\theta = 90^\circ$  and  $2\theta = 120^\circ$ . The experiments support this trend, which implies that after a certain impingement angle the shape of the liquid sheet keeps widening while its length remains practically constant.

Figure 8 shows typical photographs of microscopic views of a hologram illustrating the droplet formation process. Figure 8a is a view of a portion of the side of the sheet, while Fig. 8b is nearly under the bottom (tip) of the sheet ( $\phi = 0^\circ$ ). Two facts are clear: First, there is a great variation in droplet size; and second, the majority of the droplets feature nonspherical shapes, in particular in the region underneath the sheet (Fig. 8b). Using the

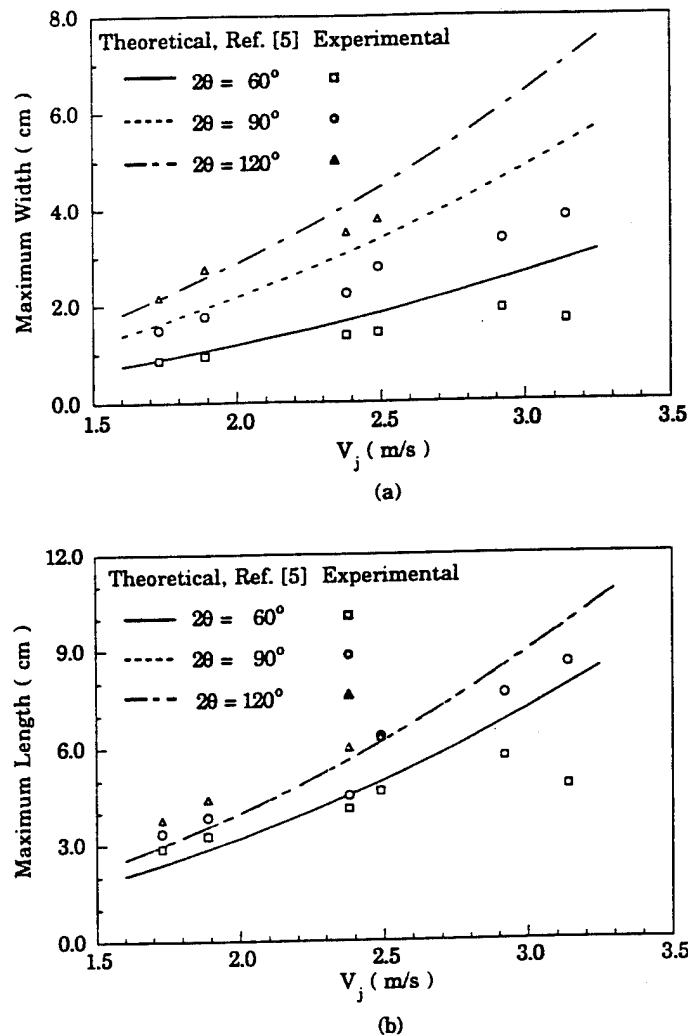


Fig. 7 Comparison of the measured maximum width and length of the liquid sheet with theoretically predicted values for  $D_j = 1.5$  mm,  $V_j = 2.49$  m/s: (a) maximum width; (b) maximum length.

IMAGE ANALYST software, an average roundness factor from all the droplets measured was defined. The value of this factor was 0.81 (a value equal to unity corresponds to a perfect sphere). Further breakup of the nonspherical droplets downstream is unlikely.

The droplet size measurements are compared in Fig. 9 to the theoretical predictions of Dombrowski and Johns [1] (with the expression for  $K$  from Hasson and Peck [2] and Ibrahim and Przekwas [5]) as well as Clark and Dombrowski [4] (with the expression for  $K$  from Hasson and Peck [2]). Note that all the droplets observed were sized and are included in Fig. 9. For all impingement angles (Figs. 9a–9c), no droplets were observed in the upper region of the liquid sheet ( $\phi > \pm 90^\circ$ ), due to the shedding mechanism of droplets

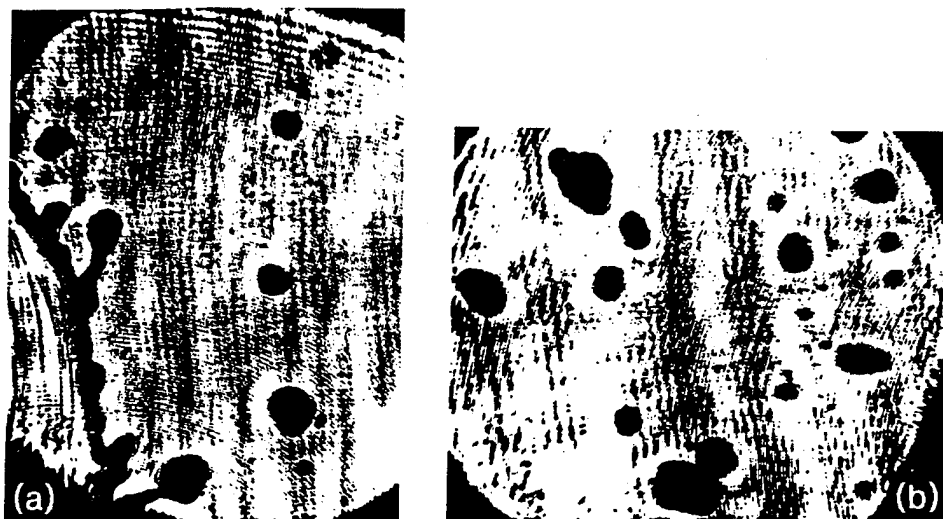


Fig. 8 Typical photographs of a hologram revealing droplet images at two different locations for  $D_j = 1.5$  mm,  $V_j = 2.49$  m/s,  $2\theta = 120^\circ$ : (a) upper right region of the sheet ( $x = 1.6$  to  $3.3$  cm,  $y = -0.5$  to  $2.0$  cm); (b) lower left region ( $x = -2.5$  to  $-1.0$  cm,  $y = 4.0$  to  $5.7$  cm).

in the tangential direction as explained in the discussion relevant to Figs. 4–6. On the other hand, the theories in [1] and [4] predicted the existence of droplets all around the liquid sheet because they relied on the assumption that droplets are disintegrating at all locations around the edge of the liquid sheet moving in the radial direction. Utilizing two different expressions for the thickness of the liquid sheet (Hasson and Peck's [2] and Ibrahim and Przekwas' [5]) did not markedly affect the predicted droplet size distribution using Dombrowski and Johns' analysis [1]. Clark and Dombrowski's correlation [4] predicted droplet sizes larger than those in [1]. This is because Clark and Dombrowski's analysis [4] focused on droplets disintegrating from the rim of an oval liquid sheet, which are usually coarser than those disintegrating from the leading edge of a semiinfinite liquid sheet [1].

In general, the predicted size distribution falls within the range of the measured values. However, the theories fail to account for the wide distribution of droplet sizes, ranging from  $500\ \mu\text{m}$  up to  $3,000\ \mu\text{m}$ . This discrepancy comes from the assumption of Dombrowski and Johns [1] that only one size of droplets is created from the unstable liquid ligaments. This assumption was adopted by all subsequent studies of the process [2–5]. It is recommended that future modeling efforts describe the disintegration of unstable liquid ligaments in a manner that allows for the generation of multiple sizes of droplets. Note that we do not report average droplet diameters. However, the coexistence of small and large droplets at the same angular position is obvious in the holograms. Existing theories do not allow for this fact. We believe that improvement is needed in this respect. The coexistence of small and large droplets around small values of  $\phi$  (tip of the liquid sheet) can be physically explained by the likelihood of the presence and partial disintegration of large liquid ligaments in this region. On the other hand, droplets existing at side regions of the liquid sheet (away from the tip) are perhaps more likely to be torn off directly from the edge of the sheet so that their diameters are comparable to the sheet thickness.

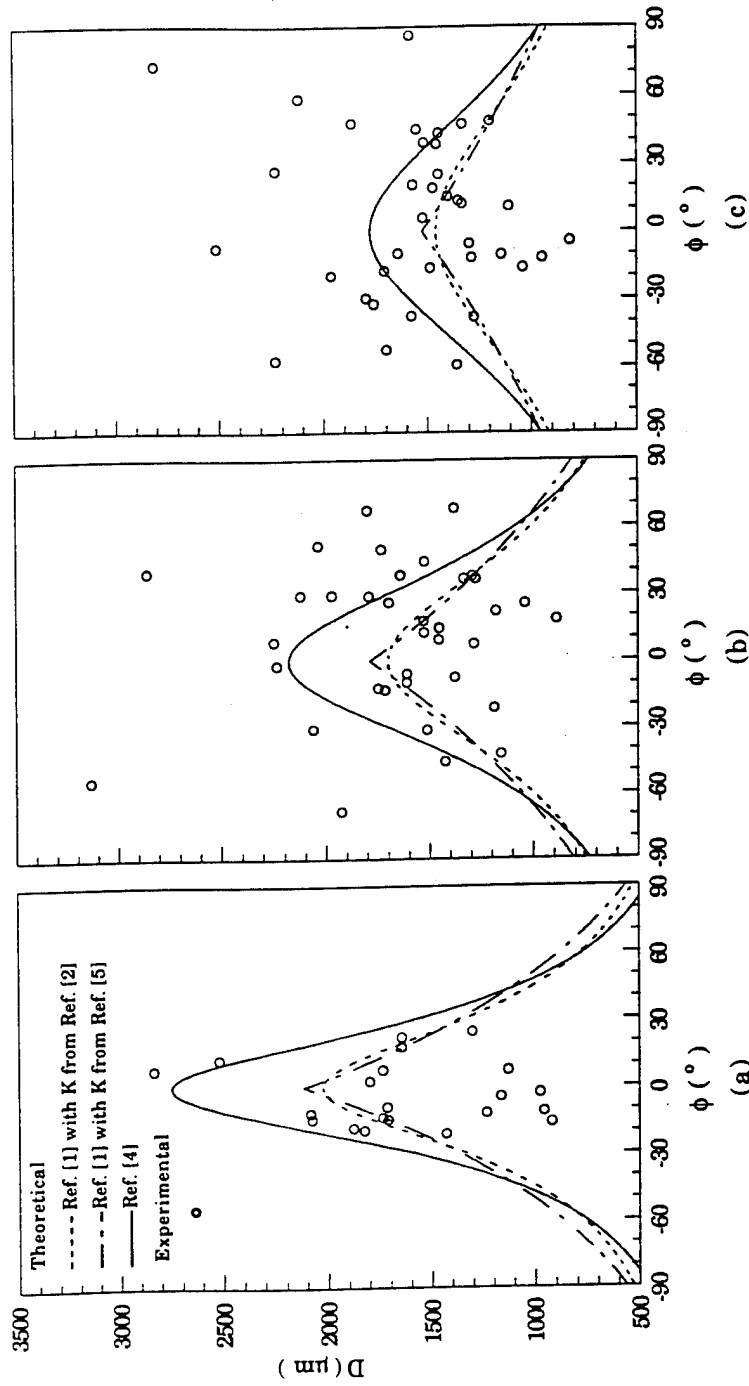


Fig. 9 Measured droplet size distribution and comparison with theoretical predictions for  $D_j = 1.5$  mm,  $V_j = 2.5$  m/s: (a)  $2\theta = 60^\circ$ ; (b)  $2\theta = 90^\circ$ ; (c)  $2\theta = 120^\circ$ .

Cumulative droplet size distributions are compared with the Rosin-Rammler distribution function [9] in Fig. 10. The Rosin-Rammler distribution function is expressed in the form

$$1 - Q = \exp\left(-\frac{d_p}{X}\right)^q \quad (13)$$

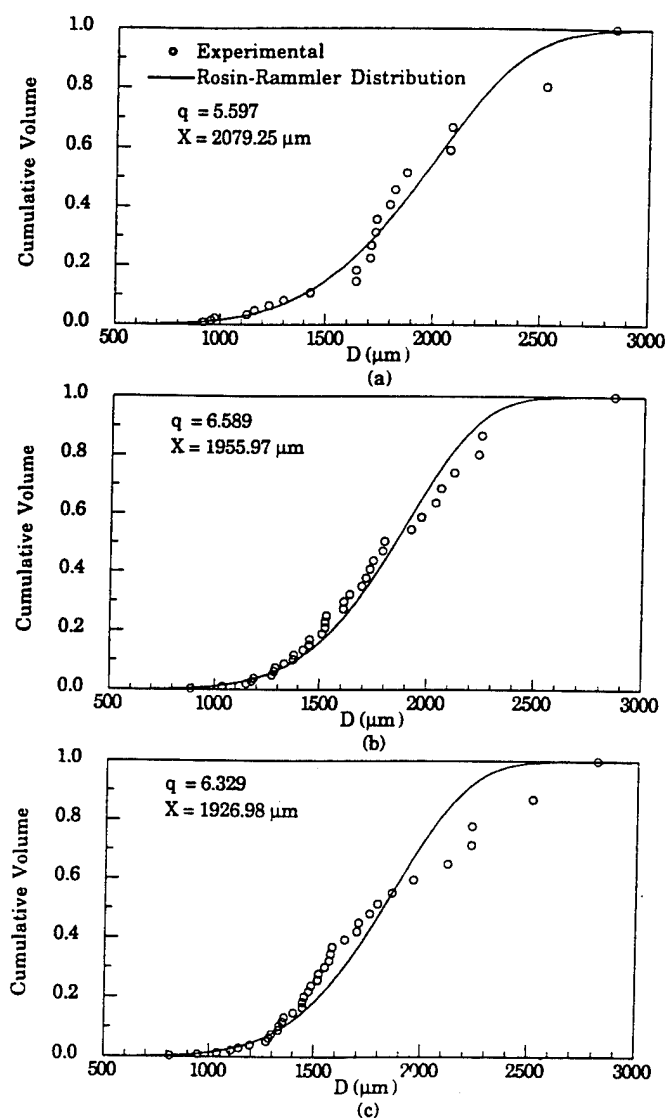


Fig. 10 Cumulative droplet size distribution and comparison with Rosin-Rammler distribution for  $D_j = 1.5$  mm,  $V_j = 2.5$  m/s: (a)  $\theta = 60^\circ$ ; (b)  $\theta = 90^\circ$ ; (c)  $\theta = 120^\circ$ .

where  $Q$  is the fraction of the total volume contained in drops of diameter less than  $d_D$ ,  $q$  is a size distribution parameter, and  $X$  is a characteristic diameter such that 63.2% of the total liquid volume is in drops of smaller diameter. The Rosin-Rammler distribution generally fits well with the measurements for all three cases (Fig. 10). The higher value of  $q$  for  $2\theta = 90^\circ$  and  $2\theta = 120^\circ$  indicates that the range of drop sizes is smaller compared to  $2\theta = 60^\circ$ .

Figures 11a and 11b show the horizontal and vertical velocity components of the droplets for two characteristic impingement angles. The horizontal velocities clearly show that droplet shedding occurs tangentially along the edge and not radially. This fact, combined with the cardioid shape of the sheet (Figs. 4–6), is responsible for the presence of negative horizontal velocities in the right half of the sheet in the vicinity of  $\phi = 0^\circ$  and positive horizontal velocities in the left half of the sheet in the same vicinity. The vertical velocity components of the droplets show good symmetry with respect to  $\phi = 0^\circ$ , with the maximum occurring at  $\phi = 0^\circ$ . The droplets in the vicinity of  $\phi = 0^\circ$  move straight downward.

### CONCLUSIONS

In this article an experimental study was presented for the problem of disintegration of a liquid sheet created by two impinging jets. The experiments were conducted utilizing

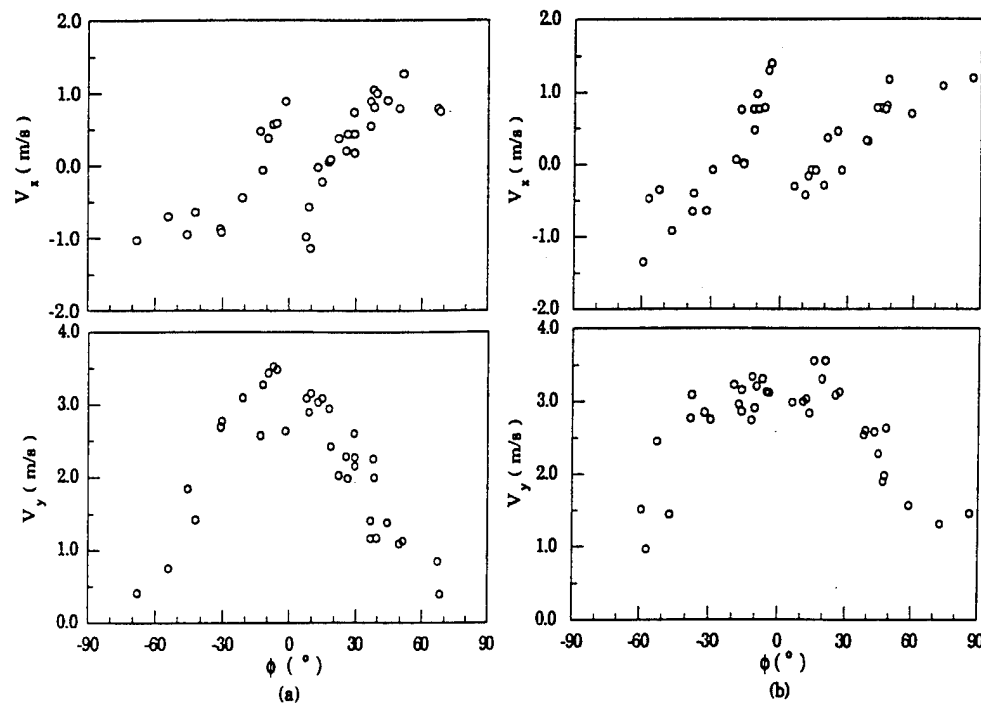


Fig. 11 Measured velocity components of the liquid droplets for  $D_j = 1.5$  mm,  $V_j = 2.5$  m/s: (a)  $2\theta = 90^\circ$ ; (b)  $2\theta = 120^\circ$ .

pulse holography. In addition to performing accurate measurements on the size and verocity of the liquid droplets generated in this process, the study tested existing theoretical predictions [1, 4, 5] on the size and shape of the liquid sheet as well as on the size distribution of the droplets around the sheet periphery. For most part, the predicted shape agreed rather well with the experimental observations, qualitatively as well as quantitatively. As the impingement velocity increased, the agreement on the maximum sheet thickness deteriorated. Both the theory and the experiments showed an insensitivity of the maximum sheet length on the jet impingement angle for large values of this angle. Even though the theoretical predictions for the droplet size distribution around the sheet rim provided a reasonable order-of-magnitude estimate of droplet sizes, they were limited by the fact that they relied on the assumption that at each angular location the droplets are spherical and monodispersed. The experiments clearly indicated that the liquid elements are largely nonspherical and that they exhibit large size variations in the neighborhood of the same location. It is recommended that future improved theoretical models of the atomization process remedy this deficiency. Maximum vertical velocity components were measured in the vicinity of the tip (bottom) of the cardioid sheet. In the same vicinity the horizontal velocity components were negative, a fact that is a direct result of the cardioid shape of the sheet.

## REFERENCES

1. N. Dombrowski and W. R. Johns. The Aerodynamic Instability and Disintegration of Viscous Liquid Sheets. *Chem. Eng. Sci.*, vol. 18, pp. 203-214, 1963.
2. D. Hasson and R. E. Peck. Thickness Distribution in a Sheet Formed by Impinging Jets, *AIChE J.*, vol. 10, pp 752-754, 1964.
3. H. S. Couto, D. Bastos-Netto, and C. E. Migueis, Modeling of the Initial Droplet Size Distribution Function in the Spray Formed by Impinging Jets. *J. Propulsion*, vol. 8, pp. 725-728, 1992.
4. C. J. Clark and N. Dombrowski. On the Formation of Drops from the Rims of Fan Spray Sheets. *Aerosol Sci.*, vol. 3, pp. 173-183, 1972.
5. E. A. Ibrahim and A. J. Przekwas. Impinging Jets Atomization. *Phys. Fluids A*, vol. 3, pp. 2981-2987, 1991.
6. J. D. Naber and R. D. Reitz. Modeling Engine Spray/Wall Impingement, SAE Paper 880107, 1988.
7. G. I. Taylor. Formation of Thin Flat Sheets of Water. *Proc. R. Soc. Lond. A*, vol. 259, pp. 1-17, 1960.
8. W. E. Anderson, H. M. Ryan, S. Pal, and R. J. Santoro. Fundamental Studies of Impinging Liquid Jets. AIAA Paper 92-0458, 30th Aerospace Sciences Meeting, Reno, NE, 1992.
9. A. H. Lefebvre. *Atomization and Sprays*. Hemisphere, New York, NY, 1989.

## **APPENDIX B**

## **HOLOGRAPHY EXPERIMENTS IN A DENSE HIGH SPEED IMPINGING JET SPRAY**

by

B.S. Kang\*, D. Poulikakos\*\*

Department of Mechanical Engineering  
University of Illinois at Chicago  
842 West Taylor Street  
Chicago, IL 60607-7022

### **Abstract**

In this paper an experimental study of the fluid dynamics of a spray created by two high speed impinging jets is presented. Utilizing a novel two-reference-beam double-pulse holographic technique the effect of the impingement angle, liquid jet velocity, orifice diameter, and liquid properties on the atomization process was investigated. Visualization of the overall spray pattern as well as measurements of the size and velocity of the droplets were performed.

The overall spray pattern clearly revealed the inherent wave nature in the disintegration process of this type of atomization. Smaller droplets were generated more rapidly, in a shorter distance from the impingement point, with larger impingement angles, higher jet velocities, and smaller orifice diameters. Surface tension played an important role in the droplet size without any noticeable effect on the spray pattern, whereas viscosity affected the structure without any significant effect on the droplet size. The droplet velocities were not affected markedly by the liquid properties. The superiority of the universal root-normal distribution to the Rosin-Rammler distribution was proved in the great majority of cases tested.

\* Graduate Research Assistant

\*\* Professor

## Nomenclature

$D$	diameter
$D_j$	orifice diameter (Figure 1)
$D_{MMD}$	mass median diameter
$D_{10}$	length-mean diameter
$D_{32}$	Sauter-mean diameter
$r$	radial distance from the impinging point (Figure 1)
$R$	liquid jet radius
$Re_j$	Reynolds number of liquid jet
$V$	velocity
$V_j$	velocity of liquid jet
$V_m$	magnitude of velocity vector of droplet
$We_j$	Weber number of liquid jet
$x$	horizontal coordinate from impinging point (Figure 1)
$y$	vertical coordinate from impinging point (Figure 1)
$\mu$	viscosity of liquid
$\theta$	half of the axis-to-axis angle of the impinging jets
$\rho$	density of air
$\rho_l$	density of liquid
$\sigma$	surface tension of liquid

## 1. Introduction

Impinging-jet injectors are commonly used in liquid propellant rocket engines [1,2]. The liquid propellants (the fuel and oxidizer) are injected through a number of separate small holes in such a manner that they impinge upon each other. Combustion instabilities in rocket engines are characterized by sustained pressure oscillations. The origin of the instabilities appears to be related to the atomization and mixing processes of the propellants. Photographs of the spray formed by

two impinging jets show the periodic nature of the atomization process [3, 4]. Groups of droplets resulting from the break-up of liquid ligaments give the impression of waves originating from the impingement point. The mechanisms that initiate and sustain these phenomena have not been disclosed satisfactorily.

As shown schematically in Fig. 1, two impinging high speed jets form a small fan-shaped liquid sheet around the impingement point. This liquid sheet quickly disintegrates into unstable arc-shaped liquid ligaments that contract themselves by surface tension and finally break into droplets. The spray characteristics depend on the liquid jet velocity  $V_j$ , the orifice diameter  $D_j$ , the impingement angle  $2\theta$ , the conditions of the surroundings, and the physical properties of the liquid.

Studies on the spray characteristics of impinging-jet injectors started in the 1950s and 1960s and were focused on revealing the sheet breakup mechanisms and predicting the size distribution of droplets. Heidmann et al. [4] investigated the effects of orifice diameter, jet velocity, impingement angle, pre-impingement length, and liquid properties (viscosity, surface tension) on the structure of the spray. The spatial characteristics of water sprays were investigated by Foster and Heidmann [5,6]. Dombrowski and Hooper [7] studied the mechanism of the disintegration of liquid sheets formed by two impinging laminar and turbulent jets. They contributed the mechanism to the formation of unstable waves of aerodynamic or hydrodynamic origin. Huang [8] investigated the breakup mechanism of axisymmetric liquid sheets formed by the impingement of two co-axial water jets. He reported three breakup regimes depending on the Weber number of the liquid jet. Recent research conducted by Anderson et al. [9] focused on the characteristics of the spray created by two turbulent impinging jets. The mean drop diameters decreased with an increase in the jet velocity and impingement angle. The mean drop velocities were almost equal to the jet velocity regardless of the impingement angle and measured position. Ryan et al. [11] extended Anderson et al.'s work [9] to investigate the effects of the jet conditions (laminar vs. turbulent), orifice diameter, impingement angle, and jet velocity on the atomization of impinging liquid jets. The experimental results contrasting the laminar and turbulent jet conditions

demonstrated that the jet conditions had a significant effect on the atomization process. They also modeled the disintegration of sheets formed by two impinging liquid jets using two existing theories; a stationary antisymmetric wave-based theory for low Weber numbers [12], and a linear stability-based theory for high Weber numbers [9]. Vassallo et al. [13] investigated the spray characteristics of two and four impinging-jet injectors using Phase Doppler Particle Analysis (PDPA).

This study reports the main results of an experimental investigation, based on two-reference double-pulse holography, for the visualization of the spray structure as well as the measurement on the size and velocity of the liquid droplets. The study focuses on the dense spray region where liquid elements are rather large and non-spherical. The experiments involved two non-evaporating impinging jets injected into still air at atmospheric pressure. The effect of several factors on the spray characteristics was examined using water, ethanol, and three glycerol solutions as test liquids. Theoretical predictions on the mean droplet size were also attempted and tested against the experimental results. The frequently used droplet size distributions were compared with the experimental results to validate their application to experimental data.

## **2. Experiments**

### **2.1 Impinging Jet Apparatus**

The experimental apparatus for two impinging jets (not shown for brevity) is described in detail in [14]. Herein, only a brief description is contained: High-pressure  $N_2$  gas was used for pressurizing a liquid reservoir. The liquid flow from a flowmeter passed through an on-off valve and was divided into two identical branches for the individual liquid jets. Precision-bore glass tubes were used as impinging jet injectors. The inner diameters of the tubes in this study were 1.016 and 1.534 mm. The length of the tubes was 0.152 m. A 50.8-mm-long, 6.35-mm-O.D. copper tube bonded at one end of each glass tube was connected to the liquid supplying plastic tube. The entry to the glass tube was smoothly contoured to maintain laminar flow conditions at the injector exit. The laminar flow condition up to the Reynolds number about 10,000 was

indicated by visual observations such as no ruffling of liquid jet boundaries and clear glassy appearance of the jets. Each injector was mounted on a high precision rotation stage in a manner which allowed for fine tuning until a "perfect" liquid sheet normal to the liquid jet plane was obtained [14]. The impingement angle was adjusted accurately by the rotation stages. The falling liquid was collected into a cylindrical liquid tank.

## *2.2 Optical System for Hologram Recording*

A novel technique was used for the recording of the holograms used for the velocity measurements. This technique allows for the separate reconstruction of the spray image obtained by different pulses of the light source, an advantage that greatly facilitates the image processing of the holograms, particularly in the dense spray region. Figure 2 shows the schematic layout of the holographic recording system. The light source is a ruby laser which can generate a 694-nm-wavelength, vertically polarized, 1-J output energy, either single-or double-pulse laser beam. The pulse interval was 50  $\mu$ s (after a trial and error process). The short pulse duration (30 ns) assures the freezing of all moving liquid elements or droplets and the clarity of the resulting images. For the alignment of all optical components before firing the ruby laser, a He-Ne alignment laser which is mounted on the ruby laser box was used.

A Pockels Cell was used to change the polarization direction of the first pulse. To drive the Pockels Cell, a high-voltage pulse generator was employed. The input signal to this device comes from a synchronization socket in the ruby laser control box. To change the polarization direction of the first pulse only, the Pockels Cell was activated just before the first pulse throughout the duration of the first pulse. To this end, the high-voltage pulse generator provides an adjustable input/output delay and pulse width, from 0.2 ms to 1.2 ms and from 40 ns to 1.2 ms, respectively. The output pulse amplitude ranges from 2.0 kV to 7.5 kV.

A beamsplitter divided the incoming laser beam into an object beam and a reference beam. The object beam was expanded and collimated by a Galilean-type beam expander. The diameter of the object beam was increased up to 0.1 m to cover entirely the spray region of interest. This

plane wave passed through the spray region and finally was intercepted at the  $0.10\text{-m} \times 0.13\text{-m}$  holographic glass plate.

The reference beam passed through a cube-type polarization beamsplitter. This beamsplitter reflected the vertical components of polarization in the incident light while permitting the horizontal components to pass undeviated. Therefore, the reference beam of the first pulse, whose polarization direction was changed horizontally by the Pockels Cell, passed through the beamsplitter without any change of direction. The reference beam of the second pulse was reflected at the diagonal plane in the beamsplitter. In this manner, two reference beams which had different incident angles interfered with the object wave. This produced two separate holograms each corresponding to a laser pulse. Each reference wave was diverged by a plano-concave lens to cover the entire holographic plate. Neutral density filters were used to control the reference-to-object-beam ratio as well as the total irradiance at the holographic plate to improve the quality of the holograms. The entire setup was placed on a vibration-isolation optical table.

To find the magnification factor and locate the droplet position, one more hologram of the grid object was taken after fabricating a spray hologram, without any changes in the optical system. The grid with numbered horizontal and vertical lines at 5.0 mm intervals was drawn by a computer, copied onto a transparent paper and attached to a transparent glass plate.

### *2.3 Hologram Reconstruction and Image Processing System*

The holograms were reconstructed using a 10-mW He-Ne laser. The reconstructed virtual image of the spray was magnified by a Questar telescope macro lens system. A camera, attached to the end of this system, recorded the magnified microscopic images of the liquid droplets. Six different locations were identified and studied for both pulses, i.e., three locations in the horizontal direction with  $\Delta x = \pm 25$  mm from the spray axis, at two locations ( $\Delta y = 25\text{mm}$ ) on the spray axis. The sampling area at each location was approximately  $(\Delta x, \Delta y) = (10 \times 15 \text{ mm})$ . At one location, the droplet images and the grid were photographed. The droplet images were magnified seven times in the final photographic print ( $75 \text{ mm} \times 110 \text{ mm}$ ). *The results on the droplet*

*diameters and velocities presented in this paper were obtained after averaging the measurements in the above six locations (unless otherwise noted).*

The images of droplets and grids printed on the photographic papers were captured by a CCD camera and inputted into a personal computer for the image analysis. Image Analyst provided by Automatrix Inc. was used as the image processing software. The magnification factor between the length of the image on the monitor and the actual length of the image was calculated by measuring the length of one grid the real distance of which is 5.0 mm. The value of the conversion factor in this study ranges from 24.3 to 27.9  $\mu\text{m}$  per one pixel of the monitor. The diameters of droplets were obtained by measuring the total area of droplets and calculating the equivalent diameter of a circle corresponding to the total area.

To measure the horizontal and vertical velocities of droplets, the absolute coordinates of the centroid of the droplets from the origin of the grid for both pulses were measured. Next, the difference in the coordinates of the centroid in each direction between two pulses was divided by the pulse separation time. To verify the accuracy of the diameter measurements, the holograms of a 4.763-mm precision steel ball and a 306.6- $\mu\text{m}$  steel wire were fabricated. The diameters of the steel ball and the wire were measured in the same manner as described for the measurements of the liquid droplet diameters. The relative error between the ball size and the holographic measurement of the diameter was within 5%. The approximate error involved in the velocity measurements of droplets was estimated in the following manner. Assuming a maximum of 4 pixels of error (this value is arbitrary but reasonable for the maximum value based on experience) in the distance measurements, the corresponding error in distance is 111.6  $\mu\text{m}$  using the maximum conversion ratio (27.9  $\mu\text{m}/\text{pixel}$ ). The error in velocity for this distance is 2.2 m/s with 50  $\mu\text{s}$  pulse separation time. This value is within 20% of measured velocities of droplets for  $V_j = 12.0$  m/s.

The total number of droplets measured for each test condition ranged between 500 and 1000. This is relatively small sample size compared to the recommended value (5500) [15]. However, this is inevitable because the measurements were made from the instantaneous spray images (for 30 ns) rather than collecting a large amount of data over a time period (for example, a

couple of seconds as customarily done with other laser instruments). Processing of the data is very tedious because the data-analysis procedure for the droplet size and velocity measurements is not currently automated.

#### 2.4 Test Conditions and Physical Properties of Liquid

The test conditions are summarized in Table 1. The Reynolds and Weber numbers of the liquid jet are based on the orifice diameter, liquid properties, and horizontal component of the liquid jet velocity ( $V_j \sin \theta$ ). The reason for electing to use the horizontal component of the jet velocity instead of the jet velocity in itself is twofold: First, the horizontal momentum of each liquid jet is closely related to the liquid sheet spreading and atomization. Second, this choice allows for the effect of the impingement angle to be reflected in the definition of  $Re_j$  and  $We_j$  when the jet velocity is kept constant.

The effect of the impingement angle, liquid jet velocity, and orifice diameter was examined in the series H of experiments with water. The condition for experiment H1 ( $D_j = 1.016$  mm,  $\theta = 90^\circ$ , and  $V_j = 12.0$  m/s) is considered as the baseline condition. Three experiments with the baseline condition were performed to verify the repeatability of the experimental results. The effect of liquid properties on the spray characteristics was investigated with ethanol (E series) and three glycerol solutions (G series). The mixing percentage of glycerol solutions is by mass throughout this study. The physical properties of the liquids used in the experiments at  $20^\circ\text{C}$  and  $1$  atm are shown in Table 2. The values in a parenthesis represent the ratio of the properties of ethanol and glycerol to the properties of water.

### 3. Results

#### 3.1 Overall Spray Pattern

Visual observations indicated that the generated sprays with the liquid jet velocities up to  $12$  m/s were primarily two-dimensional (fan spray). However, they became three-dimensional (cone spray) when the liquid jet velocities exceeded  $15$  m/s. Due to space limitations, no photographs of

the overall spray pattern are shown herein. A considerable amount of additional information can be found in [16]. Instead, a description of the phenomena observed will be presented. Generally, a small fan shaped liquid sheet formed near the impingement point due to the obliquely colliding high speed jets. Circumferentially aligned liquid ligaments, detached directly from this liquid sheet. These ligaments progressively broke up into droplets as they moved downstream. The expanding angle of the liquid sheet and arc-shaped liquid ligaments greatly increased with an increase in the impingement angle. At the lowest impingement angle,  $2\theta = 60^\circ$ , the size of droplets was noticeably larger than that for the higher impingement angles. This is due to the fact that the size of liquid ligaments, which break up into droplets, is larger at this condition. Increasing the impingement velocity did not substantially altered the overall spray pattern. However, smaller droplets were produced with an increase of the liquid jet velocity, as will be shown quantitatively in the next section. The shape and size of the liquid sheet were also very irregular and smaller for higher velocities compared to low jet velocities. An increase of the orifice diameter from  $D_j = 1.016$  mm to  $D_j = 1.534$  mm with  $V_j = 12.0$  m/s,  $2\theta = 90^\circ$  generated an entirely different spray pattern. The liquid sheet around the impingement point become larger and large liquid ligaments existed in the far downstream region of the spray.

The effect of liquid properties on the overall spray pattern was studied for  $D_j = 1.016$  mm,  $2\theta = 90^\circ$ . The viscosity of ethanol does not change much compared to that of water. However, the surface tension of ethanol is 30% that of water. In general, the surface tension of liquid represents the resisting force for the formation of the new surface area. This implies that liquid with lower surface tension is easier to disintegrate. No pronounced effect of surface tension on the overall spray pattern was observed. This fact is also confirmed by Heidmann et al. [4] using Varsol, the surface tension of which was reduced to about one half that of water. However, the effect of surface tension is more evident in the droplet size (the mean droplet diameters of the ethanol spray were found to be much smaller than those of the water spray as will be discussed in the next section).

The viscosity of liquid plays an important role in many aspects of atomization. An increase in viscosity lowers the Reynolds number and also prevents the progress of any natural instabilities. These instabilities in the jets and sheets are the main impetus for the atomization of liquid. Therefore, the combined effect of an increase in viscosity is to delay disintegration and increase the size of droplets in the spray. Experiments with glycerol solution (Table 2) featured arc-shaped liquid ligaments detaching earlier from the liquid sheet near the impingement point and stretching out further downstream in the spray. This is attributed to the delay of the break-up of ligaments due to the high viscosity of glycerol.

### 3.2 Droplet Size Measurements

Figure 3 shows typical photographs of droplet images at the first and second pulses, which are used for the measurements of droplet size and velocity. The droplet diameters were obtained by measuring the total area of each droplet and calculating the equivalent diameter of a circle corresponding to that area. This figure demonstrates the ability of the double-pulse holographic technique to record the size and position of liquid elements at two different times. The region shown is downstream along the spray axis. The movement of droplets can be clearly seen and the identification of the same droplets between the two photographs is not difficult. For example, the droplet identified as No. 1 in Fig. 3 (a) corresponding to the first pulse moved to the location identified as No. 1 in Fig. 3 (b) corresponding to the second pulse. The benefit from the separation of the first and second droplet images is remarkable. In conventional double-pulse holography, the droplet images in Fig. 3 (b) would overlap with the images in Fig. 3 (a). This photograph also demonstrates the size diversity of the liquid elements as well as the fact that these elements are largely non-spherical.

To check the repeatability of the experimental results, preliminary experiments were conducted. Three experiments with the baseline condition ( $D_j = 1.016$  mm,  $2\theta = 90^\circ$ ,  $V_j = 12.0$  m/s) were performed for this purpose. The maximum changes in mean droplet diameters with respect to the averaged mean diameters for three runs are within 6% for  $D_{10}$  and 15% for  $D_{32}$ .

Here,  $D_{10}$  and  $D_{32}$  are length- and Sauter-mean diameters. Based on above results, it is confirmed that the measurement results for mean droplet diameters are within allowable repeatability.

The effect of the impingement angle, liquid jet velocity, and orifice diameter on the droplet diameter is shown in Fig. 4.  $D_{MMD}$  (mass median diameter) is the drop size for which the masses in drops larger and smaller than this diameter are equal. In an average sense, smaller droplets (desirable from the combustion standpoint) are produced with larger impingement angles, higher jet velocities, and smaller orifice diameters. As the impingement angle and liquid jet velocity are increased, the horizontal momentum of the liquid jet is increased resulting in the increase of the horizontal impact force between two liquid jets. Therefore, the liquid is more widely dispersed centering around the impingement point. Consequently, the thickness of the liquid sheet and liquid ligaments decreases, resulting in smaller droplets. An increase of the orifice diameter from  $D_j = 1.016 \text{ mm}$  to  $D_j = 1.534 \text{ mm}$  produced a spray characterized by large liquid ligaments in the far downstream region of the spray. Relatively large size droplets are produced by the break-up of these ligaments or by direct detachment of liquid from the boundary of ligaments.

Figure 5 shows the effect of liquid properties on the droplet diameter for  $D_j = 1.016 \text{ mm}$ ,  $2\theta = 90^\circ$ . The mean diameters of water and three glycerol solutions fall almost in a straight line regardless of the fact that these data represent the variation of liquid viscosity up to 20 times the viscosity of water. This finding is interesting because the spray pattern of the glycerol solutions was visibly different from that of water at the same liquid jet velocity. On the other hand, the mean diameters of the ethanol spray always fall in the lower region of the above-mentioned straight line even though there was not big difference in the overall spray patterns of ethanol and water. Based on the above findings, it can be concluded that the surface tension of the liquid plays an important role on the droplet size of the spray without noticeable change in the overall spray pattern, whereas viscosity affects the overall spray pattern without marked effects on the droplet size of the spray.

The present results for the droplet diameters were compared with existing available results in Fig. 6. It is worth noting that the orifice diameter used in the comparison for the present study

is 1.016 and those for Heidmann and Foster [6], Dombrowski and Hooper [7], and Anderson et al. [9] are 2.26, 0.5, and 0.64 respectively. Only the comparisons with the most recent of these studies are shown in Fig. 6, for brevity. Generally, the results with the larger orifice diameter featured larger droplet sizes (Fig. 6). A decrease of the droplet diameters with an increase of the impingement angle and liquid jet velocity was observed in all the results of other researchers [6,7,9], which is in agreement with the trends of the present study.

### 3.3 Droplet Size Distribution

Numerous attempts have been made to obtain suitable mathematical or empirical expressions for the drop size distribution in sprays. Those in general use include the normal, log-normal, Nukiyama-Tanasawa, Rosin-Rammler, and upper-limit distributions [15]. In the present study, the Rosin-Rammler distribution, which is one of the most widely used expressions presently, and the universal root-normal distribution proposed by Simmons [17] were compared with experimental data.

The universal root-normal and Rosin-Rammler distributions are compared with the experimental results in Figs. 7 and 8. In most of the cases, the superiority of the universal root-normal distribution to the Rosin-Rammler distribution is obvious. The effect of jet velocity on the cumulative volume distribution is shown in Fig. 7. The maximum diameter and the slope of the curve changes noticeably when the jet velocity changes from  $V_j = 12.0 \text{ m/s}$  to  $V_j = 15.4 \text{ m/s}$ . No substantial variation is observed once the liquid jet velocity is over  $15.0 \text{ m/s}$ . The slope of the curve becomes steeper as the jet velocity is increased. This implies that the droplet diameters which have the same percentage of total liquid volume become smaller. For example, the  $D_{MMD}$  (50% of total liquid volume is within this diameter) obtained from the experimental data is 523.41, 375.31, and 295.35  $\mu\text{m}$  for  $V_j = 12.0, 15.4$ , and  $19.1 \text{ m/s}$ , respectively. The cumulative volume distributions for different liquids shown in Fig. 8 feature slopes that are a bit steeper than that of water at similar operating conditions.

### 3.4 Droplet Velocity Measurement

The effects of the impingement angle, liquid jet velocity, and orifice diameter on the droplet velocities were also investigated. Only the results of the liquid jet velocity are shown in Fig. 9 due to space limitations. Additional information can be found in [16]. The symbol,  $V_m$ , stands for the magnitude of the velocity vector throughout this study. In an average sense, faster droplets are generated with larger impingement angle, higher jet velocity, and smaller orifice diameter. The droplet velocities are almost linearly proportional to the liquid jet velocity as shown in Fig. 9. The magnitude of the droplet velocities is similar to that of the liquid jet velocity, which implies that the velocities of other liquid elements (liquid sheet or liquid ligaments) are also close to the liquid jet velocity. The horizontal velocities did not change markedly by varying the primary parameters, whereas the vertical velocities show the same trend as the mean droplet velocities.

Figure 10 shows the effect of liquid properties on the droplet velocities for  $D_j = 1.016 \text{ mm}$  and  $2\theta = 90^\circ$ . The linear proportionality of the droplet velocities to the liquid jet velocity (already shown in Fig. 9) is still apparent in spite of the large variation in the physical properties of the liquid (surface tension and viscosity). According to this observation, we can conclude that, in the parametric domain studied, the physical properties of the liquid do not markedly affect the droplet velocities of the resulting spray, whereas they have an effect on the droplet diameters, as discussed earlier.

Limited experimental data are available for the comparison of measurements of droplet velocities. Figure 11 shows the comparison of the results of the present velocity measurements with those of Anderson et al. [9]. It is worth noting that the orifice diameter they used is smaller ( $D_j = 0.64 \text{ mm}$ ) than that of the present study ( $D_j = 1.016 \text{ mm}$ ) and the position they probed was  $y = 41 \text{ mm}$  at the spray axis, while the present results in Fig 11 were taken from the region  $y = 50$  to  $70 \text{ mm}$  at the spray axis ( $x=0$ ). The velocities in [9] are generally smaller than those of the present study. The trends agree rather well.

## 4. Conclusions

In this paper an experimental study of the fluid dynamics of a spray created by two impinging jets was presented. The experiments with two non-evaporating impinging jets injected into still air at atmospheric pressure were conducted utilizing a novel two-reference-beam double-pulse holographic technique. This holographic method features the capability of separation of the first and second droplet images by using two reference beams and polarization of the laser light. The effect of the impingement angle, liquid jet velocity, orifice diameter, and liquid properties on the atomization process was investigated using water, ethanol, and three glycerol solutions. Visualization of the structure of the generated spray as well as measurements on the size and velocity of the liquid droplets were performed.

The results confirmed the inherent wave nature in the disintegration process characteristic of this kind of atomization. This feature was more distinct with high-viscosity liquids. The overall spray pattern was mainly affected by the impingement angle, orifice diameter, and viscosity of liquid, whereas the liquid jet velocity and the surface tension of the liquid had no significant effect.

Smaller and faster droplets were generated with larger impingement angle, higher jet velocity, and smaller orifice diameter. The relative error in the droplet diameter measurements was 5% and in the velocity measurements 20%. The surface tension of the liquid plays an important role in the droplet size of the spray without any noticeable change in the overall spray pattern. Viscosity affects the structure of the spray without significant effects on the droplet size. It was also found that the liquid properties did not markedly affect the droplet velocities. The superiority of the universal root-normal droplet size distribution to the Rosin-Rammler distribution was proved in the great majority of tested cases.

### **Acknowledgment**

The support of the Air Force Office of Scientific Research under grant number AFOSR F49620-92-J-0343 is gratefully acknowledged. We thank Prof. G.M. Faeth of the University of Michigan for his recommendation that we compare our droplet size measurements to the Simmons correlation.

## References

1. Sutton, G. P., *Rocket propulsion element: An introduction to the engineering of rockets*, John Wiley & Sons, 1992.
2. Harrje, D. T., and Reardon, F. H., *Liquid Propellant Rocket Combustion Instability*, NASA SP-194, 1972.
3. Heidmann, M. F., and Humphrey, J. C., "Fluctuations in a Spray Formed by Two Impinging Jets," NACA TN 2349, 1951.
4. Heidmann, M. F., Priem, R. J., and Humphrey, J. C., "A Study of Sprays Formed by Two Impinging Jets," NACA TN 3835, 1957.
5. Foster, H. H., and Heidmann, M. F., "A Spatial Characteristics of Water Spray Formed by Two Impinging Jets at Several Jet Velocities in Quiescent Air," NASA TN D-301, 1960.
6. Heidmann, M. F., and Foster, H. H., "Effect of Impingement Angle on Drop Size Distribution and Spray Pattern of Two Impinging Water Jets," NASA TN D-872, 1961.
7. Dombrowski, N., and Hooper, P. C., "A Study of the Sprays Formed by Impinging Jets in Laminar and Turbulent Flow," *Journal of Fluid Mechanics*, Vol. 18, 1963, p. 392.
8. Huang, J. C. P., "The Break-up of Axisymmetric Liquid Sheets," *Journal of Fluid Mechanics*, Vol. 43, 1970, p. 305.
9. Anderson, W. E., Ryan, H. M., Pal, S., and Santoro, R. J., "Fundamental Studies of Impinging Liquid Jets," AIAA Paper 92-0458, 1992.
10. Dombrowski, N. and Johns, W. R., "The Aerodynamic Instability and Disintegration of Viscous Liquid Sheets," *Chemical Engineering Science*, Vol. 18, 1963, p. 203.
11. Ryan, H. M., Anderson, W. E., Pal, S., and Santoro, R. J., "Atomization Characteristics of Impinging Liquid Jets," accepted for publication in *Journal of Propulsion and Power*.
12. Ibrahim, E. A. and Przekwas, A. J., "Impinging Jets Atomization," *Physics of Fluids A*, Vol. 3, 1991, p. 2981.
13. Vassallo, P., and Ashgriz, N., "Effect of Flow Rate on the Spray Characteristics of Impinging Water Jets," *Journal of Propulsion and Power*, Vol. 8, 1992, p. 980.

14. B. Kang, D. Poulikakos and Y. Shen. "Holography Experiments on Impinging Liquid Jet Atomization: Testing of Theoretical Predictions," accepted for publication in *Atomization and Sprays*, to appear in 1995.
15. Lefebvre, A. H., *Atomization and Sprays*, Hemisphere Publishing Co., 1989.
16. Kang, B., "A Holographic Study of the Dense Region of a Spray Created by Two Impinging Jets," *PH.D. Thesis*, University of Illinois at Chicago, 1995.
17. Simmons, H. C., "The Correlation of Drop-Size Distributions in Fuel Nozzle Sprays," *Journal of Engineering for Power*, Vol. 99, No. 3, 1977, p. 309.

Table 1 Summary of test conditions

Case	Liquid	Orifice Diameter, $D_j$ (mm)	Impingement Angle, $2\theta$ (°)	Liquid Jet Velocity, $V_j$ (m/s)	$Re_j$	$We_j$
H1-1	water	1.016	90	12.0	8590	1000
H1-2	water	1.016	90	12.0	8590	1000
H1-3	water	1.016	90	12.0	8590	1000
H2	water	1.016	60	12.0	6070	500
H3	water	1.016	120	12.0	10520	1500
H4	water	1.016	90	15.4	11020	1650
H5	water	1.016	90	19.1	13670	2540
H6	water	1.534	90	11.9	12860	1490
E1	ethanol	1.016	90	7.2	3410	920
E2	ethanol	1.016	90	9.1	4300	1460
E3	ethanol	1.016	90	11.9	5640	2520
G1	50% glycerol	1.016	90	8.0	1070	530
G2	59% glycerol	1.016	90	12.3	990	1290
G3	68% glycerol	1.016	90	11.7	510	1210

Table 2 Physical properties of the liquids used in the experiment at 20°C and 1 atm.

Liquid	Density ( $kg/m^3$ )	Viscosity $\times 10^3$ ( $N s/m^2$ )	Surface tension $\times 10^3$ ( $N/m$ )
water	998 (1.0)	1.002 (1.0)	72.88 (1.0)
ethanol	791 (0.79)	1.200 (1.20)	22.80 (0.31)
50% glycerol	1124.9 (1.13)	6.05 (6.04)	69.68 (0.96)
59% glycerol	1149.5 (1.15)	10.25 (10.23)	68.70 (0.94)
68% glycerol	1174.2 (1.18)	19.40 (19.36)	67.72 (0.93)

## List of Figures

- Figure 1 Schematic diagram of a spray formed by two high speed impinging jets. The insert in this figure shows a side view of the impingement region.
- Figure 2 Schematic of the optical setup for double-pulse holography with two reference beams.
- Figure 3 Photographs of hologram revealing droplet images at the first and the second pulse with  $D_j = 1.016$  mm,  $2\theta = 60^\circ$ ,  $V_j = 12.0$  m/s,  $(x, y) = (0.0$  cm, 4.0 cm) (a) droplet images at the first pulse (b) droplet images at the second pulse.
- Figure 4 Effect of the impingement angle, liquid jet velocity, and orifice diameter on mean diameters (a)  $D_j = 1.016$  mm,  $V_j = 12.0$  m/s (b)  $D_j = 1.016$  mm,  $2\theta = 90^\circ$  (c)  $V_j = 12.0$  m/s,  $2\theta = 90^\circ$ . The maximum relative error in the measurements was 5%.
- Figure 5 Effect of liquid properties on mean diameters for  $D_j = 1.016$  mm,  $2\theta = 90^\circ$ . The maximum relative error in the measurements was 5%.
- Figure 6 Comparison of the size measurement results ( $D_j = 1.016$  mm) with  $D_{10}$  results from Anderson et al. [9] for  $D_j = 0.64$  mm.
- Figure 7 Comparison of cumulative volume distributions with the Simmons and Rossin-Rammler distributions for water,  $D_j = 1.016$  mm,  $2\theta = 90^\circ$  (a)  $V_j = 12.0$  m/s (b)  $V_j = 15.4$  m/s (c)  $V_j = 19.1$  m/s.
- Figure 8 Comparison of cumulative volume distributions with the Simmons and Rossin-Rammler distributions for  $D_j = 1.016$  mm,  $2\theta = 90^\circ$  (a) Ethanol,  $V_j = 11.9$  m/s (b) Glycerol (59 %),  $V_j = 12.3$  m/s (c) Glycerol (68 %),  $V_j = 11.7$  m/s.
- Figure 9 Effect of the liquid jet velocity on mean velocities  $D_j = 1.016$  mm,  $2\theta = 90^\circ$ . The maximum relative error in the measurements was 20%.
- Figure 10 Effect of liquid properties on mean velocities for  $D_j = 1.016$  mm,  $2\theta = 90^\circ$ . The maximum relative error in the measurements was 20%.
- Figure 11 Comparison of velocity measurement results with those of Anderson et al. [9] ( $D_j = 1.016$  and 0.64 mm for the present study and Anderson et al. [9], respectively).

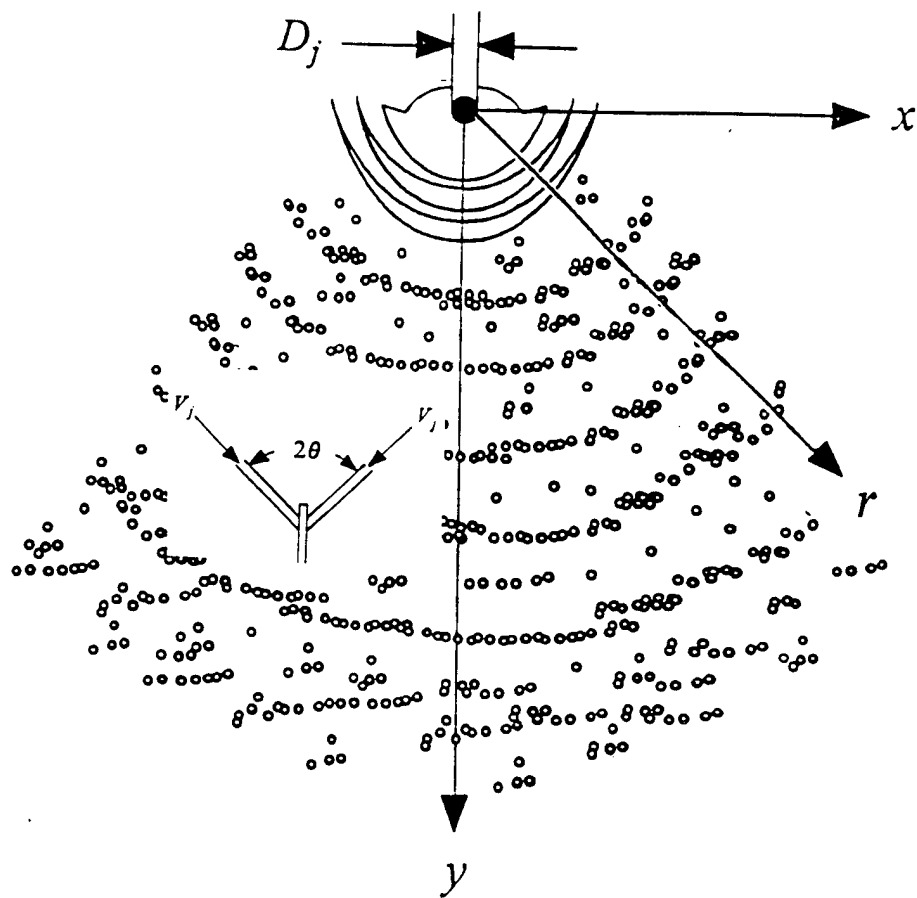


Figure 1

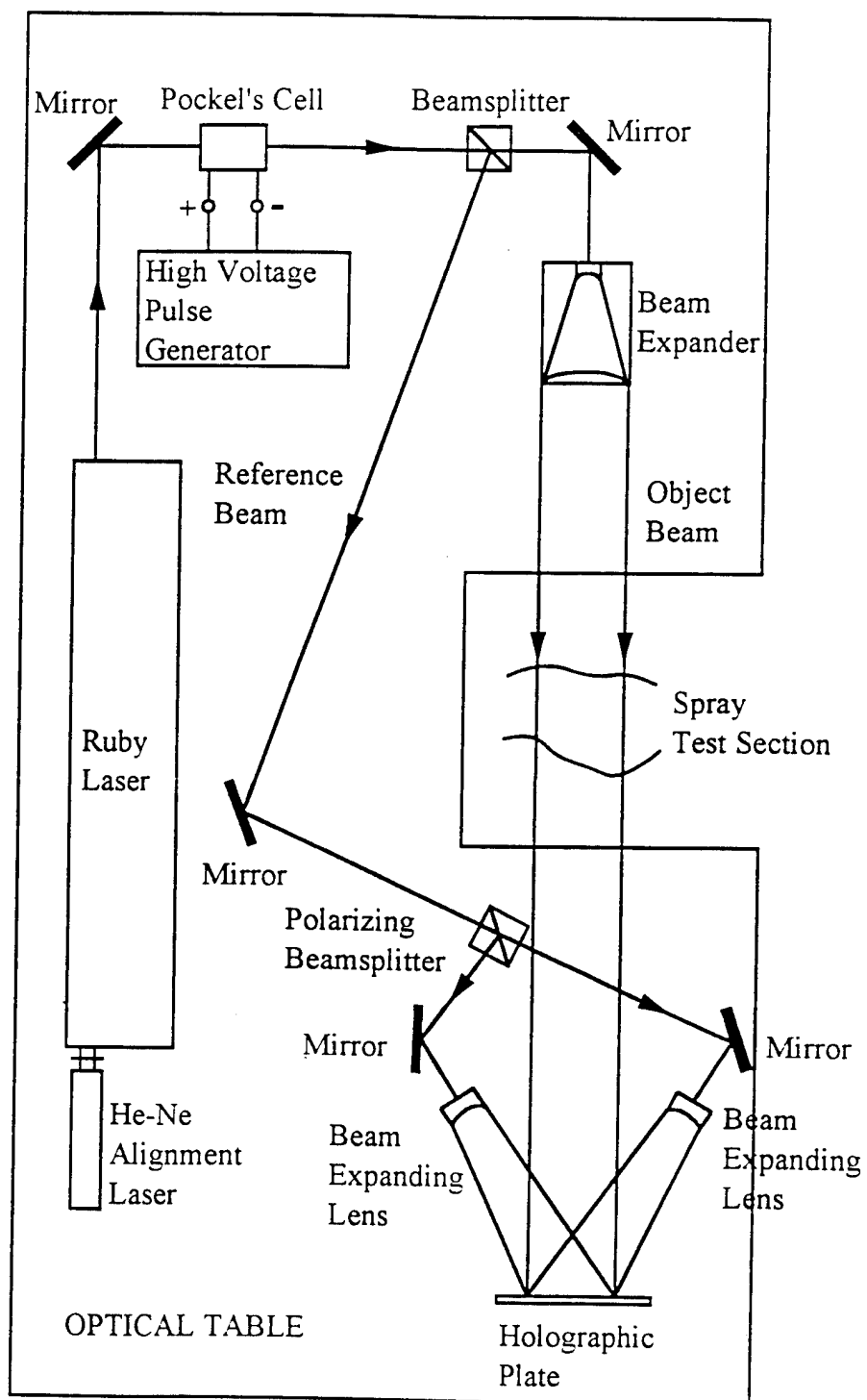


Figure 2



(a)

5 mm



(b)

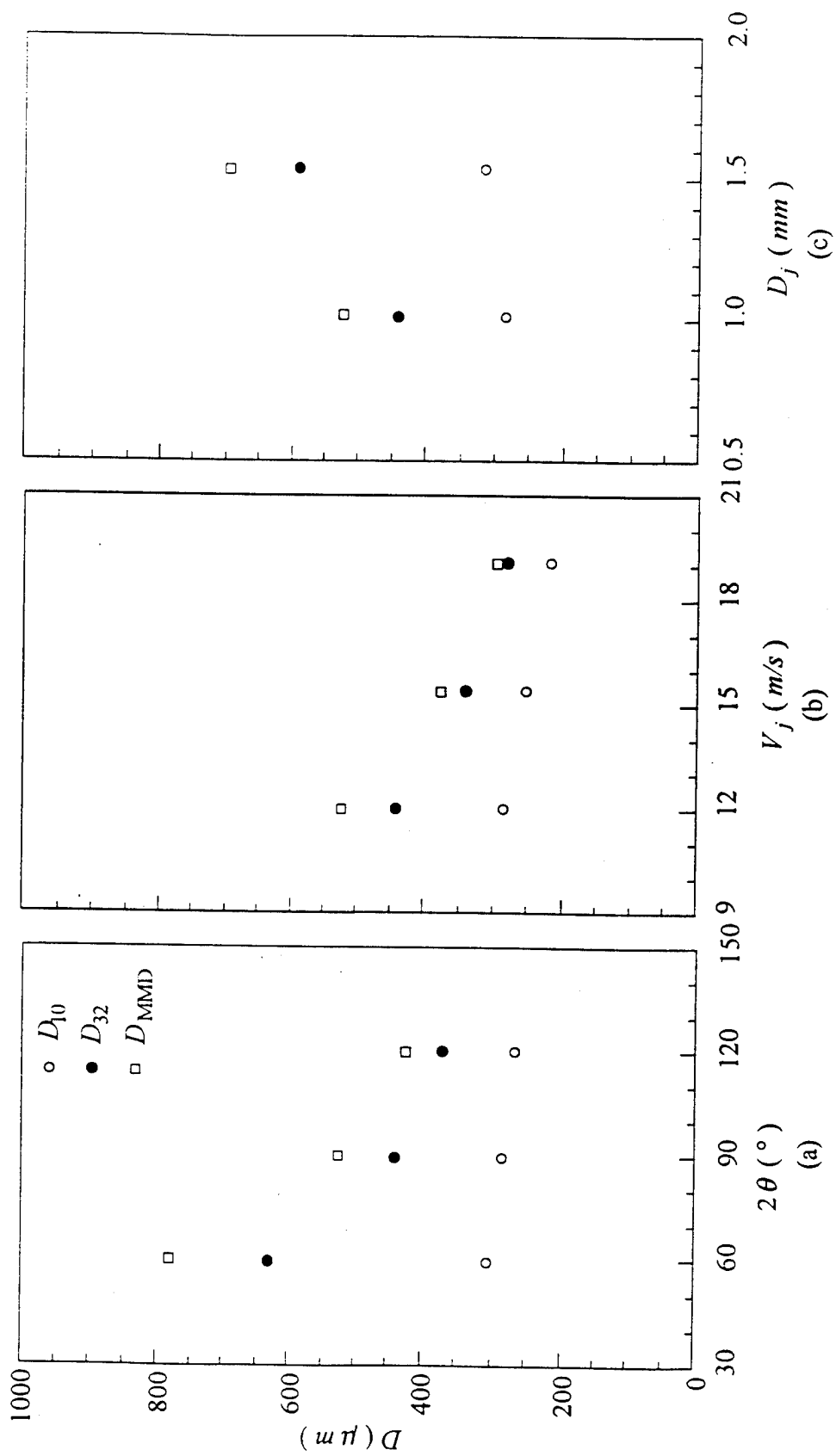


Fig. 4

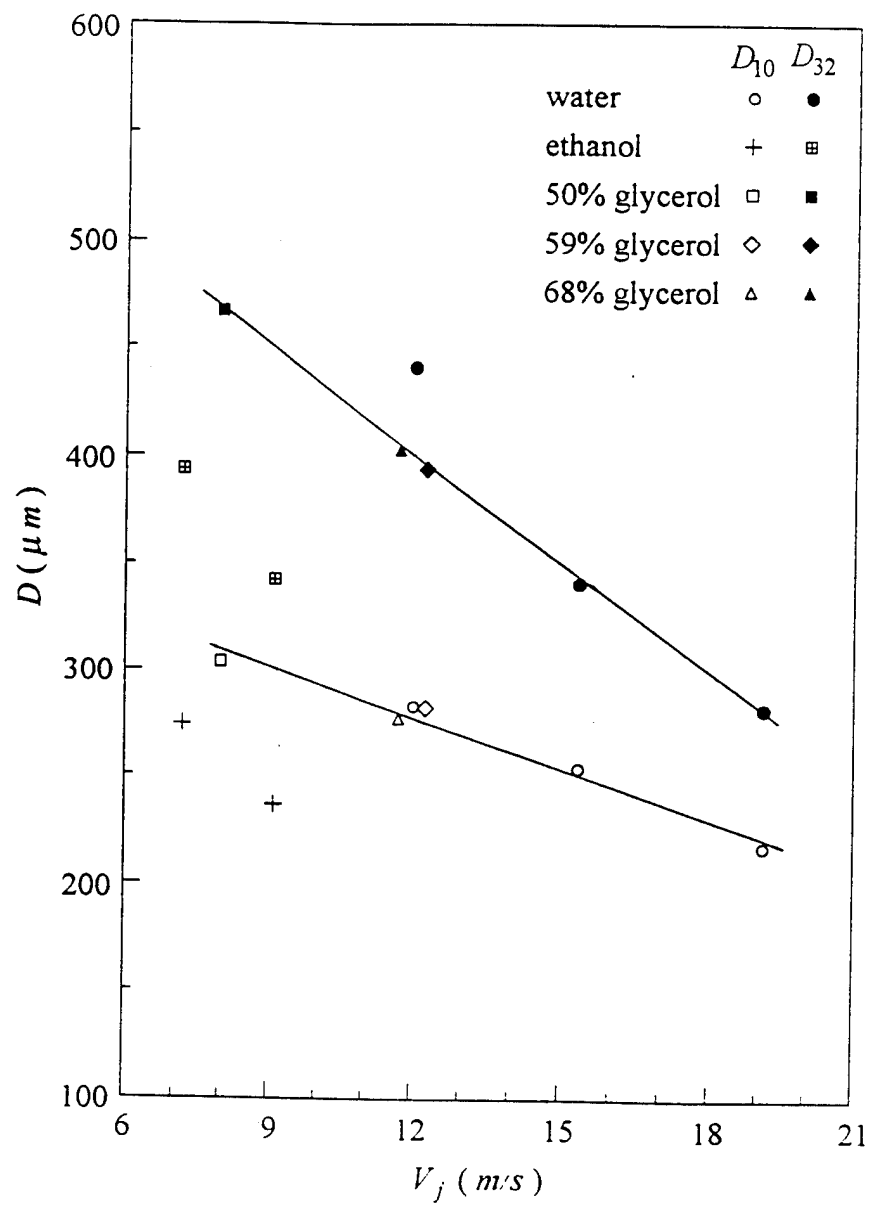


Fig. 5

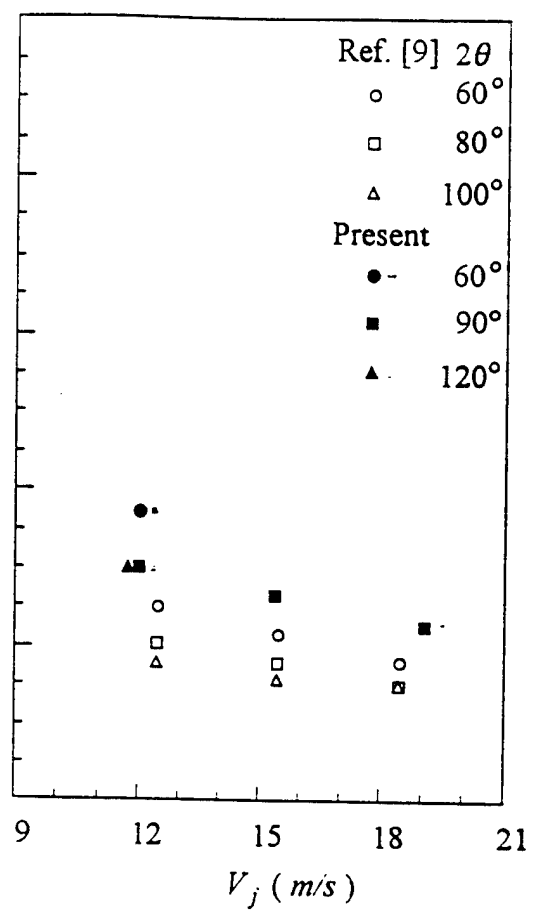
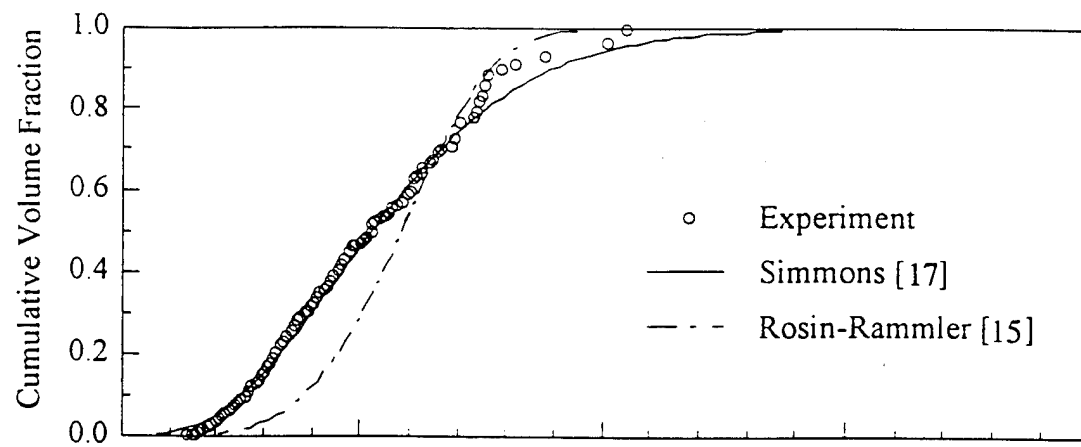
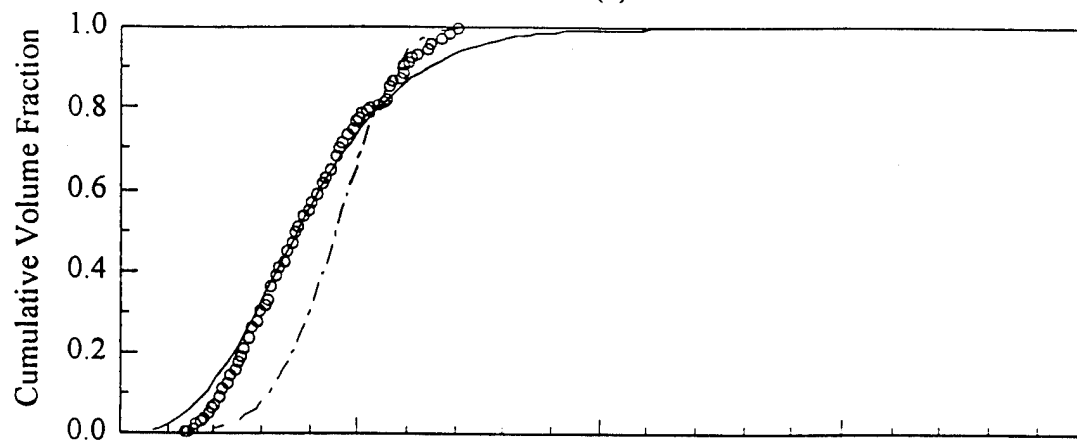


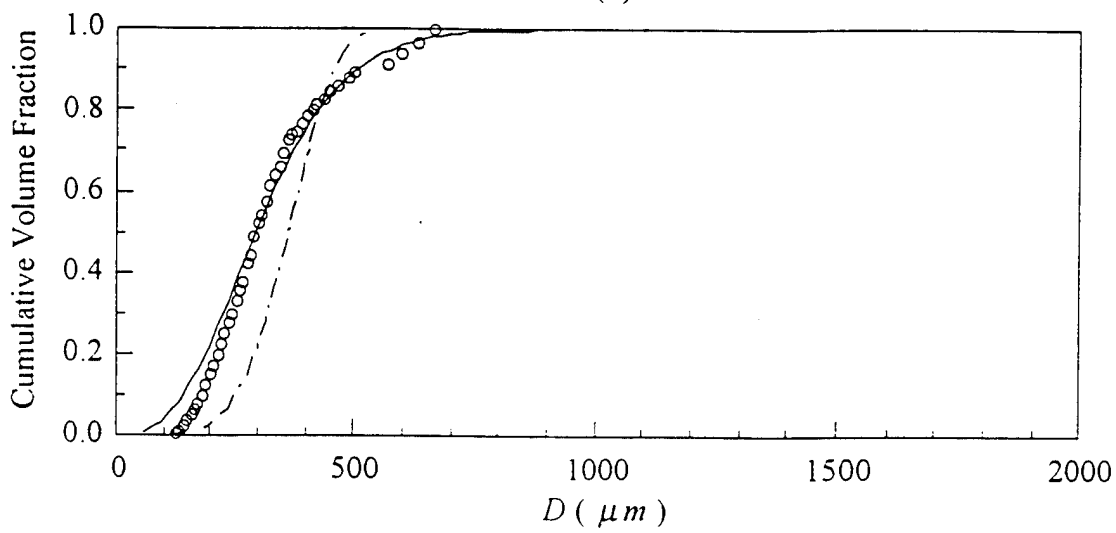
Figure 6



(a)

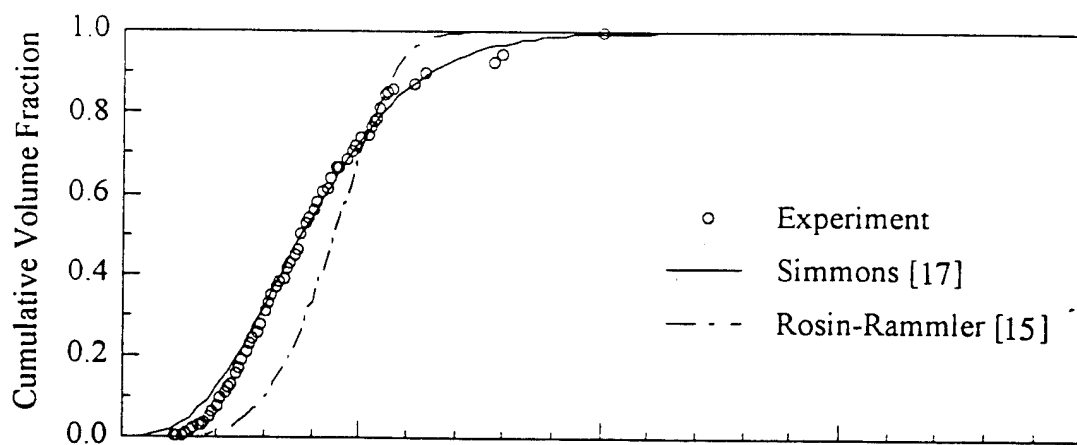


(b)

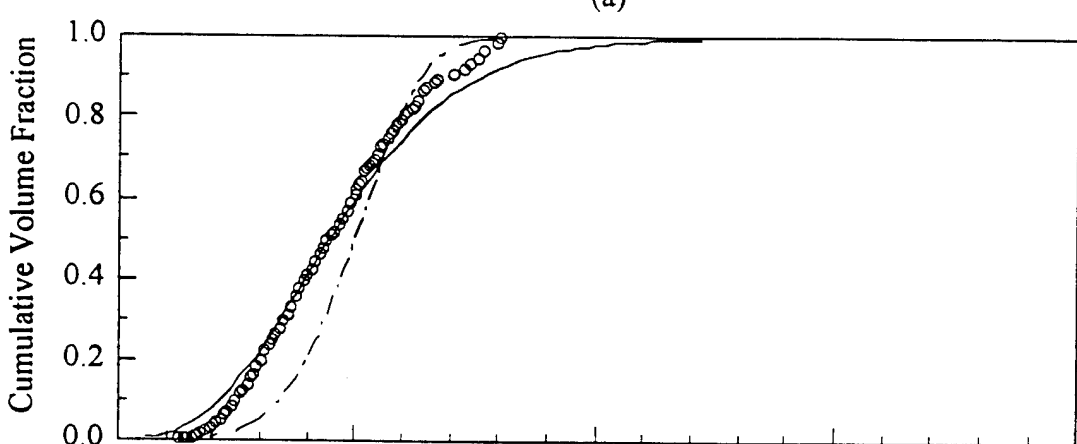


(c)

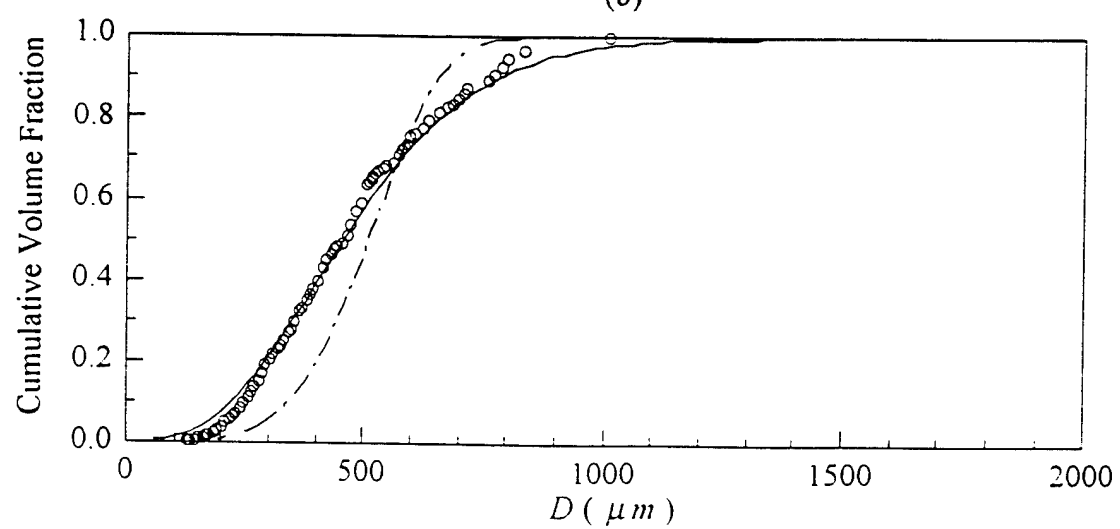
Fig. 7



(a)



(b)



(c)

Fig. 8

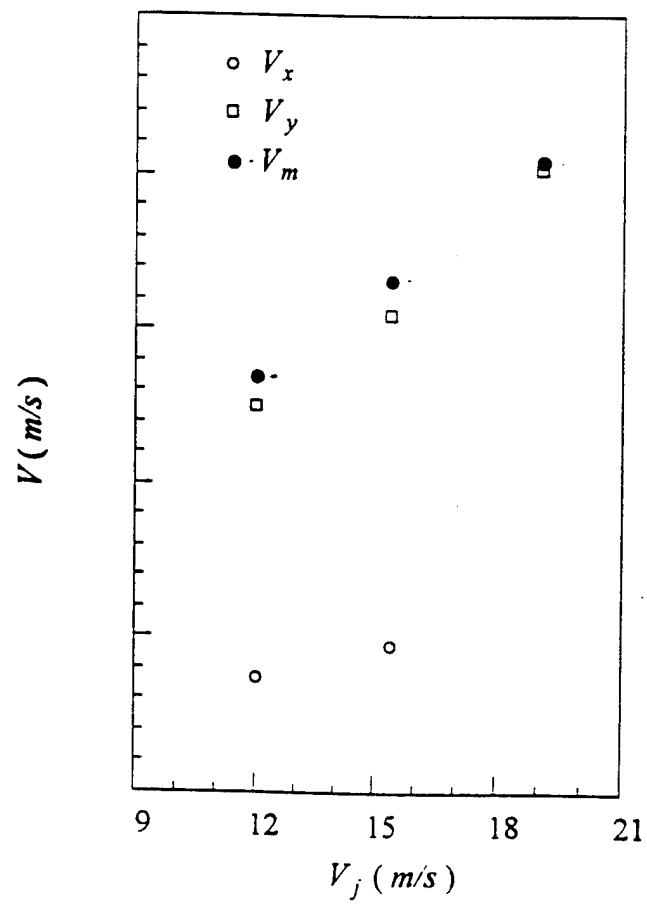


Figure 9

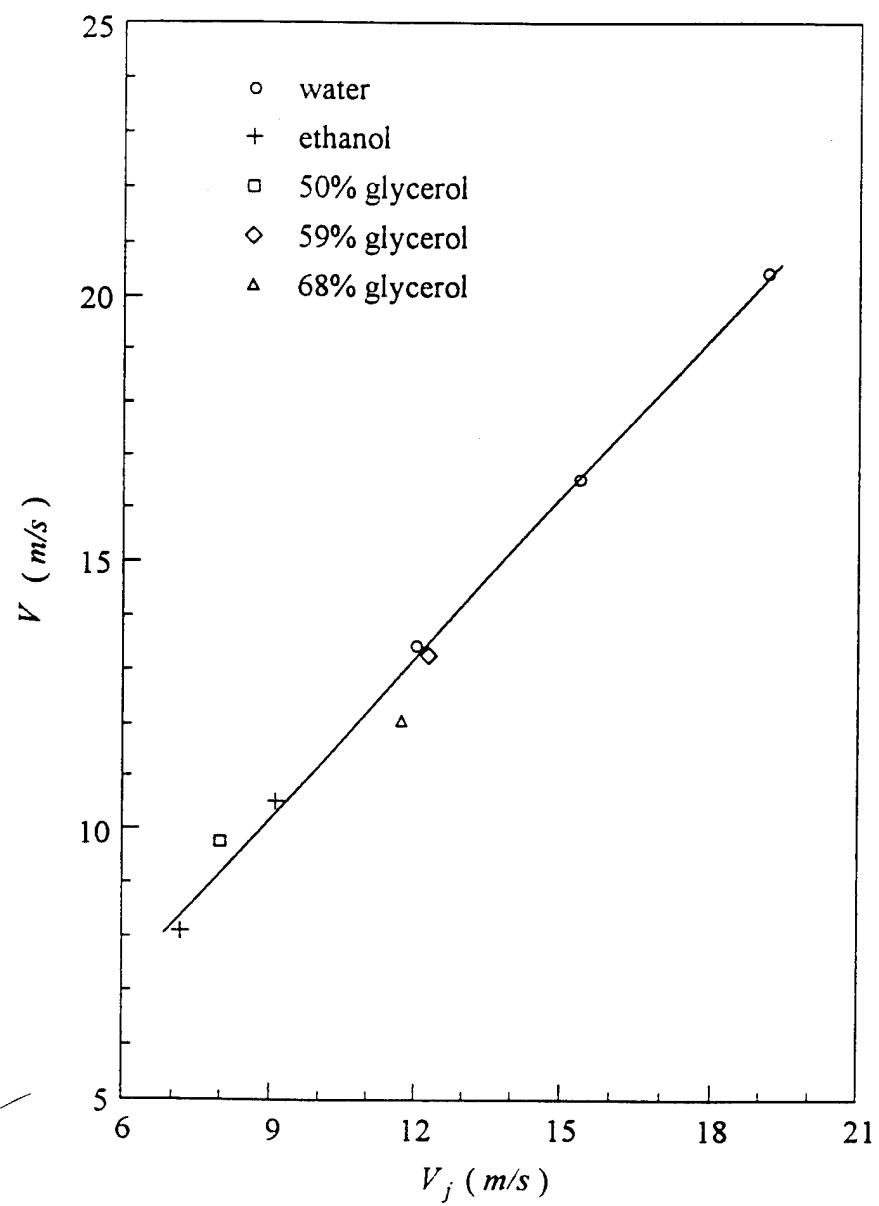


Figure 10

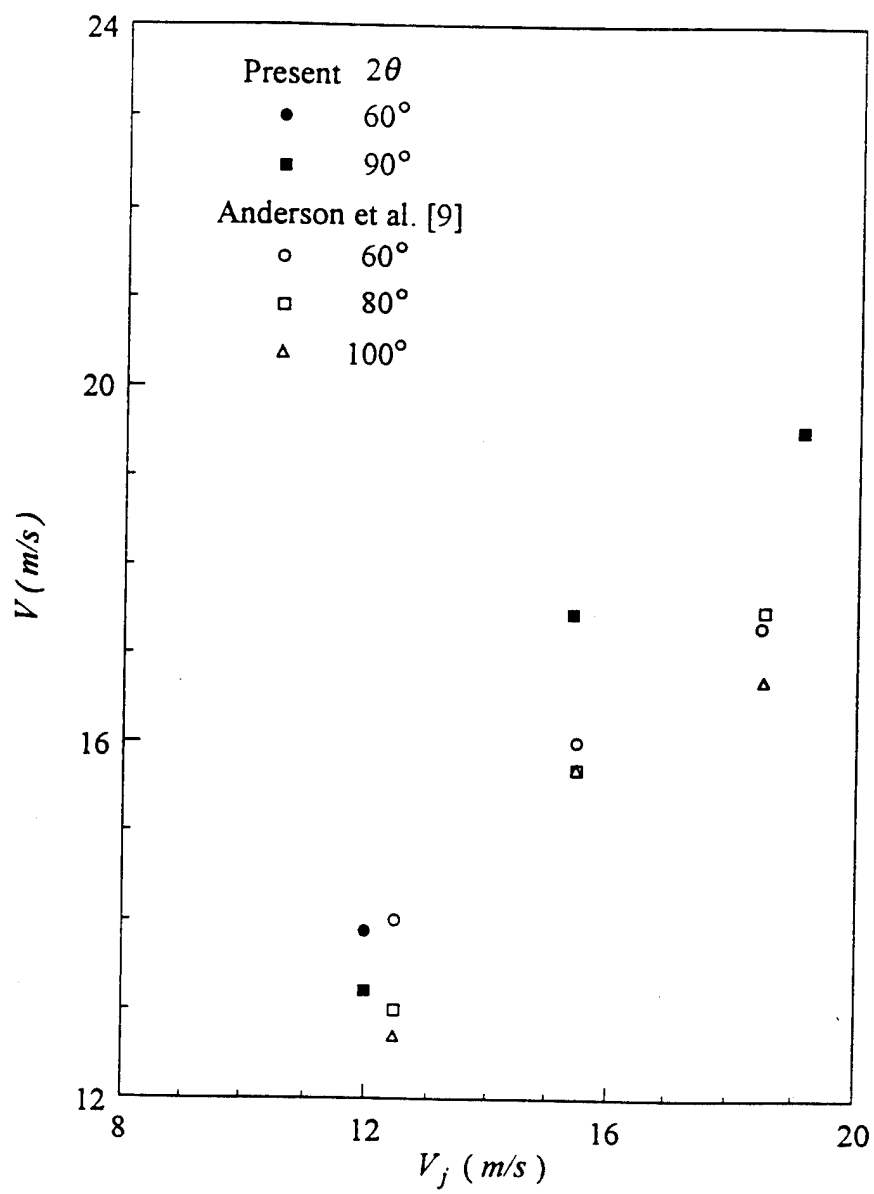


Fig. 11